Università degli Studi di Napoli

"Federico II"

Ph.D. Thesis
in
Information Technology and Electrical Engineering

Innovative Techniques to Devise 3D-printed Anatomical Brain Phantoms for Morpho-functional Medical Imaging

Maria Agnese Pirozzi

Tutor: Prof. Mario Cesarelli

Co-tutors: Dr. Mario Quarantelli, MD

Ing. Mario Magliulo, PhD

Coordinator: Prof. Daniele Riccio

XXXIII Ciclo

Scuola Politecnica e delle Scienze di Base
Dipartimento di Ingegneria Elettrica e Tecnologie dell'Informazione (DIETI)

Contents

List of Acronyms

3DP	–	3D Printing
ABS	–	Acrylonitrile Butadiene Styrene
AM	–	Additive Manufacturing
AMF	–	Additive Manufacturing File Format
ASCII	–	American Standard Code for Information Interchange
B-Rep	–	Boundary Representation
BET	–	Brain Extraction Tool
BSE	–	Brain Surface Extractor
CAD	–	Computer-Aided Design
CAM	–	Computer-Aided Manufacturing
CBF	–	Cerebral Blood Flow
CNC	–	Computer Numerical Control
CNS	–	Central Nervous System
CSE	–	Conventional Spin-echo
CSF	–	Cerebrospinal Fluid
CSG	–	Constructive Solid Geometry
CT	–	Computed Tomography
DLF	–	Digital Light Fabrication
DLP	–	Digital Light Processing
DMD	–	Direct Metal Deposition
DMLS	–	Direct Laser Sintering to Metal
EBM	–	Electron Beam Melting
ECT	–	Emission Computed Topography
FDG	–	Fluorodeoxyglucose
FDM	–	Fused Deposition Modelling
FFF	–	Fused Filament Fabrication

FLAIR	–	Fluid Attenuated by Inversion Recovery
GM	–	Grey Matter
HIPS	–	High Impact Polystyrene
ICV	–	Intracranial Voxels
IGES	–	Initial Graphics Exchange Specification
LENS	–	Laser Engineered Net Shaping
LOM	–	Laminated Object Manufacturing
MNI	–	Montreal Neurological Institute
MRI	–	Magnetic Resonance Imaging
NEC	–	Noise Equivalent Count
NURBS	–	Non-Uniform Rational B-Spline
PC	–	Polycarbonate
PD	–	Proton Density
PDw	–	PD-weighted
PET	–	Positron Emission Tomography
PET-G	–	Polyethylene Terephthalate Glycol-modified
PLA	–	Polylactic Acid
PVA	–	Polyvinyl Alcohol
QMCI	–	Quantitative Magnetic Color Imaging
R1	–	Longitudinal Relaxation Rate (1/T1)
R2	–	Transverse Relaxation Rate (1/T2)
ROI	–	Region of Interest
SPECT	–	Single Photon Emission Tomography
SHS	–	Selective Heat Sintering
SLA	–	Stereolithography
SLM	–	Selective Laser Melting
SLS	–	Selective Laser Sintering
SPM	–	Statistical Parametric Mapping
STL	–	Standard Tessellation/Triangulation Language
T1	–	Longitudinal or Lattice-spin Relaxation Time

T1w	–	T1-weighted
T2	–	Transverse or Spin-spin Relaxation Time
T2w	–	T2-weighted
TPM	–	Tissue Probability Maps
TPU	–	Thermoplastic Polyurethane
UAM	–	Ultrasonic Additive Manufacturing
WM	–	White Matter

List of Figures

Figure 6 – Brain lobes and major brain structures. The lobes are the 4 major subdivisions into which the cerebral cortex is divided in each hemisphere. The frontal lobe is located at the front of each hemisphere, opposite the parietal and temporal lobes, and is the largest of the four lobes. The parietal lobe is positioned over the occipital and temporal lobes, beyond the frontal lobe and the central sulcus. The occipital lobe constitutes the posterior end of the telencephalic hemispheres and has no limits whatsoever with the temporal lobe, which is in turn located below the frontal and parietal lobes from which it is separated by the lateral (Sylvian) fissure. The figure also shows the main structures of the

List of Tables

Abstract

Introduction. The Ph.D. thesis addresses the development of innovative techniques to create 3D-printed anatomical brain phantoms, which can be used for quantitative technical assessments on morpho-functional imaging devices, providing simulation accuracy not obtainable with currently available phantoms.

3D printing (3DP) technology is paving the way for advanced anatomical modelling in biomedical applications. Despite the potential already expressed by 3DP in this field, it is still little used for the realization of anthropomorphic phantoms of human organs with complex internal structures. Making an anthropomorphic phantom is very different from making a simple anatomical model and 3DP is still far from being *plug-and-print*. Hence, the need to develop *ad-hoc* techniques providing innovative solutions for the realization of anatomical phantoms with unique characteristics, and greater *ease-of-use*.

Aim. The thesis explores the entire workflow (brain MRI images segmentation, 3D modelling and materialization) developed to prototype a new complex anthropomorphic brain phantom, which can simulate three brain compartments simultaneously: grey matter (GM), white matter (WM) and striatum (caudate nucleus and putamen, known to show a high uptake in nuclear medicine studies). The three separate chambers of the phantom will be filled with tissue-appropriate solutions characterized by different concentrations of radioisotope for PET/SPECT, para-/ferro-magnetic metals for MRI, and iodine for CT imaging.

Methods. First, to design a 3D model of the brain phantom, it is necessary to segment MRI images and to extract an error-less STL (Standard Tessellation Language) description. Then, it is possible to materialize the prototype and test its functionality.

- ***Image segmentation.*** Segmentation is one of the most critical steps in modelling. To this end, after demonstrating the *proof-of-concept*, a multi-parametric segmentation approach based on brain relaxometry was proposed. It includes a pre-processing step to estimate relaxation parameter maps (R1 = longitudinal relaxation rate, R2 = transverse relaxation rate, PD = proton density) from the signal intensities provided by MRI sequences of routine clinical protocols (3D-GrE T1-weighted, FLAIR and fast-T2-weighted sequences with ≤ 3 mm slice thickness). In the past, maps of R1, R2, and PD were obtained from Conventional Spin Echo (CSE) sequences, which are no longer suitable for clinical practice due to long acquisition times. Rehabilitating the multi-parametric segmentation based on relaxometry, the estimation of pseudo-relaxation maps allowed developing an innovative method for the simultaneous automatic segmentation of most of the brain structures (GM, WM, cerebrospinal fluid, thalamus, caudate nucleus, putamen, pallidus, nigra, red nucleus and dentate). This method allows the segmentation of higher resolution brain images for future brain phantom enhancements.

- ***STL extraction.*** After segmentation, the 3D model of phantom is described in STL format, which represents the shapes through the approximation in *manifold* mesh (i.e., collection of triangles, which is continuous, without holes and with a positive – not

zero – volume). For this purpose, we developed an automatic procedure to extract a single voxelized surface, tracing the anatomical interface between the phantom's compartments directly on the segmented images. Two tubes were designed for each compartment (one for filling and the other to facilitate the escape of air). The procedure automatically checks the continuity of the surface, ensuring that the 3D model could be exported in STL format, without errors, using a common image-to-STL conversion software. Threaded junctions were added to the phantom (for the hermetic closure) using a mesh processing software. The phantom's 3D model resulted correct and ready for 3DP.

Prototyping. Finally, the most suitable 3DP technology is identified for the materialization. We investigated the material extrusion technology, named Fused Deposition Modeling (FDM), and the material jetting technology, named PolyJet. FDM resulted the best candidate for our purposes. It allowed materializing the phantom's hollow compartments in a single print, without having to print them in several parts to be reassembled later. FDM soluble internal support structures were completely removable after the materialization, unlike PolyJet supports. A critical aspect, which required a considerable effort to optimize the printing parameters, was the submillimetre thickness of the phantom walls, necessary to avoid distorting the imaging simulation. However, 3D printer manufacturers recommend maintaining a uniform wall thickness of at least 1 mm. The optimization of printing path made it possible to obtain strong, but not completely waterproof walls, approximately 0.5 mm thick. A sophisticated technique, based on the use of a polyvinyl-acetate solution, was developed to waterproof the internal and external phantom walls (necessary requirement for filling). A filling system was also designed to minimize the residual air bubbles, which could result in unwanted hypo-intensity (dark) areas in phantom-based imaging simulation.

Discussions and conclusions. The phantom prototype was scanned trough CT and PET/CT to evaluate the realism of the brain simulation. None of the state-of-the-art brain phantoms allow such anatomical rendering of three brain compartments. Some represent only GM and WM, others only the striatum. Moreover, they typically have a poor anatomical yield, showing a reduced depth of the sulci and a not very faithful reproduction of the cerebral convolutions. The ability to simulate the three brain compartments simultaneously with greater accuracy, as well as the possibility of carrying out multimodality studies (PET/CT, PET/MRI), which represent the frontier of diagnostic imaging, give this device cutting-edge prospective characteristics. The effort to further customize 3DP technology for these applications is expected to increase significantly in the coming years.

Chapter 1

3D Printing in Biomedical Applications

1.1. Introduction

Additive Manufacturing (AM), also known as 3D Printing (3DP), rapid prototyping, layered manufacturing or solid "free-form fabrication", is a disruptive technology that is changing the manufacturing industry in many fields. AM is a production method that allows the creation of objects (components, semi-finished or finished products), using different techniques, which are mainly based on the deposition of successive layers of material. Differently from traditional production techniques (subtractive manufacturing), in which objects are obtained by subtraction from solid (through process as milling, drilling, or turning), in AM the product is created by depositing only the material necessary for the realization, thus reducing waste. 3DP is the most popular AM process and it is marking an important evolution of the AM, entering the broad trend towards the digitalization of manufacturing [1]. In the biomedical field, the 3DP is paving the way for many new applications ranging from surgical planning, to medical education and training, customised prosthesis design, medical imaging research, bioprinting and many others [2]. In this chapter, the state of the art of 3DP for biomedical applications will be described, while providing the information necessary for the development of the methods and techniques, object of this doctoral thesis work.

1.2. History of 3D Printing

AM techniques were conceived for rapid prototyping. However, the great development of 3DP technology, in the last thirty years of history, has highlighted its huge potential for different applications in various fields (medicine, automotive, jewellery, aerospace and so on) by expanding the usability of existing materials and creating new ones.
The first traces of a technology that made rapid mechanical prototyping possible could already be found in topography, with the first rudimentary machines for the *layer-by-layer* production of topographic maps in relief; and in photo-

sculpture, the art of creating sculptures through combinations of photographs (from all sides) of the contours and shapes of the object to be reproduced. Right from these first rudimentary "3D printers" the way was opened for successive evolutions in materials and *layer-by-layer* deposition techniques. In 1982, stereolithography (**Section 1.3.1.1**), the first actual 3DP technique, was invented by the American engineer Chuck Hull, who patented it in 1986 [3]. In the same year, Hull was co-founder of *3D Systems*, the first 3DP company in the world. Thus, Hull laid the foundation for 3DP, paving the way for all future developments. Only two years later, in 1988, the spouses S. Scott e Lisa Crump invented and patented a new 3DP technique, Fused Deposition Modelling (FDM) [4], in which a plastic polymer filament is passed through a heated nozzle (**Section 1.3.1.4**). FDM technology printers were marketed starting since the early 1990s by the company *Stratasys*, whose founders were the Crump spouses. It is currently a leader in the professional 3DP industry with bases in Minnesota and Israel. Since 2005, the year of the expiry of the patent on FDM, this technology has started to spread more and more, not only in industrial contexts, but also in research, up to the home of hobbyists. In the last 15 years, therefore, open-source projects have been born, such as *RepRap* [5] and *MakerBot* [6], which allow anyone to build and assemble a 3D printer with their own hands at very low cost. In the wake of these projects, the wording Fused Filament Fabrication (FFF) was also coined to refer to a technology that is completely like *Stratasys*' FDM, but which is developed through entry-level machines. To date, 3DP can even be seen as an evolution of traditional printing on sheets of paper, which can be called "2D printing". Two completely different procedures, which have a fundamental aspect in common: in both cases the design and modelling work is performed on a computer, while the physical implementation is performed by means of a printer, starting from the information provided by the digital file. This analogy becomes more interesting if translated into a medical scenario, for example on the interpretation of medical images. The radiologist is generally used to looking at two-dimensional images of sections of the body to make diagnoses, using, where possible, also 3D digital reconstructions of the anatomies (3D rendering). 3DP therefore becomes the tool to materialize exact anatomical replicas starting from medical images, providing, as discussed below, a new, valid, and more advanced image evaluation tool.

1.3. 3D Printing Technologies

All 3DP technologies have in common the use of a print head through which they additively materialize an object, *layer-by-layer*. The layering process is the innovative aspect that made AM a great invention and a simple example is often used to explain it, the skyscraper. To build a skyscraper it is in fact necessary to

create a base, the foundations, on which the subsequent "floors" of the skyscraper will be placed. Once the first floor has been built, it will then be possible to create the second, on which the third will be erected and so on. Only when the previous floor is fully formed will it be possible to proceed with the construction of the next. In the current standards classifications (ISO/ASTM52900-15 and ISO standard 17296-2:2015), there are seven specific groups of AM/3DP technologies. The group of 3D bioprinting technologies joins these. Although beyond the scope of this discussion, it is important to include it, not only because it emerges from the same classic 3DP technologies, but also because it is of enormous interest in defining the future perspectives of 3DP for biomedical applications based on anthropomorphic phantoms.

1.3.1. Technologies for Biomedical Applications

The five technologies, described below, are the most popular in clinical settings [7]. Each of them has strengths and weaknesses regarding its uses in clinical and medical 3DP applications. The predominant technologies are stereolithography, fused deposition modelling, material jetting and bitter jetting, typically used to realize anatomical models; and powder bed fusion (or more precisely, selective laser sintering), used to fabricate implants, prostheses, and surgical guides [8].

1.3.1.1. Vat Photopolymerization

This technology uses a vat of liquid photopolymer resin, which is hardened according to the printing path, while a platform (printing bed) moves the object to be made downwards (or upwards in bottom-up printers) when each new layer must be cured using ultraviolet (UV) light. The deposited resin layers are polymerized in sequence by exposing them to a light source that follows the shape of the only cross section of the model to be made on that layer (perpendicular to the z axis of the printer). Light starts a chemical reaction in the resin whereby the monomers and oligomers polymerize and become solid. The curing of each layer is not fully completed by the controlled light source to ensure that the next layer also sticks well on the last. In this technology, lattice support structures are added to erect the parts. These supports must be removed manually after printing. A post-processing phase is therefore necessary to complete the polymerization of the model in a UV chamber and to remove the supports [9]. Among the main printing technologies, stereolithography (SLA) and Digital Light Processing (DLP) fall into this category. In SLA, the light source is a laser which is directed by mirrors at different positions on the surface of the liquid to trace the entire area of each layer of the printed object. DLP instead uses a light projector, which instantly illuminates the entire shape of the

printed object layer on the surface of the liquid. Generally, DLP takes less time to print than SLA. These technologies are often used for medical 3DP, especially for bone applications. The main limitations are the difficulty in removing the support structures for very complex and convoluted models, or with small, long or tortuous vessels (such as the coronaries, the cerebral vasculature, the branches of the aorta, etc.); and the impossibility of producing multi-material models, or which require the support material to dissolve in a special solvent (as it is not accessible for manual removal) [7, 8]. To produce such objects, parts of the model would have to be separated and reassembled later.

1.3.1.2.   Material Jetting

The most widely used technology of this type is PolyJet®, marketed by *Stratasys*. Material jetting is based on the same chemical principles as vat polymerization, but these printers do not hold the material in a vat, instead they use a material jet with a similar principle to two-dimensional inkjet printers. Microdroplets of liquid polymer resin are jetted onto the build tray and cured with a UV light according to the printing path. The material is then jetted onto the build platform using either a continuous approach or a drop on demand approach. Once a layer is completed, the build tray is lowered, according to a chosen increment (layer thickness) and the scanning for the second layer (in the x-y plane) begins. In this technology, two (or even more for multi-material printing) sets of print heads are required, for example, one providing the photopolymer construction material and another one providing dissolvable support material. The latter is a gel-like material which is deposited to support the protrusions, jutting parts and complicated geometries. Dissolvable support is then removed, through dedicated removal processes, which go through various steps of soaking in mild soap solutions based on caustic soda (sodium hydroxide), and rinsing; and manually completed, through a pressurized waterjet [10]. Generally, in material jetting no further post-processing is required for the printed parts. Inkjet printers are widely used in medicine, especially for printing detailed anatomical models. Multi-material prints with different colours and different properties for each printed object are also possible. Transparent organ models are often printed with internal structures (e.g., nerves, vessels, or tumours), visible in different colours. In the most modern and advanced high-end machines, the materials can be mixed in each print head during printing. This allows the use of so-called "digital materials" [11]. These are combinations of materials recreated on the digital model to print a single piece with different properties. Likewise, flexible materials can be mixed with other solid materials, which can be used to achieve different hardness and mechanical properties, from flexible (similar to natural rubber) to hard/rigid. To date, short-term

biocompatible materials are also available for the manufacture of surgical/dental instruments and guides for implants [7, 8].

1.3.1.3.   Binder Jetting

The binder jetting process uses two materials, a powder-based material, and a binder, usually in liquid form, which acts as an adhesive between the layers of powder. The binding agent is deposited by a print head, which moves in the x-y plane, to selectively bind the powder deposited on a bed of fine powder, according to the print design for that layer. A roller deposits each new layer of powder to cover the entire print tray. The powder on the running layer is bonded and the build platform is lowered, then the roller moves on to deposit the next layer of powder. Support structures are unnecessary as the model is continuously supported by unbound powder filling the build tray during fabrication. Many binder jetting 3D printers are equipped with a colour print head or binders to get the whole piece in colour or just its outer surface [12]. A wide range of colours can be obtained with this technique by mixing multiple-coloured binders/inks. In making anatomical models, this technique has several limitations. It is not possible to print flexible and translucent models, they have a rough surface finish and are very fragile before post-processing, especially if they are very complex models. Furthermore, the printed models can be composed of a single powder (consisting of gypsum, ceramic or sand). In post-processing the residual dust is sucked/blown to clean the model, which is then strengthened with infiltration of cyanoacrylate, wax, resin, or metals to increase the final resistance of the piece. Binder jetting is therefore used for printing anatomical models with colour coded anatomy, for example, for bone anatomy models coloured according to bone density derived from medical images [8].

1.3.1.4.   Material Extrusion

Material extrusion is also known as Fused Deposition Modelling (FDM) or Fused Filament Fabrication (FFF). The FDM is a material extrusion process, trademarked by the company *Stratasys*. In the aftermath of the *Stratasys* patent expiry, the alternative name FFF was created by 3D printers' manufacturers which used the same processing principle of releasing fused material in layers. In this technology, the material, in the form of filament wound on a spool, is pulled through the print head, and brought to a nozzle heated by a resistance. In the nozzle the thermoplastic filament melts at high temperatures and is deposited layer-by-layer according to the print design. Typically, the nozzle moves in the x-y plane and the build platform moves down (along the z axis) after each new layer has been deposited. Once extruded, the material hardens and cools.

Extrusion printers have one or more heated print heads, which move in a path calculated by the printer driver software (printing path). Most "at-home" and entry-level printers have a single extrusion head that allows printing only one material at a time. In these printers, the support structures are therefore made of the same printing material. In this case, the supports must be detached manually, sometimes with some difficulty. Furthermore, any supports inside the object (for example, for empty anatomical models) are difficult to reach and therefore cannot be removed. Professional extrusion printers, on the other hand, have at least one other print head that allows the use of a specific support material, different from the one used for construction. In such a case, the supports are typically soluble in a bath of hot water and a solvent (e.g., 70° C water solution with sodium hydroxide). Soluble supports are a great advantage in the case of convoluted and hollow medical models, which trace human anatomical overhangs. For these complex models, the supports must be appropriate, otherwise the printing will fail. To date, even for the highest-level printers, soluble supports are not available for all printable materials. Multi-head machines can also be used for printing models with multiple colours and/or materials [13]. The fused filament has a cylindrical shape which depends on the diameter of the nozzle. The cylindrical threads are juxtaposed on the printing surface and superimposed between the various layers. Due to the cylinder shape, the bonding between the parts is partial, with inevitable gaps (named air gaps) in the mesostructure of the piece. However, this 3DP technique is the most widespread and economical for both medical and non-medical applications. It is the most widely used technology for "at-home" or laboratory printers, with widespread use also for research applications in various fields. It is preferred for the greater resistance, durability, and stability of the final parts and for the reduced costs both for machines and materials. It is widely used for the materialization of musculoskeletal orthosis or large bone anatomical models [8], but may not be optimal for complex anatomical models (e.g., models for simulating endovascular procedures, or phantoms for medical imaging) which would require watertightness. In this case, an adequate infiltration process with an appropriate sealant must be identified to waterproof the piece, while varnishes or resins can be used to improve the aesthetic result.

1.3.1.5.   Powder Bed Fusion

This technology uses high-powered lasers or an electron beam to melt small particles of plastic, metal, ceramic or glass, which are carried by a roller to the print tray in the form of powder. The powder is typically preheated just below its melting point. The power source is managed by the printer drivers, which control the target (the path to be drawn) allowing it to selectively melt the

powder into each layer on the powder bed. As soon as a layer has been melted, the powder bed is lowered by one layer thickness, and a new layer of powder is printed. In powder bed fusion, as well as in binder jetting, metallic materials generally do not require support structures, as the model is always completely surrounded and supported by unsintered powder. However, metallic materials may require supports to transfer heat from the printed piece and reduce swelling during 3DP [14]. The most common 3DP techniques based on this technology are Selective Laser Sintering (SLS), Selective Laser Melting (SLM), Selective Heat Sintering (SHS), Electron Beam Melting (EBM), Direct Laser Sintering to Metal (DMLS). These technologies are widely used in 3DP of medical devices, including implants to promote osseointegration, fixings and surgical instruments and guides. The materials are synthetic polymers (such as nylon, polyether ether ketone) and metals (such as titanium and cobalt-chromium alloys), which are biocompatible and sterilizable and can be safely implanted [7, 8]. Furthermore, the main obstacle, when using such technologies for the realization of anthropomorphic phantoms, models for pre-surgical planning, or medical devices, is the difficulty of ensuring the removal of any remaining unsintered powder in any cavities in the printed pattern/parts.

1.3.2. Other Technologies

This section briefly discusses two others popular 3DP technologies, which currently have limited medical applications, to complete the scenario of the 3DP technologies available to date.

1.3.2.1. Sheet Lamination

Sheet lamination is an inexpensive 3DP method that bond paper, metal, or plastic film. Each rolled sheet is pulled onto the build tray, a laser knife (or cutter) traces the outline of the shape of the object to be printed, finally, a glue or heat treatment is applied between the layers for adhesion to the previous layer. To produce coloured models the sheet can be pre-printed in colour. Among the sheet lamination processes, the most common are Ultrasonic Additive Manufacturing (UAM) and Laminated Object Manufacturing (LOM). UAM machines use metal sheets or strips that are bonded together during printing by ultrasonic welding. The process requires additional Computer Numerical Control (CNC) machining for the removal of unalloyed metal. The most used metals are aluminium, copper, stainless steel, and titanium. LOM machines use a similar layer-by-layer approach, but the material is in sheets or strips of paper, which are then glued together. The LOM process uses a cross-hatch method during construction to allow for easier removal of sheet remnants in post-processing [15]. These objects

have a beautiful aesthetic and visual rendering but are unsuitable for structural uses. In both technologies presented, the removal of excess material in post-processing may not be easy (or possible), especially for complex anatomical geometries, such as cavities or areas surrounding tortuous structures (vessels or brain circumvolutions). Mainly for this reason, sheet lamination is currently not found in biomedical 3DP applications. Being economical, it has been used for some orthopaedic applications where it was necessary to evaluate the external bone surface [8]. Despite the economy, printing and post-processing times are prohibitive for more advanced uses in this field.

1.3.2.2.   Directed Energy Deposition

Directed energy deposition is a more complex 3DP process, which is commonly used to repair printed parts or to add material to existing components, but this option is of limited use in medical applications. A large group of 3DP technologies falls under this name: Laser Engineered Net Shaping (LENS), Directed Light Fabrication (DLF), Direct Metal Deposition (DMD), 3D Laser Cladding. The typical directed energy deposition machine consists of a nozzle mounted on a multi-axis arm, which deposits fused material on the indicated surface, where it solidifies. The principle may seem similar to material extrusion, however, in this case, the nozzle is not fixed to a specific axis, so it can move in multiple directions. The material can be deposited from many angles (in machines with 4 and 5 axes) and is melted at the time of deposition with a laser or electronic beam. Materials are deposited directly into the area where a high-power energy source is directed to melt the material, combining aspects of material extrusion and powder bed melting (laser or electron beam) [16]. The materials for this technology are mostly polymers and ceramics, even metals (in the form of filaments or powder) can be used.

1.3.3.   3D Bioprinting Technologies

3D Bioprinting is a form of AM that uses cells and other biocompatible materials, also known as "bioinks", to print living structures that mimic the behaviour of natural living systems [17]. Bioprinting has emerged in recent decades as the intersection of larger fields: AM, tissue engineering, regenerative medicine, and biofabrication. For this reason, the term "bioprinting" encompasses a wide range of technologies for "bioprint" 3D objects that extend far beyond classic 3DP. In the early 2000s, cellular aggregates and spheroids began to be used as bioinks. In early bioprinter prototypes, bioinks were deposited using a modified inkjet printer equipped with luer-lock needles [18], which exploited a droplet-based hybrid technology towards the possible use of

technologies based on spheroids' extrusion. Cell spheroid printing thus became a novel approach for tissue and organ printing where a large number of cells would be required to obtain the densities present in vivo [19]. Since the beginning of 2010, bioprinting has begun to consolidate and this field has undergone considerable evolutions. Advances in the development of existing and new methods for extrusion and droplet-based printing of these materials have been and remain an important focus of bioprinting research. Like those of classic 3DP, each bioprinting technology (e.g., extrusion, droplet-based, and light-based, to name some major categories) has intrinsic strengths and limitations [20]. There has already been a synergistic development of hardware technology and materials to facilitate the printing of bioinks, however, the identification of materials, or material formulations, with properties useful for printing will continue to represent an important direction for ongoing and future research. Existing bioprinting technology has now reached multiscale capability: high resolution capability in 3D space and the ability to address that space across macro-length scales. However, the combination of bioprinting modalities will similarly offer opportunities to design processes that lead to multiple tools to support complex problems, where a single technology may not be optimal to solve all aspects of a problem. Therefore, the bioprinting technology will be further investigated in the future, not only for the aspects inherent in the engineering of tissues and replicas of living organs, but also for developing of functional phantoms of human organs [21].

1.4. Biomedical Applications of 3D Printing

Continued advances in digital 3D and 4D rendering imaging technologies have enabled healthcare professionals to document and visualize human tissues and organs more and more accurately. Likewise, 3D model fabrication technologies are integrated to put anatomical models in the hands of physicians for various biomedical applications.

1.4.1. Why 3D Printing in Biomedical Applications?

Studies to objectively evaluate the clinical utility, efficacy and cost of 3DP applications are currently underway [7, 22], but the impact that this technology is having on both patient care and medical-clinical research is beyond doubt, above all thanks to the possibility to carry out meaningful measurements on physical models of human anatomy. 3DP is one of the most disruptive technologies of recent decades, it has the potential to significantly change clinical fields, improving medicine and healthcare, making care affordable, accessible, and personalized. As printers evolve, numerous scientific journals

increasingly highlight how 3DP now frequently enters various departments of interventional medicine [23], orthopaedics and radiology [7]. The great impact of 3DP in this field is due to the advantages of AM production, compared to the traditional production techniques of subtractive manufacturing [24]. These generally require very expensive and bulky, energy-intensive machinery with large quantities of material waste. Furthermore, traditional casting and in-mould processing methods make customization of medical devices impracticable and, above all, the production of patient-specific models would be very expensive [2, 8]. Similarly, objects with complex shapes, such as anatomical shapes, are difficult to make with conventional techniques. In 3DP, however, the production of 3D models is no longer constrained by design complexity [2, 24]. It provides structural freedom to designers without production constraints, while offering a significant reduction in costs and waste. This is particularly useful and effective for biomedical applications that require the creation of 3D objects, sometimes very complex in terms of shapes, geometries, and internal structures (e.g., models for preoperative planning, anatomical phantoms for imaging, customized devices, and prostheses, etc.). The promising frontier of 3DP in medicine involves exploiting this freedom in the production of anthropomorphic forms and improvements in the techniques of acquisition and segmentation of medical images. Some details of the anatomical structures and the same anatomies, when very convoluted, would not be otherwise reproducible in physical objects. Indeed, starting from the patient's medical image data, 3D models can instead be customized before fabrication to be used for a variety of purposes [7]. 3DP will therefore be increasingly beneficial for biomedical devices, designed according to the specific needs of research (such as, imaging phantoms) and clinical practice (such as, presurgical planning), up to patient-specific tissue engineering and bioprinting.

1.4.2. Main Applications

Between all the sectors in which 3DP is used, biomedical field requires extreme customization and still a lot of research. 3DP has been used in the wide range of healthcare settings, including cardiothoracic surgery, cardiology, gastroenterology, neurosurgery, oral and maxillofacial surgery, ophthalmology, otolaryngology, orthopaedic surgery, plastic surgery, podiatry, pulmonology, radiation oncology, transplant surgery, urology and vascular surgery [2]. The main direct applications of 3DP in biomedical field are the following:

- personalized treatment and preoperative planning;
- customized surgical tools and prostheses;
- testing of different devices in specific pathways;
- medical education and training;

- patient education to improve the doctor-patient communication;
- personalized drug 3D printing;
- study of osteoporotic conditions;
- bioprinting and customized synthetic organs.

Although 3DP offers great potential for manufacturing, 3DP products do not yet have a defined legal status, not even in the biomedical field for both implantable and non-implantable devices. All 3D-printed products are classified as custom-made devices under the Regulation (EU) 2017/745 of the European Parliament and of the Council of 5 April 2017. Manufacturers of custom-made devices shall only be guaranteed by an obligation of conformity assessment procedures upon which the device shall be compliant with safety and performance requirements [2].

1.4.3.   3D Printing to Support Radiology

3DP in radiology broadly includes the manufacture of anatomical structures represented on medical images. The present work placed in the context of 3DP in radiology, focusing on morpho-functional medical imaging applications based on anthropomorphic brain phantoms (**Section 2.3.3**).

Before the introduction of 3DP in radiology, physicians did not have effective tools for materializing the anatomies they saw in the medical images. Their only option was to rely on two-dimensional images, for example, to define diagnoses and plan surgeries, or to perform quantitative technical evaluation (quality control, equipment calibration) on radiological medical imaging devices. To date, clinicians can instead be provided not only with a 3D virtual model (tracing an exact segmentation of the anatomy of interest), but also with a physical model that can be created through 3DP, which can reproduce the human anatomy with extreme precision and attention to detail (as will be explained in the **Section 2.2.3**). In this context, the "3D radiology laboratories" were created by academic radiologists to develop and implement software tools to reformat diagnostic images, most commonly from Computed Tomography (CT) and Magnetic Resonance Imaging (MRI), in anatomical 3D models as opposed to traditional imaging. As a first step, 3D rendering of anatomical volumes reproduced on a two-dimensional monitor enabled 3D visualization of anatomy and pathological conditions, which largely influenced radiology and provided an important new method for radiologists to communicate relevant measurements and pertinent findings on specific anatomies to medical care teams. The further development of advanced 3D visualization on screens (obtained processing the voxels of the medical images) prompted the idea of bringing the 3D model into the physicians' hands [25]. Therefore, "3D printing laboratories in radiology" have been emerging, with some parallels and differences from the early 3D laboratories [7].

However, 3D printers do not directly accept medical images (such as DICOM or Nifty) or 3D rendered models, but single objects or parts defined by surfaces that enclose a region of space in a vector format suitable for 3DP (discussed in **Section 1.5**).

1.5. Communicating with a 3D Printer

Creating 3D-printed models requires additional basic knowledge and mastery of technical skills to generate unique printable file formats recognized by 3D printers. There are two main phases in the development of a 3D object, prior to printing, which are the modelling phase and the slicing phase. In this section, it refers only to the design phases that arise in the context of anatomical 3DP. Another fundamental step in the design workflow is images segmentation, which will be contextualized and discussed in more detail in **Chapter 3** and **Chapter 5**. Modelling is the phase in which, starting from the images, the project of a digital (vector) 3D model comes to life, consisting of all the information that characterizes its shape, dimensions, and project specifications. The information contained in the digital model must therefore be in a format suitable for 3DP (the STL format, referred to in **Section 1.5.1**). After that, the model must then be translated into a language that the 3D printer can understand, obtaining a new file that includes all the instructions that the print head must perform to obtain the print of the piece on each layer. In this phase, the model is sliced using specific slicing software for 3D printers (referred to in **Section 1.5.2.1**) in a series of slices (horizontal planes), corresponding to the layers deposited during printing. The complete workflow of this work is summarised in **Appendix, Flowchart (A)**.

1.5.1. The STL Format and Beyond

The 3DP process begins with the creation of a digital model, which can be generated using a variety of Computer-Aided Design (CAD) software. Digital models are limited by 3D surfaces enclosing a region of space. A 3D printer produces these three-dimensional objects by filling (compactly or porously, according to defined infill patterns) the space enclosed by each of the surfaces with a solid material. The material is deposited, *layer-by-layer*, by the print head, following the printing path described by the surfaces of the digital model. How these surfaces are described and stored in a digital file is therefore a key concept to understanding and using 3DP. The standard file format for defining the surfaces of a 3D model is the Standard Tessellation Language (alternatively, Standard Triangulation Language), commonly referred to as STereoLithographic file format, abbreviated to STL. The STL format represents

geometry via tessellation (facets), a simple approximation technique in polygonal mesh (hereinafter, also referred to as mesh) to cover a surface with a collection of geometric shapes (e.g., triangles, polygons), which fit perfectly with no overlaps, gaps, or holes. After that the geometry of the 3D model is encoded through the three unique vertices an one normal of each planar triangle. An ASCII (American Standard Code for Information Interchange) or a binary STL file is generated storing the encoded geometry in ASCII or binary codes. ASCII STL files are human readable but taking up more storage space than binary STL files, which are not easy to read, but need less storage space. Binary STL files can only describe a single part, while ASCII STL files can contain multiple independent parts. STL files are ideal for printing a single object (e.g., an organ, a phantom, an implant, a guide, or components) with a single "thickened" surface, but more difficult is the design of an STL of a 3D model with multiple surfaces (or parts) with different material properties and/or different colour. For example, in the case of an anatomical model that must represent several tissues (touching each other), the operator generating the STL files must not only ensure that the tissues described in the files accurately represent the anatomy, but also that the two tissue surfaces touch along a single side of each of the two surfaces described by the STL files, without leaving any space between them (aspects addressed for our application in the **Section 3.3.2**). If these aspects were not considered in the design phase, the anatomical model would not faithfully represent the physiology, and the 3DP would not be possible. However, the STL format, although widely used, still has a number of limitations (discussed in the following **Section 1.5.1.1**) that could also greatly complicate the design. Recently, ASTM International approved a new format called Additive Manufacturing File Format (AMF) [26], which has been designed to overcome many of the limitations of the simple STL format, especially to follow the development of the potential of 3DP machines in the future. The AMF format, when it will be more widespread, will allow the user to incorporate features (including surface texture, colour, and material properties) into the digital file of part to be printed.

1.5.1.1. Mesh Refinement and Correction

STL files could present some problems once generated. Therefore, before printing, it must be checked that polygonal meshes are free from errors. This verification is essential because it is the only way to ensure that the digitally designed 3D model can actually be materialized by 3D printers. In contexts other than 3DP, such as in simple 3D volume rendering, polygon mesh verification is not required. In these cases, it may happen that 3D scenes contain objects that would be not actually printable, with senseless topologies, bad

meshes and duplicated vertices but still this would not invalidate the 3D rendering results. If the model is to be 3D-printed, the question becomes completely different. If the correctness of the mesh is not verified, the 3D printer may encounter a polygon that does not meet the criteria for completing the print (printability requirements, **Section 1.5.1.2**), and the print would fail, resulting in waste of time and material. Therefore, before printing the polygon mesh must be imported into software that evaluates its errors to ensure its manifoldness. The term "manifold" is a mathematical term to describe the topology of a virtual object (it will be better defined in **Section 2.2.3.1**). Basically, it means that the object must be continuous inside and outside (i.e., without holes and having a positive – not zero – volume). Errors in the mesh may occur as the computer generates the triangles of the discretized surface. On the other hand, when creating a model for 3DP, various software is used in the different stages of processing the model. Therefore, it is necessary to establish in advance a valid operating procedure, scrupulously checking each phase of the workflow, to avoid too many steps before arriving at the final STL file. Each model refinement step could introduce errors, when the errors are numerous it is no longer possible to fix them.

1.5.1.2. Printability Requirements

They are closely related to the geometric and topological description of an anatomical 3D model extracted from medical images (aspects that will be explored in **Section 2.2.3.1**). The printability requirements for having a polygonal manifold mesh are shown below.

Absence of inverted normals. If the 3D model defined in the STL file contains an inverted normal, the interpreters (slicing software – **Section 1.5.2.1** – and 3D printers) are not able to determine the inside and outside of the object. Mesh triangles have an orientation on each external and internal face. A normal inverted is an inverted (inside-out) triangle whose outside face points to the centre of the part (towards the inside). All triangles must have the normal pointing towards the outside of the object, since if all the triangles of an object are inverted, the slicing software could interpret the part as having a negative volume, which is not compatible with printing (**Figure 1**).

Absence of overlapping or intersecting triangles. The outer surface of an object cannot intersect with itself (i.e., only a triangle can exist at a given coordinate) in the physical space. This error arises during the connection of discrete surface points of a volume segmented into triangles, but in an orientation whereby the triangles themselves intersect (**Figure 2**). While if two triangles overlap, there is a redundant element which, in addition to the use of memory, means that the

outside of a triangle is inside the volume of the piece, making the solid non-manifold.
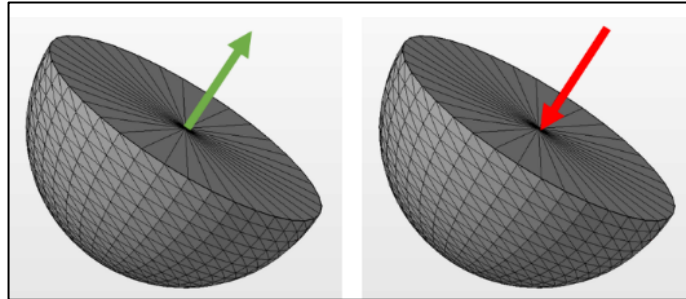
Figure 1 – Half sphere STL model with normal vectors. *The cut surface of the half sphere must have a normal outgoing (green arrow) from the surface. In this way the printing software can discriminate the inside and outside of the object. If the normal was inverted (red arrow), the software would swap the inside of the object with the outside and the printing could not be completed.*

Absence of extra edges or faces hidden within the 3D structure. Since each triangle has an "inside" and an "outside" in the 3D structure, an "inside" and an "outside" of the part are defined. Extra edges or faces in the 3D object (or inside the internal structure of the object) are not visible on its external surface (**Figure 2**), and they may be thin and therefore not evident, however, leading to problems in printing. This error can arise, for example, from Boolean operations between two objects and should be avoided because it involves redundant information that does not correctly define the surfaces of the object.

Absence of bad-edges. All sides of the triangles that form the surface must be properly connected to each other. Each polygon must share edges with adjacent triangles with no gaps between them. Polygons that do not share surfaces are called bad-edges (**Figure 3**).

Absence of non-manifold shells. Shells touching at a single point, single line or a single plane are non-manifold. The point/edge/plane of connection could be from a mathematical point of view infinitesimally thin and therefore have no volume, which would mean not printable. There must be a very small connection between the objects, but not null. More specifically, these problems can be referred to as non-manifold edges and non-manifold vertices (**Figure 3**).

Watertight mesh. The mesh must have a contiguous surface of triangles without holes (absent triangles), which instead should be on the inner or outer surface of the mesh. Even if the object is hollow, the inside of the excavated part must be "coated" with triangles to be watertight. Surfaces in a 3D space (without a thickness) are not printable, therefore, even an empty object must always have a printable wall thickness. In 3DP, only real solid objects are created and in

designing them they must be imagined filled with water without any drops coming out.
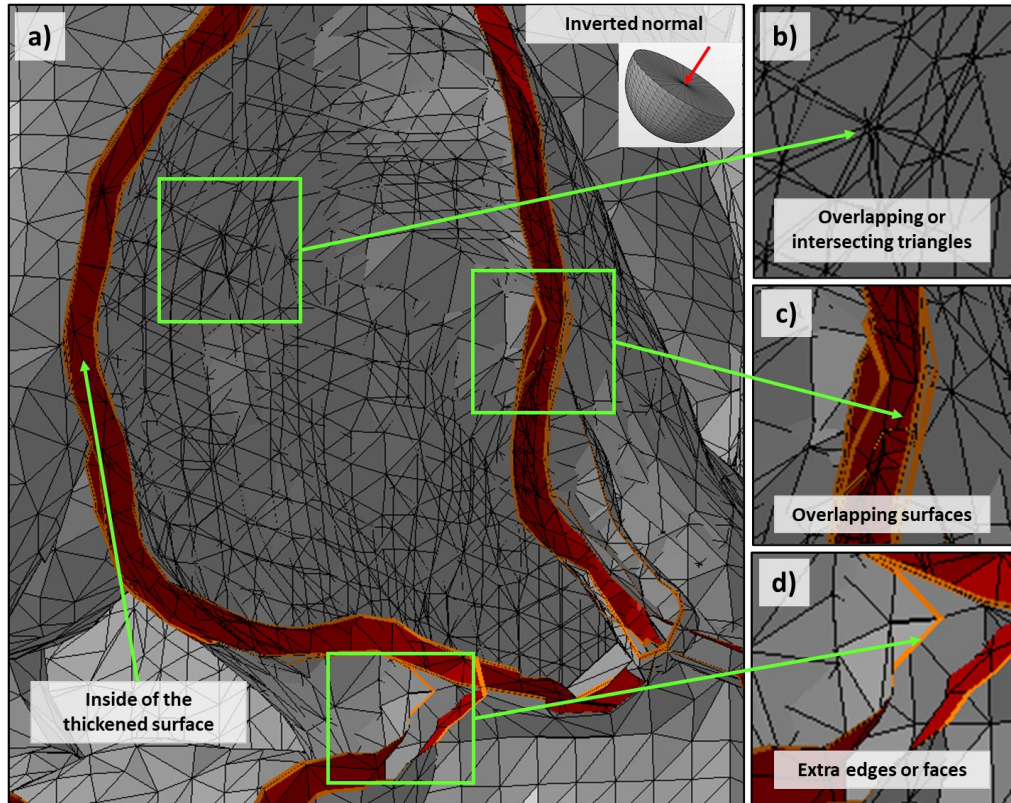
Figure 2 - Examples of typical errors in polygonal meshes. *The figures show the inside of the "thickened" surfaces in red, the outside in grey and the edges in orange. (a) Non-manifold mesh with inverted normal and several errors; enlargements of the panel (a) showing: (b) overlapping and intersecting triangles; (c) overlapping surfaces (in orange) and (d) extra edges or faces. These errors cannot be corrected easily, rather their generation should be avoided.*
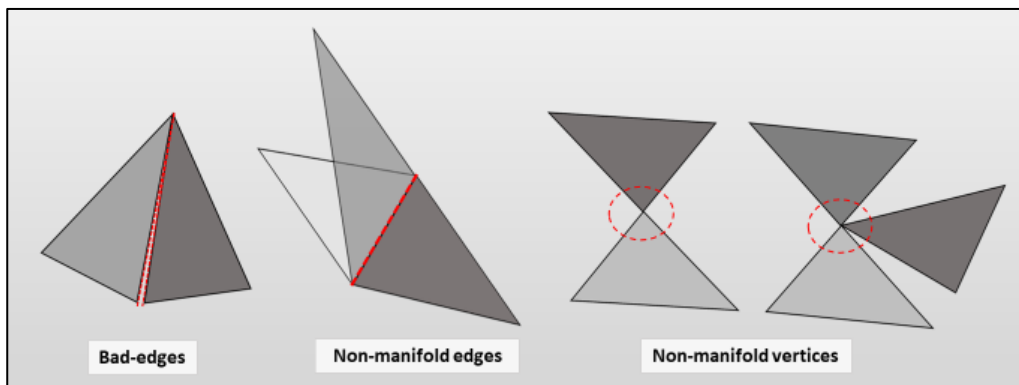
Figure 3 – Representation of bad-edges, and non-manifold edges and vertices. *The bad-edge example shows two neighbouring triangles that do not share all the points along the side. In the example of non-manifold edges, edges shared by several disjoint triangles are identified, while in the non-manifold vertices example, vertices shared by several disjoint triangles are identified.*

Absence of noise-shells. This problem might arise when extracting STL models from medical images. Noise shells are unintended/unwanted islands of a three-dimensional shell (a series of joined faces) separated from the main shell/mesh, which could be erroneously segmented as belonging to the object to be created. Eliminating noise shells decreases the number of errors that can be found, and corrected, and makes printing the model less difficult.

1.5.2.   Prepare, Slice and Print

Another limitation of STL files is that there is no portable standard across software to store the intended printing parameters, material properties and colours for a model. 3D printer-specific software is used to assign these properties to each STL file loaded for printing, which can be a long and error-prone process, if there is a discrepancy between the project specifications and the technical characteristics set during the slicing phase (these aspects will be addressed for our application in **Section 4.3**). Indeed, STL model must be translated into a decodable "language" for the 3D printer.

1.5.2.1.   Slicing software

Slicing is a further modelling step aimed at 3DP that placed in an intermediate position between the STL modelling of the (digital) object and the production of the (physical) object. In this phase, the model is divided into a series of "slices" of defined thickness, which will be the layers deposited one on top of the other during printing. For each slice, the software defines the deposition modalities and the print head path for each single layer. CAM (Computer-Aided Manufacturing) software is required to convert the STL file into a series of instructions in language (generally, G-code) for the 3D printer. CAM software is programmed for Computerized Numerical Control (CNC) machines that are used to build an object. The movements during construction are directed by a microprocessor (inside the machine) which controls them according to a specific programming language. In the case of 3D printers, it is not necessary to use complex CAM software. For 3DP there are easy-to-use slicing software (also called slicers), which are used to convert the 3D model into instructions interpretable by the 3D printer. The instructions concern the movements that the head and/or the printing plate must follow on the x and y axes; the deposition of the material and the support; the printing speed and, where required, the temperatures. Movement on the z axis, on the other hand, occurs only in the transition from one layer to the next to materialize the model. The thickness of the layers, defined in the slicing phase, is usually set by the user according to the technical characteristics of the object to be printed, from the desired quality of

the mechanical resistance of the printed object. There is much software (open-source, free access, commercial or proprietary) for this type of operation, created for specific printers, or more generally compatible with other and different machines. The slicing software is generally proprietary for professional 3D printers (e.g., *GrabCAD Print* and *Insight* for *Stratasys* printers), while for semi-professional or entry-level printers there are valid alternatives (e.g., *Simplify3D*, *Slic3r*, *Cura*, *KISSlicer*, *ideaMaker*).

1.5.2.2. Printing parameters

In the slicing process, the printing parameters are set and optimized. These are the attributes that during (and after) printing, can affect the production speed, as well as the appearance (and behaviours) of the printed object. Based on the user settings, the slicing program calculates the most efficient path (both in terms of processing time and surface finish) that the 3D printer will have to do to obtain the best result for printing. This path is generally described in G-Code language and at the end of the computation it can be saved in the format readable by the chosen 3D printer. However, the parameters that can be set are numerous and interrelated. Their definition, unfortunately, does not follow fixed rules, especially due to the many variables, sometimes unpredictable, that occur during the printing processes. Therefore, only a meticulous study of the same, a careful analysis of the slicing result and the printing attempts (especially, in the case of more complex models), can lead to define a fair compromise between the possible options and the desirable characteristics for the printed object (in **Section 4.3**, these aspects will be addressed for our application). Furthermore, they vary greatly across the various printing technologies. For some of them, it is not possible a high customization of the printing parameters, while for others, such as the FDM, the user has the possibility to configure many more printing parameters, compared to the default setting. For the various 3D printers there are in fact many errors related to the slicing process that determine the success of the printing, some related to the specific technology and the characteristics of the printing materials. In SLA or FDM, the orientation of the piece relative to the print bed can also affect the success of the print, even sometimes due to inadequate positioning of the supports. Since these errors (and the consequent printing defects) are related to the specific model to be printed, once the printing parameters have been set, the slicing results should always be inspected, at least visually, to verify their appropriateness. The main printing parameters, common to the various printing technologies, will be described below. Other parameters specific to the FDM technology will be described for the slicing of the phantom designed in this thesis (see **Section 4.2.2**).

Layer Height. This parameter defines the thickness (in inches or mm) of each layer in which the 3D model is sliced. The print quality increases with a lower layer height, leading to objects with a smoother surface and more visible details (in the z direction, height of the model), but increasing the printing time (proportionally to the height of the layer).

Wall Thickness. This setting adjusts the thickness of the walls of the model. Depending on the type of material deposition, the slicing software approaches the set value as much as possible. For example, in FDM technology, it calculates how many walls must be printed with the specific nozzle depending on its diameter. In general, a thickness of 2 or 3 times the width of the printed line in one deposition is sufficient to create a robust and watertight pattern. The minimum vertical wall thickness recommended by printer manufacturers of various technologies is approximately 1 mm. Lower wall thicknesses can be printed in PolyJet and FDM setting specific options to fill the airgaps in the walls to be printed (see **Section 4.3**).

Retraction. It is used to prevent dripping of the material or the release of threads when moving from side to side of the object to be printed without deposition of material. For each technology, and printer, there are different retraction strategies. These are designed to avoid the annoying stringing phenomenon of older generation printers.

Top/Bottom Thickness. In some technologies, such as FDM, this parameter gives a better adherence of the piece to the printing bed and therefore a higher quality of the surface finish of the first and last layer of the printed object. It should be a multiple of the layer height and high enough to ensure that the parts of the top and bottom layers are completely closed. Where possible, it is important to set it properly especially for the top to prevent the pillowing problem (i.e., the presence of imperfections on the top layer).

Infill Density. It is usually a percentage value that expresses the quantity of internal filling of a solid, defining the amount of material used within the compact parts of the printed object. There are various filling patterns (grid, honeycomb, lines), specific to the technology and strength characteristics of the printed piece. Generally, 100% filling is not recommended, except in specific cases where it is required by the product specifications, because it would result in a waste of material and time.

1.5.2.3.   Support structures generation

In slicing software, it is possible to choose the orientation of the model on the print bed and generate the support structures. This choice is not trivial and can

often influence the success of the 3DP project, with some *trial-and-error* required for judicious positioning of the support structures. Since supports are related to the particular model to be printed, 3D models should at least always be visually inspected after supports generation, before being printed [27]. Following this practice, we can first move the piece in the virtual three-dimensional space to understand which positioning will allow limiting the number of supports. Then, we can perform the slicing, checking on the various layers that all the critical points are supported, especially in very convoluted models. Less number of supports will result in a smaller quantity of deposited material, a condition that implies less waste, and a shorter printing time, often managing to maintain the same quality of the final product. However, it is not always correct to assume that the best orientation is the one with the least number of supports [28], much also depends on the functionality of the object and on how the supports automatically generated by slicing software are able to support even the critical points. Depending on the slicing software used, it is possible to choose between different support configurations and this allows a great customization of the printing process. There are different types of supports, with shapes (tree, grid, line, honeycomb) that are better suited to some types of models than others. Supports are often printed in special soluble materials, so that they can be dissolved in the post-printing phase before any further finishing of the piece. Slicing software propose different useful settings according to the needs. It is possible to choose whether to print support structures everywhere or only for the external parts above the print bed; or set a maximum overhang angle beyond which supports will be generated, helping increase or decrease the amount of needed supports. Furthermore, a higher density of supports can be fixed (in terms of infill density and/or number of supports) by increasing the resistance of the latter to prevent them from breaking during printing and/or the number, in both cases however they will be more difficult to remove. It is also possible to set the minimum distance between the end of a support and the print itself, thus facilitating supports' final removal. Generally, there is no fixed rule in defining them, therefore it remains a personal choice of the designer, who can follow some basic considerations, which are explained below and summarized in **Table 1**.

Overhang Angle. A 3D model generally has different levels of inclination with respect to the printing bed, the closer a part is to be parallel to the printing surface, the more difficult it is for it to support its own weight, if not properly supported. In FDM supports must be created whenever there is an inclination greater than a specified limit value. For example, if we decide that the limit value is 30°, setting the perpendicular to the print surface as the zero angle, then all areas with a greater inclination will have supports to support them. There is no

absolute valid or always correct value, however, a limit value of 45° will almost always be a good choice. SLA and DLP printers require the use of supports to ensure that the prints adhere to the print platform. In this case, the orientation of the parts plays a crucial role on where the supports for the print are located. By reorienting a part, the amount of supports (and therefore the cost of printing) can be drastically reduced. In material jetting, support material is needed in all cases where there are overhanging parts, regardless of the angle. In binder jetting and SLS there is no need for support structures since the powder acts as support when the object is built up layer-by-layer.
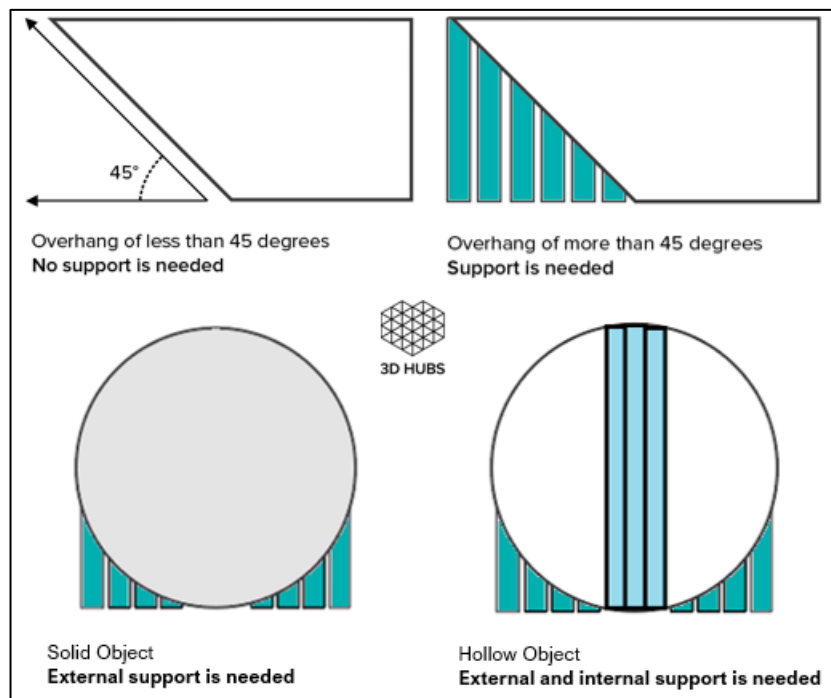
Figure 4 - General rule for setting the overhang angle in FDM. As also suggested by 3D Hubs (https://www.3dhubs.com/knowledge-base/supports-3d-printing-technology-overview/), overhangs greater than 45° must be supported. In our experiments, we also arrived at an overhang angle of 60° without printing issues. An important problem is also that of internal supports. They risk being too many for hollow anatomical structures, and therefore difficult to remove.

Support removal. A common mistake is to assume that the slicing program creates easily removable supports in any case. Unfortunately, this is not the case. The task of slicing software is only to create supports for the critical areas that it automatically identifies starting from the set overhang angle. For this reason, the slicing software may also provide supports that are not easily reachable or removable. To prevent this, before printing, it is necessary to visualize the file produced by slicing and make sure that there are no supports positioned in unreachable areas or that, during removal, could damage the model. This problem can be managed for technologies that have actual support structures,

such as FDM, SLA and DLP. In these cases, the designer can intervene as appropriate to modify the support structures. However, this is not possible for technologies that use support material, such as in material jetting, SLS and binder jetting. In material jetting the gel-like support, although soluble by means of a waterjet, is not always reachable. In SLS and binder jetting, the support powder may become trapped in the cavities of the object, without being able to remove it.

Residual marks of the supports. Consequence of the actual support structures could be the residual marks that they leave once removed. Attention should be paid to this aspect if the aesthetic is important, when printing in FDM, SLA o DLP. It is good practice to use the supports in less visible areas or in large and flat areas in order to eliminate residual marks by smoothing them with sandpaper. This problem does not exist in material jetting, SLS and binder jetting printing. In this case, the supports cannot affect the surface quality and the properties of the parts.

Table 1 - 3DP supports features. Summary table of the specifications and characteristics of the supports for the main 3DP technologies.

3DP Technology	Support required	Overhang Angle	Support removal
FDM	Dependent on model geometry	40°-60°	Manual or dissolution (by immersion)
SLA and DLP	Always	19°-30°	Manual
Material Jetting	Always	Not applicable	Dissolution (water-jet)
Binder Jetting	Never	Not applicable	Manual (air gun)
SLS	Never	Not applicable	Manual (air gun)

1.6. 3D Printer Resolution, Accuracy and Reproducibility

The resolution of a 3D printer represents the minimum movement that the machine can make on each axis. Since printing occurs in three dimensions, three resolution measures must be considered: the z resolution (layer thickness) and the planar x-y resolution [29]. The x-y resolution parameter is an objective fixed

data, which depends on machine specifications, the minimum layer is instead a value suggested by the manufacturer.

The z axis resolution of the printers ranges from 0.05 to 0.30 mm. However, often only one resolution range is indicated in all three axes and, for this reason, generally, manufactures indicate that the highest resolution with 3DP modalities is roughly 0.05 – 0.10 mm in all three axes, which is higher than that of most clinical images. Similarly, to the slice thickness in medical imaging systems, the layer thickness is also user selectable for most 3D printers (see **Section 4.3.2**) and, likewise to medical imaging protocols where slice thickness directly affects acquisition time, its choice directly affects the printing time. For thinner layers, the printheads or power sources will have to deposit proportionally more layers and printing will take a proportionately longer time. Partly due to its impact on print time, layer thickness is the size of 3D printers with a lower resolution (the minimum layer thickness is generally higher than the x-y resolution). Typically, material extrusion printers print with a layer thickness of 0.1 – 0.4 mm; vat photopolymerization printers with a layer thickness of 0.02 – 0.2 mm; material jet printers can print layer thickness up to 16 μm; and the binder jetting layer thickness is typically 0.05 – 0.1 mm.

Resolution is the smallest scale that a 3D printer can reproduce, and it is a factor that affects accuracy. The greatest accuracy is achieved when the printer resolution is the lowest in each of the three axes. The accuracy refers to the degree of agreement between the dimensions of the printed object and the expected ones (the dimensions of the digital object stored in the STL file) [29], and, although the accuracy and reproducibility of medical models for 3DP are not been studied in depth, unsatisfactory accuracy is the most reported drawback of 3DP technology [7]. Current technologies allow 3D models to be created with accuracy within the limits of clinical imaging spatial resolutions, however this is not always possible in practice, as various factors at each stage of the 3DP process contribute to model inaccuracy, including the inherent limitations of each printing technology. Errors that occur during the imaging, segmentation, post-processing phase, before 3DP, also contribute to inaccuracies. Evidence to date indicates that the entire process (workflow) for designing and printing a 3D model must always be performed in a way that limits inaccuracies to clinically acceptable levels [7, 25, 29]. Indeed, a printer with the highest accuracy is not always necessary. The required level of accuracy depends on the clinical purpose. Another aspect to note is that the underlying processes performed by 3D printers (e.g., chemical reactions, heating, and cooling) can cause model-specific dimensional errors. For example, FDM printed parts are susceptible to shrinkage and warping during the thermoplastic cooling process. This can lead to geometric inaccuracies in portions of the model that are not adequately supported during printing. Therefore, regular accuracy testing of a 3D printer,

and recalibration of preventive maintenance, is a necessary part of quality assurance protocols, similar to those used for medical imaging devices.

1.7. 3D Printing Materials

Regarding the materials for 3DP, a large discussion section should be opened in order to comprehensively cover them. However, this goes beyond the purposes of this thesis work. It will be enough for us to discuss the most popular 3DP materials, also studied and used for the development of techniques to make anthropomorphic phantoms.

Plastics. Thermoplastic materials are used in FDM technology. Acrylonitrile-Butadiene-Styrene (ABS) is the plastic material most used by 3D printers, along with Polylactic Acid (PLA) [30]. It is the cheapest material on the market, which partly explains its wide use. Another advantage is the high heat resistance, which allows the creation of rather durable components, compared to other materials. ABS also has some disadvantages that need to be considered. First, during the printing process there is emission of potentially dangerous fumes and therefore an adequate ventilation system is necessary. In addition, the material tends to deform with cooling, so a heated printing bed is essential during printing to maintain the final shape of the piece. ABS is one of the leading materials for FDM technology, this plastic is processed at a temperature ranging from 215°C to 250°C and the average printing speed is from 30 to 80 mm/sec, depending on the machines used. Its characteristics make it suitable for the creation of small parts or to create products resistant to impact and wear. Then there are some variants of the basic ABS material, such as PC-ABS (PolyCarbonate-ABS), which allow for better performance at a higher cost.

Another material widely used in FDM technology is PLA, which certainly has low cost, mechanical strength, and the absence of some of the ABS problems among its advantages. PLA can be obtained from some plant-based materials, such as corn starch or other (waste or algae). Therefore, PLA is more compatible with the environment and biodegradable. Furthermore, no particularly toxic substance is released during the printing process and there are no problems in maintaining the shape of the pieces. Therefore, in the use of PLA no special precautions are required as for ABS-based printing. On the other hand, precisely because it is a biodegradable material there is a risk that it deteriorates very quickly, both because it absorbs the moisture present in the air and due to exposure to ultraviolet rays. PLA is processed at a temperature ranging from 160°C to 220°C (lower than ABS) and can be printed at rather high speeds, from 60 to 200 mm/sec. However, objects in PLA are more rigid, and therefore can more easily break (especially if with very low vertical wall thickness), than those in ABS which are more flexible. As for ABS, there are variants of the basic PLA

that allow obtaining a higher print quality, of course the cost increases proportionally (up to more than double compared to a common PLA filament). ABS and PLA are used, especially in material extrusion printing, due to their ductility and the characteristics that give the final object resistance to heat, chemical agents, mechanical stress, and humidity. For entry-level or semi-professional dual-extruder printers, attempts are being made to use Polyvinyl Alcohol (PVA), a water-soluble synthetic polymer material, as support material for PLA. Immersed in hot water for a couple of hours, the PVA disappears completely, but it is really very difficult to print, the reason why it is not yet suitable for printing complex models, such as anatomical ones. It is non-toxic and stable in terms of performance. The printing temperature is between 180° C and 200° C. High Impact Polystyrene (HIPS) is instead proposed as a support material for ABS. It is a thermoplastic material consisting of polystyrene and styrene-butadiene rubber, which therefore has mechanical characteristics similar to ABS in terms of resistance and extrusion temperature. It dissolves completely when immersed in limonene, properties that make it a good material for printing supports of particularly complex structures. Unlike PVA, HIPS has excellent printability, and it can also be used as construction material. For high-end commercial printers, the support materials are generally proprietary, so their exact chemical composition is not always known. For *Stratasys* ABS, the supports dissolve in a calcium hydroxide solution, while for PLA, PLA (non-soluble) supports are provided. Among the flexible thermoplastics it is worth mentioning the Thermoplastic Polyurethane (TPU), which does not emit fumes or unpleasant smells during extrusion, and has remarkable properties such as elasticity, transparency and resistance to abrasion and oil repellence. However, this material is not commonly used in biomedical 3DP applications. A particularly innovative material in the context of FDM 3DP is nylon, a material from the family of synthetic polyamides. It has particularly interesting mechanical properties. It allows the production of resistant and flexible objects, able to withstand strong vibrations and repeated stresses. However, it has some problems: sensitivity to humidity, risk of deformation during the printing process, printing temperatures often above 250°C (difficult to reach with lower cost machines). Furthermore, a more recent thermoplastic, widely used in 3DP (especially entry-level), is the Polyethylene Terephthalate Glycol-modified (PET-G). The interest in this material stems from its transparency, low shrinkage rate, high impact resistance, high mechanical strength, and high chemical resistance. It is particularly durable, and considerably more flexible than PLA and ABS, but also softer. It combines the functionality of ABS (temperature resistant, more durable) and the reliability of PLA (easy to print) in a single material. The adhesion of the layer is generally excellent, although PETG is not immune to problems, as it suffers from stringing. Being difficult to break it, if

the object to be made is a container or a casing that must have characteristics of high resistance, PETG is the most suitable material, since nylon presents greater printing difficulties and higher costs.

Resins. The resins are used in vat photopolymerization (SLA, DLP) and material jetting technologies. Polymeric resins are made of viscous material, which requires continuous (in each points) support when printing [2, 30]. The need for continuous support is what could limit the use of resins in very complex anatomical models with many internal structures and projecting parts. Vat photopolymerization always requires any supporting structures during the manufacturing process (**Table 1**), whose manual removal is not always easy. Even material jetting always needs support, but it is made of soluble material and removed with a waterjet (**Table 1**). What makes resins remarkable for biomedical applications is the large number of different and complex polymers obtainable with a variety of methods and raw materials. Furthermore, objects printed with resins usually have a high level of detail and precision. Resins allow producing colour prototypes and/or composed of materials with different consistencies. Professional 3D printers that use resins can reproduce even complex shades and textures (combining different materials in appropriate quantities), as well as use rubbery/rigid-transparent/opaque materials.

Chapter 2

Anthropomorphic Brain Phantoms

2.1. Introduction

Imaging phantoms are test objects used for dosimetry measurements, for highly specialized quantitative technical evaluation on radiological medical imaging devices (quality control, equipment calibration), and for education in medical imaging. Generally, a distinction is made between calibration and anthropomorphic phantoms. Calibration phantoms are often cylinders or plates of already known densities, used in quality control to ensure that the same expected density values are reproduced in images reconstructed by imaging devices. Deviation from these values may indicate the need for recalibration and service for imaging equipment. Anthropomorphic phantoms are much more advanced objects for simulating patients to medical imaging. These phantoms are those of interest for this work and will be explored further below.

2.2. Anthropomorphic Imaging Phantoms

Anthropomorphic phantoms are objects that simulate human anatomy, made of materials with similar characteristics to normal tissues of the human body. The first phantoms were designed to carry out dosimetry studies on ionizing radiation, clearly not always possible on patients. Due to their resemblance to real patients, these phantoms can be used for a variety of tasks. Rather than image multiple patients, anthropomorphic phantoms can be used for *trial-and-error* to evaluate the optimal use of ionizing radiations in new protocols or image reconstruction techniques [31]. Hence the increasing need to have anthropomorphic phantoms in which the physical, geometric, and physiological information of a real patient was enclosed (**Figure 5**). In the wake of technological innovation, first there was an evolution in the 3D modelling of human anatomy from medical images [32], while recent advancements in 3DP technology are improving the development of physical anthropomorphic phantoms to better mimic the anatomical structures of patients [31].
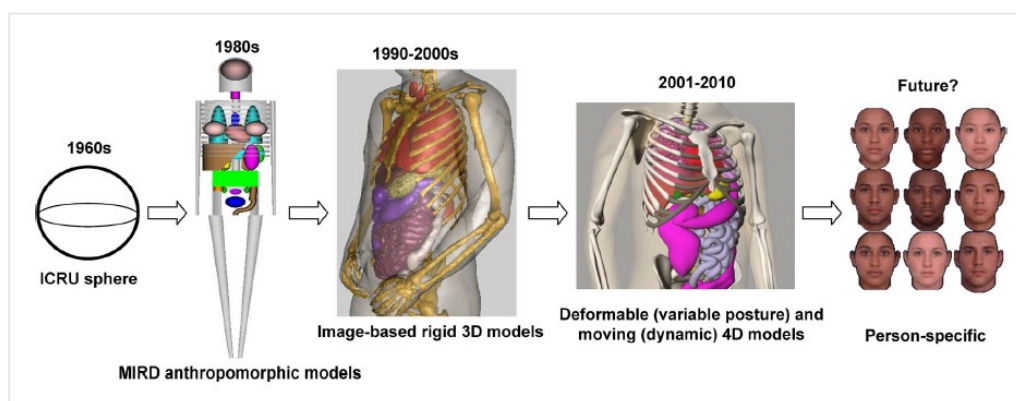
Figure 5 - Evolution of 3D models of human anatomy. From the first and very simple spherical model (ICRU sphere) to the more realistic and complex computational models (even, person-specific phantoms in the future) [32].

2.2.1. Stylized Phantoms

Early generation of computational phantoms was developed to meet the need to better evaluate the doses received by an organ or tissue following the introduction of one or more radionuclides into the body. As a first approximation, earlier efforts aimed at producing, very simple models. Each organ of the body was usually represented as a sphere with a certain radius, different for each one (e.g., ICRU sphere, **Figure 5**) [32]. Other stylized phantoms, such as *Shepp-Logan*'s [33], were used as models for the human head in the development and testing of image reconstruction algorithms. Over time, radiologists have tried to model the single organs of the body and, also, the entire human body in an increasingly realistic way. These efforts led to the creation of the early stylized anthropomorphic phantoms that best traced the human anatomy. For the realization of these objects, the classical techniques of Constructive Solid Geometry (CSG) were used, according to a volume-based model of representation of 3D objects [34]. In this approach, the shapes were built starting from a family of elementary geometric solids (called primitives, such as the parallelepiped, the cylinder, the sphere, the cone, the torus, the ellipsoid). The primitives could be finely tuned and adjusted by changing the parameters of the mathematical equations based on the volume, position, and shape of the organ to be represented. For simplicity, most of these phantoms were considered filled with water and in most cases it was not possible to simulate the real composition of the tissues with them [34]. Despite the scientific effort aimed at diversifying and extending the applications of stylized anthropomorphic phantoms, as well as in radiation protection, even in radiotherapy and medical imaging, it is still difficult to overcome their intrinsic limits of CSG. The representation of the internal organs by these mathematical

functions is rough, providing only a general description of the position and the far more complex geometry of each organ. Therefore, the stylized phantoms provide only approximate information with a high degree of error. Hence the powerful trend towards more advanced 3D modelling methods to simulate the human body more accurately.

2.2.2. Digital Phantoms

Towards the end of the 1980s, the development of more powerful computer technologies and more advanced tomographic imaging techniques paved the way for a second generation of anthropomorphic phantoms, the so-called voxel phantoms, or digital phantoms. Digital phantoms differ from stylized ones in the approach used in reproducing human anatomy [32]. These are actually "anthropomorphic" compared to those of the previous generation, which are instead mostly "geometric", because the exact anatomy can be extracted from medical images. Indeed, the turning point came when, with Computed Tomography (CT) and Magnetic Resonance Imaging (MRI), it was possible to generate high-precision images of internal organs. Thus, diagnostic imaging data were finally represented by voxel (volume element or volumetric pixel), recreating the organ volumes in 3D digital format. Therefore, these phantoms provide a discrete representation of the anatomy whose degree of approximation will be the better the smaller the size (and the greater the number) of the voxels [32, 35]. It was not easy to obtain medical images that could be suitable to develop digital phantoms, nor to handle the amount of data created by medical imaging devices. Only after a few years, it was possible to combine the various needs, thanks to the availability of much more performing computers and improved imaging devices. To date, developing digital phantoms is still not a trivial process (mainly, due to the hurdles of image segmentation) but it is certainly faster. First, raw data obtained from CT, MRI or other direct imaging methods must be available. Second, the density (or more commonly in MRI, intensity) of each component must be identified. Third, the tissues must be segmented, identified, and separated from the rest. Finally, the data must be unified into a single 3D structure that can be used for analysis. Being able to define for each voxel physical characteristics of the belonging tissue makes the digital phantoms more suitable for precise, accurate and realistic anatomical description. Therefore, voxel-based phantoms have the enormous advantage of being able to provide a faithful modelling even of complex anatomical structures (such as the brain, **Section 2.3.1** and **Section 2.3.4**).

2.2.3. Boundary Representation (B-Rep) Phantoms

The phantoms of this generation are models that contain external and internal anatomical features of the human body, obtained using the Boundary Representation (B-Rep) methods [32]. These methods use a hybrid approach, which combines the methodologies developed in the two previous generations (equation-based and image-based, respectively). The contours of an organ are represented by complex mathematical and geometric models, starting from the information extracted from the voxel data. B-Rep was one of the first vector graphics formats to represent surfaces using geometric boundaries and, to date, it is still used in solid modelling and CAD for surface representation. The design is carried out using the Non-Uniform Rational B-Spline (NURBS) representation method or by means of polygon meshes, collectively referred as B-Rep methods. Therefore, compared to voxel-based digital phantoms, B-Rep phantoms are more suitable for simulating geometric deformations and for adjustment of shapes, as a larger set of computerized operations (extrusion, chamfering, blending, etc.) is available for them. The creation of these phantoms, after the segmentation of medical images, could involve two steps: polygonal mesh modelling and NURBS modelling. First, structural imaging data are used to develop polygon mesh models of an organ's boundaries, after which other internal anatomical structures can be designed. Indeed, meshes can be generated for each segmented tissue and/or organ, before incorporating them into more complex 3D models. Mesh-based models could finally be exported as NURBS-based models by means of NURBS modelling tools. Therefore, in addition to tracing the real human anatomy, these phantoms have the outstanding advantage of being able to be transformed through 3DP into physical phantoms, starting from polygonal meshes. For 3DP, it is not mandatory to switch to NURBS-based models, unless it is necessary to deform the mesh-based model. However, as seen in **Section 1.5**, the formats accepted for 3DP are based on polygon meshes, so the final model should always be a mesh-based model.

2.2.3.1. Geometrical and Topological Description

Vector graphic are widely used in computer graphics to describe an image (vector image). It is described by means of a set of geometric primitives that define points, lines, curves, and polygons (colours and shades can also be attributed); and different from raster graphics (or bitmap graphics) in which the images are described as a grid of pixels. Three-dimensional models are instead defined according to topology, as well as geometry. The main topological elements are faces, edges and vertices; while the main geometric elements are surfaces, curves, and points. A face is a limited portion of a surface, an edge is a

limited part of a curve and a vertex is located at a point. Other elements are the shell (a series of joined faces), the loop (a circuit of edges that delimit a face), and the loop-edge links, also known as winged edges or half edges, which are used to create the edge of the loops. It is therefore a representation that connects faces, edges, and vertices. Therefore, the formats of B-Rep represent only the edges of the solid, which form a sort of stretched threads between the vertices [36]. The obtained surfaces are coated with textures to represent their final shape. A solid is thus represented as a set of connected surface elements, which are the boundary between the "solid" and "non-solid". In addition to the classic Boolean operation (union, subtraction, intersection), these formats also allow operations of extrusion, smoothing, meshing, drawing, shelling, tweaking and other combinations of these. The boundary representation has also been extended to represent special types of non-solid models, called *non-manifolds*. Normal solids in nature have a property, which, for the sake of clarity, can be described in this way: in each point on the contour, it is possible to consider a sufficiently small sphere around it, which has two parts, one inside and one outside the object. This feature makes them *manifold*, meaning solids that could actually "exist". Non-manifold models break this rule, they are a representation of non-real solids through real components, created in order to make modelling more functional and flexible. In real solids each single edge always has two (and only two) faces that join to create the solid; while, if there are edges that have only one face that joins them, these edges are defined as non-manifold (unconnected edges) and the model is an open-solid. Specifically, open solids are a sub-category of non-manifold solids, widely used in modelling complex shapes. A solid is defined as non-manifold even when there are rips and overlapping surfaces in the model. The discussion of non-manifold solids is beyond the scope of this dissertation, as it is strictly related to visual rendering needs. However, understanding how manifold models are defined and designed is fundamental for 3DP, as already discussed (in the **Section 1.5.1.1**) for the STL format. Indeed, one of the advantages of STL is the possibility of guaranteeing a "water-tight" model suitable for printing, which is not always guaranteed by more complex formats such as IGES (Initial Graphics Exchange Specification). This format provides a variety of surface representations, including higher order representations, such as B-Spline and NURBS. However, perhaps due to their greater complexity, IGES files often contain incorrect geometry (either holes, gaps or extra-edges) at the intersections of surfaces [37]. Correcting these errors, even in STL files, is not trivial. Therefore, senseless topologies should be avoided by designers at every step of 3D models' manipulation for phantoms to materialize.

2.2.3.2. Polygonal Mesh-based Phantoms

A polygon mesh is a set of vertices, edges, and faces that specify the shape of a polyhedral object in 3D space. The surfaces of a polygonal mesh-phantom are defined by a large amount of polygon meshes, commonly known as triangles. The faces are usually tessellated by triangles, which form the so-called triangular meshes, or by quadrilaterals, or by other simple convex polygons. Polygon meshes have at least three remarkable advantages in the development of anthropomorphic phantoms:

- mesh surfaces depicting human anatomy can be conveniently obtained from real patient images, or from commercial mesh models of human anatomy;
- a mesh-based phantom has considerable flexibility in adjusting and fine-tuning its geometry, effectively allowing the simulation of very complex anatomies;
- polygon meshes obtained from medical images can be saved in the STL format for 3DP.

2.2.3.3. NURBS-based Phantoms

Most commercial CAD software provide functions that can quickly convert a polygonal mesh to NURBS. This aspect is one of the classic problems of reverse engineering, which is beyond the scope of this discussion. However, it is certainly worth mentioning the NURBS-based phantoms to complete the overview of the technologies to realize anthropomorphic medical phantoms. NURBS are a class of geometric surfaces used in computer graphics to represent curves and surfaces that accurately define the shape of 3D objects. NURBS are a generalization of B-Splines and Bézier curves and surfaces, defined starting from a set of control points. The shape and volume of a NURBS surface vary with the coordinates of the control points. This is very useful in designing 4D models of the human body as a function of time. One example is NCAT phantoms used to simulate heart and respiratory movements in a very realistic modelling of the heart system [32]. However, the NURBS modelling technique also has important limitations. The main disadvantages are to be found in the intrinsic mathematical complexity and in the high number of parameters for modelling complex structures, an aspect that makes them unsuitable for the study of the smallest anatomical details of the human body. For this reason, when creating high complexity structures, instead of NURBS, it is more convenient to use models in polygonal mesh format.

2.3. Brain Phantoms

Brain phantoms aim to mimic the physical and physiological properties of various brain tissues. They are important for the development and testing of various medical imaging modalities including CT, MRI, Positron Emission Tomography (PET), Single Photon Emission Tomography (SPECT) and others. Ever since it was possible to acquire images of the inside of the human body, there has been an ever-increasing interest in the interactions of electromagnetic waves with biological tissues for medical imaging research. Hence, the need to create "biological", and then "anthropomorphic", phantoms that could mimic the electromagnetic properties of tissues. Creating a model that reproduces the shape of each brain compartment is not trivial, especially because of its deep structures (gyri and sulci). Generally, brain phantoms that attempt to emulate the external anatomy of the brain have a reduced depth of the grooves or only recreate the superficial shape of the brain, obtaining it with various types of moulds. Even when these phantoms reproduce the physical appearance of the human brain, they fail to accurately represent the physiology and variety of brain tissues. In addition, multimodal imaging of these phantoms is usually not easy. This may be due to various problems, which vary from case to case, but which are often attributable to the need to have structures that are smaller than the resolution of the imaging method or insufficient contrast (for example, between the uptake of the marker in the structure of interest compared to the surrounding ones).

2.3.1. Brain Anatomy

The human brain is a functionally and topologically complex organ, richly innervated, with deep sulci and convolutions on its surfaces (medial and lateral), as well as fluid that fills the ventricles, which are also complex in shape. The human Central Nervous System (CNS) is derived from four basic embryological formations: the prosencephalon (adult forebrain), the mesencephalon (adult midbrain), the rhombencephalon (adult hindbrain), and the elongated spinal cord. Embryonic divisions give rise to adult brain with the associated ventricular spaces filled with cerebrospinal fluid (CSF). The prosencephalon (forward brain) soon divides into the two parts of the adult forebrain: the telencephalon (or cerebrum, outer brain), giving rise the cerebral hemispheres; and the diencephalon (through brain), becoming the thalamus and hypothalamus. The mesencephalon does not further divide and becomes the midbrain of the adult. The rhombencephalon further divides into the metencephalon and the myelencephalon, which become the pons and cerebellum, and medulla, respectively (**Figure 6**).

Figure 6 – Brain lobes and major brain structures. *The lobes are the 4 major subdivisions into which the cerebral cortex is divided in each hemisphere. The frontal lobe is located at the front of each hemisphere, opposite the parietal and temporal lobes, and is the largest of the four lobes. The parietal lobe is positioned over the occipital and temporal lobes, beyond the frontal lobe and the central sulcus. The occipital lobe constitutes the posterior end of the telencephalic hemispheres and has no limits whatsoever with the temporal lobe, which is in turn located below the frontal and parietal lobes from which it is separated by the lateral (Sylvian) fissure. The figure also shows the main structures of the telencephalon (cerebrum), of the diencephalon (thalamus and hypothalamus), of the brainstem (midbrain, pons, medulla) and of the cerebellum.*

The cerebrum is the largest part of the brain. It contains the cerebral cortex of the two hemispheres, as well as several subcortical structures (hippocampus, basal ganglia, and olfactory bulb). The right and left cerebral hemispheres are separated by a deep median longitudinal fissure, while each hemisphere is in turn divided by other sulci that delimit four lobes (frontal, parietal, occipital and temporal). The major components of the CNS are the grey matter (GM) and the white matter (WM) [38]. GM consists of numerous neuronal cell bodies and relatively few myelinated axons. In the brain and in the cerebellum the neuronal bodies are mainly arranged on the surface, forming the cerebral and the cerebellar cortex, respectively. WM is composed of bundles, mainly made up of myelinated axons (tracts), which connect various GM areas of the brain to each other, carrying nerve impulses between neurons. Indeed, myelin acts as an insulator, which allows brain electrical signals to jump (saltatory conductions) along the axons. WM forms also the bulk of the deep parts of the brain and the superficial parts of the spinal cord, where the neuronal bodies are located centrally. Therefore, the WM is found buried in the inner layer of the cortex, while GM is mainly located on the surface of the brain. In the spinal cord, GM and WM arrangement is reversed: GM is deep inside its butterfly-shaped core and the insulating WM is wrapped around the outside (**Figure 7**).
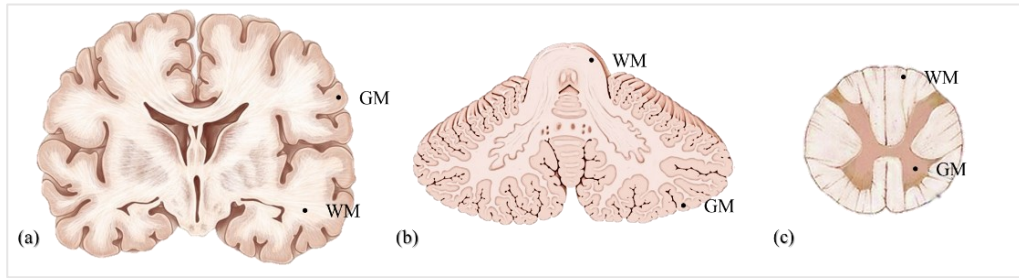
Figure 7 – Gray matter (GM) and white matter (WM) in the cerebrum, cerebellum, and spinal cord. (a) Frontal section of cerebrum: GM is mainly located on the cortex, while WM is found buried in the inner layer of the cortex. (b) Transverse section of cerebellum: in the cerebellar cortex there is a very tightly layer of GM, underneath lies WM. (c) Transverse section of spinal cord: GM in the spinal cord is known as grey column presented in an "H" or butterfly shape, while WM forms the superficial part of the spinal cord.

In addition to the surface and the spinal cord, aggregates of GM, surrounded by deep cerebellar WM (arbor vitae), are also distributed in the depths of the cerebrum (hypothalamus, thalamus, subthalamus, basal ganglia – putamen, caudate nucleus, globus pallidus, nucleus accumbens, septal nuclei), cerebellar (deep cerebellar nuclei – dentate nucleus, globose nucleus, emboliform nucleus, fastigial nucleus) and brainstem (substantia nigra, red nucleus, olivary nuclei, cranial nerve nuclei) [39] (**Figure 8**).
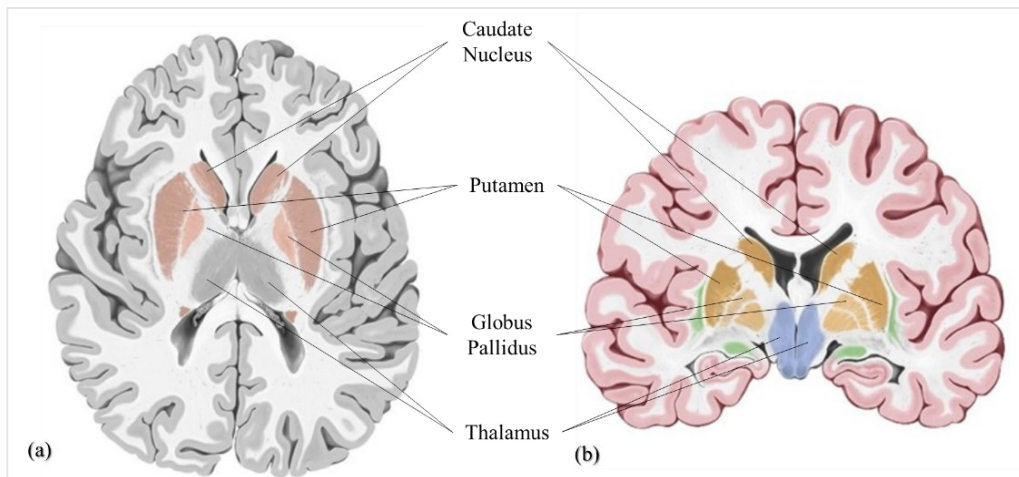
Figure 8 - Basal ganglia and thalamus. (a) transversal section and (b) frontal section of the cerebrum in which some basal ganglia (caudate nucleus, putamen and globus pallidus) and the thalamus are coloured and indicated by arrows.

2.3.2. Brain Imaging

While both CT and MRI, in their basic implementation, return a structural and non-functional image of the brain [40], nuclear medicine techniques based on

Emission Computed Tomography (ECT), which includes both PET and SPECT, provide functional images [41]. Therefore, in CT and MRI, what is displayed at the site of a lesion refers only to the alteration of the macroscopic structure of the brain, without any reference to any functional alterations that the lesion may cause. On the other hand, the most common functional methods are based on the principle according to which the metabolism of a region of the brain, and therefore the amount of blood that bedews it, depends at least partly on the activity carried out at that time by that tissue. Therefore, the greater the functional activity of a brain tissue, the greater its metabolism and consequently the blood supply to that tissue, and these characteristics vary over time. Nowadays, the more detailed structural information provided by CT and MRI techniques can be integrated with functional information obtained from the measurement of Cerebral Blood Flow (CBF) and cerebral metabolism by ECT [42]. The result is images where the information is hybrid, that is, it has both a structural and functional meaning. The CBF measurement is carried out by monitoring the arrival of a radioactive isotope (for example, Xenon 133 or metastable Technetium 99) through the cerebral blood circulation in the brain, measuring its distribution. In this way, it is possible to evaluate the variations in concentration of the tracer over time and consequently its distribution at the level of the different brain regions. The method is invasive and therefore should be limited to patients who for medical-diagnostic reasons require tests of this type. However, it has the merit of having highlighted, through the correlations with morphological images, that the areas of impaired perfusion are often larger than a structural lesion. With this method it was also possible to measure, for the first time *in vivo*, increases in perfusion in specific brain areas related to specific tasks (for example, the increase in blood flow in the occipital visual cortex in the presence of light stimuli). However, ECT methods have a much lower spatial resolution than CT and MRI techniques, the reason why hybrid methods are used and developed to obtain information that can increase structural and morphological details, while preserving functional information. Current CT scanners have a spatial resolution of 0.5 – 0.625 mm in the z-axis, and approximately 0.3 – 0.5 mm in the x- to y-axes. The z-axis resolution of CT is superior to the resolution of MRI, which is typically 1 – 2 mm for most clinical sequences [43]. The spatial resolution in PET depends on several factors ranging from physics limitations related to the positron emission and annihilation (i.e., positron range and noncollinearity) to those dependent on the detection system (e.g., crystal size, photon detector, and scanner diameter) or the image reconstruction algorithm [44, 45]. In most PET studies, glucose metabolism is studied, which is the main source of energy for nerve cells. Therefore, a glucose analogue substance is used, fluorodeoxyglucose (FDG). The fluorine isotope present in this molecule is fluorine-18 (^{18}F), which is a radioisotope that emits

positrons, which are detectable by PET. The greater the metabolic activity of a given brain area, the greater the consumption of glucose and the amount of incorporated ^{18}F-FDG and therefore the greater the amount of γ radiation emitted by that specific area. When decaying, the radioactive isotope emits positrons which, interacting with electrons, emit two γ rays by annihilation which can be recorded by specific sensors. After that, a computer reconstructs maps of the distribution of metabolic activity within the brain based on the distribution of γ rays. Furthermore, with this technique, it is also possible to map the distribution of highly specific moieties, such as neuroreceptors or molecules involved in neurodegenerative processes (e.g., amyloid, involved in Alzheimer's disease pathogenesis, or Tau, whose accumulation in the brain is involved in the so-called "tauopathies"). Through PET, therefore, it is possible to define abnormal, hypofunctional brain areas, which can in turn be localized on anatomical (MRI or CT) data. Many PET studies show, once again, that the area of reduced metabolism is usually larger than the area of structural lesion highlighted by morphological imaging.

2.3.3.   Applications of Brain Phantoms

Anthropomorphic phantoms can be used for assessment of inaccuracies in medical imaging systems. Phantom imaging studies are crucial to reduce quantitative variability due to differences in the acquisition setting and intrinsic imaging characteristics. In addition, phantom studies can be used to verify that each scanner is appropriately calibrated and that it has adequate capabilities to support brain imaging. Commonly, the phantoms (mostly geometric) are positioned in the centre of the field of view of the scanning system in a standard orientation in order to simulate the patient's supine position during brain imaging. Obviously, there is an intuitive and real disparity between the images usually obtained with simple geometric phantoms and the distributions of intensities and/or activities seen in *in vivo* images. This disparity can be circumvented thanks to more realistic anthropomorphic phantoms, which allow for much more precise and accurate information to be obtained, because it is processed with respect to a more faithful reproduction of the anatomy. Many studies have validated the use of phantoms also to examine the requirements required by tumour imaging. In this context, brain phantoms are used for the assessment of quantitative accuracy in the measurement of absorption at hot spots, which simulate tumour sites. Therefore, for brain tumours the use of realistic anthropomorphic phantoms can be useful to ensure that all scanners provide acceptable images for the study, and for nuclear medicine that the scatter and attenuation correction methods work as expected. In the following, some examples of brain phantoms application will be illustrated. Since most brain

phantoms are used for nuclear medicine imaging, applications are mainly found in this field.

2.3.3.1.   Inaccuracies in Nuclear Medicine Studies

Although a phantom can never precisely simulate imaging problems on real patients, having an anatomical model of it can add a level of complexity to test nuclear medicine systems in a more intuitive and satisfying way. ECT imaging methods, in particular PET/SPECT, allow detecting quantitative or semi-quantitative *in vivo* measurements of physiological and metabolic quantities in humans. The brain phantoms are mainly designed to carry out the accuracy measurements of the ECT systems. The following are the main sources of inaccuracy in nuclear medicine [45, 46], particularly PET, which can be evaluated with phantom-based measures.

Registration error. The co-registration of functional information obtained with ECT, with high-resolution structural information, such as those obtained in MRI images, has many clinical and research applications. Whenever a patient undergoes a multimodal multilayer study, the images obtained from the different modalities should represent exactly the same anatomy in each point for an optimal comparison of structural and functional data. Indeed, different sets of images acquired on the same subject, using the same or different modality, can differ in scale, resolution (voxel size), orientation (angle) and position. For some organs even the shape can change in relation to the patient's position, but it is a problem that does not occur in acquiring images of the brain, in which case the shape can be assumed constant. Only anatomical features can be used to align image sets. The use of anatomical features can be separated into techniques in which an expert identifies the location of features common to the two sets of images, and techniques in which the surfaces of the organs are determined from the images of the two sets and matched through a co-registration program that transforms the source image by superimposing it on the reference image. This is the image that is assumed to remain stationary (sometimes known as the target or template image), while the source image is moved to match it. Inevitably, following these procedures, there will be a registration error, which can be defined as the difference in the position of an anatomical point of the reference image compared to its position in the source image (co-registered with the first). Brain phantoms, such as *Hoffman 3D Brain Phantom* (see **Section 2.3.5.1**), are used to measure this registration error in different contexts and to estimate the contribution to this error resulting from errors in other transformation parameters (for example, independently measure inconsistencies in rotation, translation, and rescaling parameters).

Limited spatial resolution. Poor spatial resolution is a major source of inaccuracy in ECT. It is limited both by intrinsic factors, dependent on the physics of the exploited phenomenon (the annihilation of positrons), and technological factors, dependent on the limitations of the equipment. In PET, the positron, once emitted, travels a certain distance before annihilating, which is greater the higher its energy is. This inevitably leads to a degradation of the spatial resolution of the images (called the range effect). For the ^{18}F in water this error is approximately equal to 2 mm. Another error factor is the angular deviation of the photon pairs. In fact, the emission is never perfectly antiparallel (with a precise angle of 180°) but tends to have a margin of error (which in water is approximately 0.5°). These intrinsic factors lead to a loss of spatial resolution that increases as the distance between the detectors and the emission source increases (about 2.2 mm for each meter). Among the technological factors, the finite size of the elements of the block detector contributes to determining the resolution of the instrument, as well as the thickness of the scintillation crystals, which can lead to interactions at different depths in the crystal, with consequent error in determining the position of the event in the block detector. It is called parallax error and, sometimes, limited by dividing the scintillator crystal into 2 layers. There is also the coding error, due to an imperfect localization of the position of an event within the block detector due only to technological limitations of the detection system.

Partial volume effect. In nuclear medicine, it is often necessary to obtain quantitative values that indicate how much radiopharmaceutical has accumulated in the tissues. As a rule, the number of counts detected by the tomograph is directly proportional to the activity present in the tissue, but this statement is no longer valid if we consider elements smaller than 2 times the minimum spatial resolution of the instrument. The error due to this phenomenon is called the partial volume effect and leads to a loss of counts proportional to the size of the target studied (which visually translates into a loss of contrast between small elements). For values ranging from 1 to 2 times the minimum resolution of the instrument it is possible to correct at least partially the counts for this error using experimentally measured curves (recovery curves). This correction is always necessary to obtain reliable quantitative data from the images. Specifically, this is necessary because the human body tends to absorb the photons emitted, especially if the point of emission is located very inside the body, leading to a drastic drop in counts that increases with the depth and density of the matter crossed. Usually, the correction is carried out exploiting CT scans, which are photon attenuation maps, with the advantage of also providing relevant clinical information, as well as helping in the localization of radiopharmaceutical accumulations using hybrid PET/CT imaging. CT provides

much less noisy images and much faster but using photons with a much lower energy than those generated by annihilation phenomena. Since the difference in attenuation between different energies of γ photons is not linear, different conversion coefficients are used for different ranges of Hounsfield units detected by the CT. This correction generally works but can give erroneous results in the presence of materials with a high atomic number (metal objects, such as prostheses), leading to artifacts in the image that cannot be corrected (and which must be interpreted as such by the nuclear doctor, perhaps using incorrect attenuation images as an aid). MRI images can also be used for the same purpose, but, since MRI intensity is never a function of tissue radiopacity, it is necessary in such cases to use mathematical models to estimate attenuation maps.

Noise on images. In the measurement path, when an event is involved in a coincidence, the signal from each photomultiplier is measured and digitized. This procedure takes some time. During this interval, the detector is in a state of so-called "dead time" during which the same detector cannot accept other events. This fact causes the loss of a certain fraction of the events which must be suitably corrected (correction for dead time). This effect also determines a limitation on the maximum rate measurable by the PET system (and therefore on the maximum usable activity). In modern PET systems, however, this limitation should be secondary to the effects due to accidental coincidences. The "true" counts detected by the machine are those that correspond to a real annihilation event, however it is also possible to detect "false" counts due to events in which at least one of the two photons has been deflected due to a Compton interaction with the matter crossed (scattered event); or due to two different events that led their photons to interact "by chance" within the time window at the limits of the detector (random events). While true and scattered events are due to annihilation events (therefore called prompt events) this is not so for random events. The amount of prompt events varies linearly with the activity given to the patient, while the rate of true events on scattered does not. Scattered events lead to a degradation of the spatial resolution of the image. A measure, albeit indirect, of the quality of the acquired data in relation to the presence of scattered and random events and the effect of the dead time on the measured data is given by a value called Noise Equivalent Count (NEC) rate, which indicates the true events on the total for different activity values in the image. In practice, this parameter measures the system's ability to select and capture true events. Using this (standardized) procedure it is possible to obtain a curve (NEC curve) that shows the quality of the acquisition for different ranges of activity. On this curve, the most suitable activity to use with the tomograph corresponds to the peak.

2.3.4. Digital Brain Phantoms

Digital brain phantoms are generally derived from brain MRI images of a normal volunteer's scan and are widely used to simulate neuroimaging procedures. They are distinguished from physical phantoms because they are an image representation (voxel-based representation) of phantoms that physically do not (or do not yet) exist. Main brain structures are typically segmented automatically, and edited manually where needed by experts, resulting on maps of binary or probabilistic labels associated with each voxel of a given structure. Digital phantoms can be used after the implementation of new medical image processing algorithms because they allow it to be validated to ensure that the procedure meets all the requirements set out in its initial design phase. Indeed, a robust evaluation of the accuracy of the segmentation algorithms requires a "gold standard", where an exact classification of each voxel is given *a priori* by a realistic phantom.

2.3.4.1. Phantomag

As anticipated, digital phantoms are needed to evaluate the performance of segmentation methods, providing a "gold standard" against which the automatic segmentation of software can be compared. *Phantomag* is a digital MRI phantom of a normal brain, which simulates the relaxation parameters distributions of real reference studies (**Figure 9**).
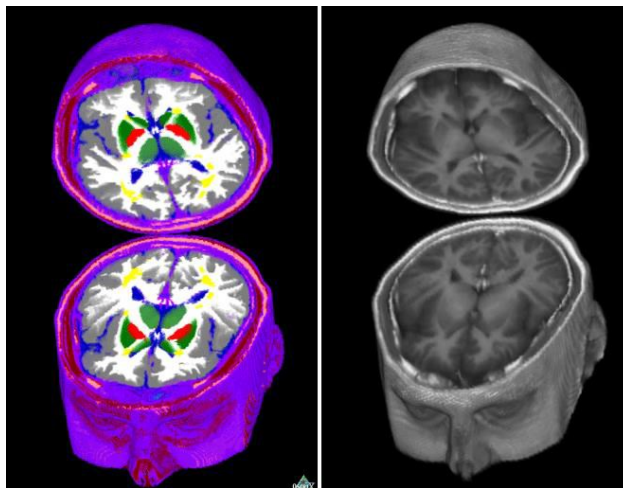
Figure 9 – Phantomag. It is a digital brain phantom created for validation of segmentation methods. It simulates spin-echo and fast field-echo sequences of any realistic relaxation time of different brain tissues, providing four brain model (two normal subjects and two multiple sclerosis patients) [35].

The phantom is composed of 17 compartments of segmented healthy brain tissue, plus an optional eighteenth compartment that simulates multiple sclerosis

(abnormal white matter) lesions. Relaxation parameter maps of R1 = 1/T1 (longitudinal relaxation time or lattice-spin relaxation), R2 = 1/T2 (transverse relaxation time or spin-spin relaxation) and proton density (PD) of a normal brain were derived from an acquisition on a 1.5T scanner of a 38 years old male normal volunteer, through Conventional Spin-Echo (CSE) sequences (the mainstay of the early MRI studies, see **Section 5.2.2**). Spin-echo data was used to calculate quantitative maps of relaxation parameters (R1, R2, PD). These quantitative maps enable the formation of consistent images without imperfections due to the variation of the gain of the scanner at different times and on different subjects (further details in the **Section 5.2.2.3**). The phantom MRI data consists of 150 axial slices, with a near-isotropic voxel of $0.9375 \times 0.9375 \times 1$ mm^3. For each slice, the corresponding PD and relaxations rate maps, calculated voxel-wise from CSE PD-, T1- and T2-weighted (PDw, T1w, T2w) images using a mono-exponential two-point method, are provided with the phantom, along with the corresponding brain tissue maps, segmented by means of a fully automated multi-parametric segmentation method, and manually refined by expert neuro-radiologists to have a binary classification of each brain voxel (i.e., only one tissue fills each voxel). The segmented tissues are GM, WM, and CSF, along with subcortical GM structures. In addition, also the air, the intra-cranial connective tissue, and the extra-cranial tissues (fat, muscle, vitreous humour, nasal mucosa, extra-cranial fluid, skull, and other low PD tissues) are defined [35].
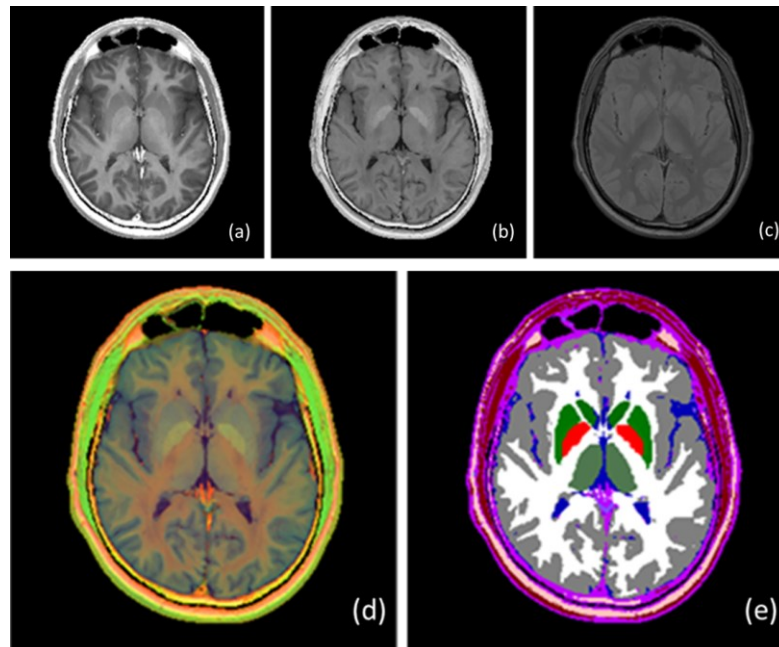
Figure 10 – Normal volunteer study of Phantomag. *(a) Longitudinal relaxation rate (R1) map. (b) Transversal relaxation rate (R2) map. (c) Proton density (PD) map. (d) Quantitative Magnetic Color Imaging (QMCI) representation. (e) Binary classification of brain tissues.*

Relaxation maps offer an additional advantage, which is the possibility of providing integrated information from multiple relaxation parameters exploiting a full-colour representation approach (**Figure 10**). Therefore, the digital phantom also provides a *Quantitative Magnetic Color Imaging* (QMCI) representation, coding the three quantitative images into single colour images where the R1, R2, and PD values, are red, green, and blue intensities, respectively (the QMCI is described in **Section 5.2.2.3**).

2.3.5.   Physical Brain Phantoms

Physical brain phantoms have different purposes, complementary to those for which the digital ones are used. Their production implies the fabrication of controlled shapes with known volumes, in materials with predictable properties in MRI and represent an objective measure to validate the performance of image processing algorithms, especially segmentation ones. In order to evaluate the accuracy and precision of the segmentation methods, different characteristics of the physical phantoms must be present. They must have known volume and natural size, produce contrast similar to that seen in vivo, and be anatomically accurate in shape and proportions. These phantoms, once filled with radioactive tracer solutions (for use in ECT), or with water-based solutions dopes with different metals (to provide brain-like densities at CT or signal intensities at MRI), allow analysing quantitative aspects of the imaging systems under physical conditions overlapping those in which the patient is scanned. Unfortunately, the creation, preparation and analysis of the physical phantoms is not trivial. Making a physical model, faithful to the real anatomy of the human brain and, ideally, fillable with suitable solutions, requires a considerable design effort, whatever the technique to build it. Furthermore, because of the geometrical complexity of brain tissue compartments, the removal of air bubbles during the filling phase, which would create areas of hypo-intensity in imaging, represents and additional challenge to this approach. The air removal is necessary to avoid non-uniformity in the concentration of radiotracer resulting from improper mixing of the ^{18}F-FDG solution due to air bubbles. For these reasons, new techniques for the development of anthropomorphic physical brain phantoms are continuously being researched, and no optimal solution has emerged to date.

2.3.5.1.   Hoffman 3D Brain Phantom

The *Hoffman 3D Brain Phantom* was designed for accuracy evaluations in PET in 1983. The idea arose because in this context it is necessary to take into account an intuitive and real gap that exists between the images usually obtained with

simple geometric phantoms for tests and the distribution of activity that is instead observed in *in vivo* images. In the brain the activity distribution of metabolic or flow measurements is irregular and three-dimensional with out-of-plane activity distributions quite different from those in the plane. When functional investigations of the brain with PET technology are performed, the image obtained shows the study of a distribution of FDG or brain flow with a GM to WM ratio of about 4 or 5 to 1 [47, 48]. The first version of this phantom consisted of a single chamber cut in PMMA (polymethylmethacrylate, better known as Plexiglas). However, this phantom was useful for evaluating the performance of PET systems only in a non-quantitative way. So later, in 1990, the concept was extended to a three-dimensional phantom, still used today, which is useful in simulating several problems present in brain imaging with PET systems (**Figure 11**).
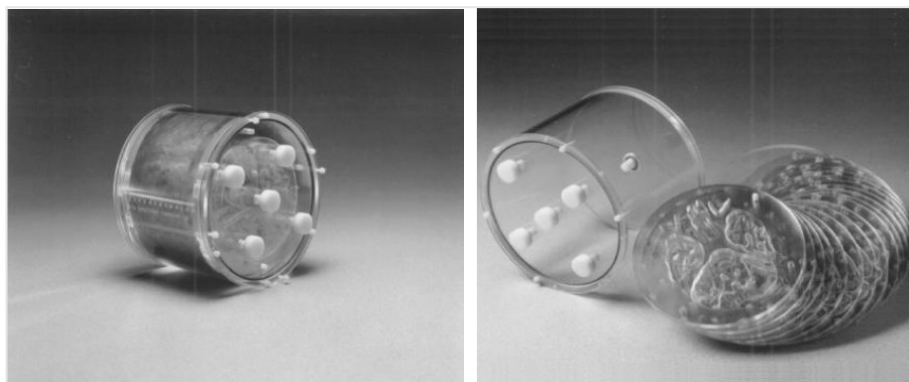
*Figure 11 - **Hoffman 3D Brain Phantom**. It provides an accurate anatomical simulation of radioactivity distribution from brain PET and SPECT studies, and of proton density distribution and relaxation parameters for brain MRI studies.*

The core dataset for the phantom was derived from a set of 19 T1w spin-echo MRI scans taken at 7 mm intervals over the entire brain. From these, with the aid of software tools, anatomical atlases and neuroanatomy experts, the external contours of the brain, the interface between all the GM and WM structures and all the ventricular regions (containing CSF) were derived. After that, each ROI (Region of Interest) identified, corresponding to a list of coordinates in the image matrix, was filtered and interpolated to obtain plots of these contours. A typical set of these plots is shown in **Figure 12**, which also helps to better understand how this phantom is made. The shaded areas contain the plastic and all areas within the outermost contours of the cortex (except the ventricles) are open and filled with isotopes once the phantom is assembled. The ventricles act as spacers between the thick layers. Thus, the phantom structure consists of two types of cut-out plastic layers. A first type of layer is a plastic cut-out of the WM and the outermost boundaries of the brain. The area corresponding to the GM is open

and can be filled with activity when the phantom is used. The other type of layer is a cut-out of only the ventricles and the outermost borders of the brain. The fluid-filled space around the ventricles provides activity for the WM. These two types of layers are positioned alternately to make up the whole phantom. A radioisotope is added and after the air bubbles have escaped the phantom is ready for use. The phantom is filled with agents appropriate for each study: a solution of $CuSO_4$ is inserted for the MRI, a solution of ^{99m}Tc for the SPECT and a solution of ^{18}F-FDG for the PET. Note that this phantom can accurately reproduce a GM to WM tracer concentration ratio of 4 to 1, which is considered representative of the physiological range [48].
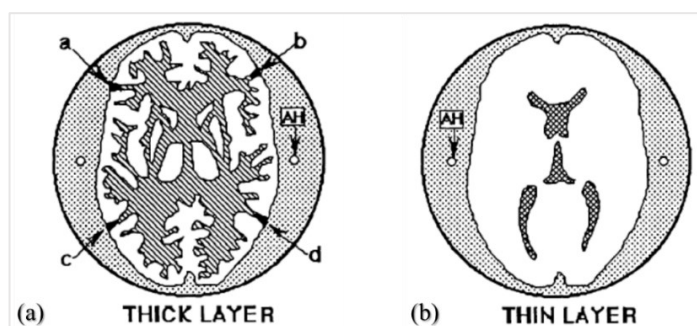
Figure 12 – Plot of the contours of Hoffman's phantom. (a) shows plot of the outer lines of the WM structures and the outer contours of the cortex which is cut out of the plastic to form one of the layers in the brain phantom. Shaded areas contain plastic. The areas corresponding to the structures of the GM are open and, once the phantom is assembled, filled. (b) shows the plot of the external lines of the ventricles and the external contours of the cortex. These are cut out in the plastic to create one of the layers in the brain phantom [47].

2.3.5.2.   RSD Striatal Phantom

Radiology Support Device (RSD) Inc. is a world leader in the production of anthropomorphic phantoms for radiography and radiotherapy. It was founded by Samuel W. Alderson, widely recognized as one of the pioneers of Phantom Technology. The head phantom (also known as Alderson's phantom) is based on an RSD standard with a cut in the skull area to allow easy insertion or removal of the brain "shell". The nasal cavities and maxillary sinuses are filled with a foam. The brain shell contains 5 compartments that can be filled separately: left and right putamen, left and right caudate and the rest of the brain. This allows different caudate to putamen ratios as well as different striatal to background ratios to be obtained; this also permits differences between left and right striatal activity to be examined. The volume of the shell is approximately 1260 ml. The volumes of the caudate and putamen nucleus are 5.4 ml and 6.0 ml, respectively. A set of refillable capsules is provided with the phantom, which act as external markers. The capsules can be filled with a radioactive solution and fixed to the

external surface of the phantom. The phantom can then be imaged by SPECT or PET to compare image-registration techniques. The quantification of the uptake of the striatum is not simple because it depends on a series of factors:

- type of radionuclide used;
- imaging factors, such as: collimator type, amount of dispersion and attenuation;
- image processing parameters, such as: scatter, attenuation correction techniques, the type of reconstruction filter, slice thickness, the size of the ROI and its position.

In normal subjects, the putamen and the head of the caudate nucleus are small structures with typical dimensions of 7-15 mm in the axial plane (which is comparable to the resolution of the acquisition system). Since partial volume effects are more important for objects less than twice the size of the system resolution, the selection of imaging and reconstruction parameters is critically important in calculating the striatal to occipital ratio (used to measure relative striatal uptake in the brain).

2.3.5.3.   STEPBrain Phantom

The *STEPBrain* brain phantom was created and patented in 2006 by researchers from the *Italian National Research Council - Institute of Biostructures and Bioimaging* of Naples [49]. It is a physical brain phantom that can be used in CT, MRI, PET and SPECT. This anthropomorphic phantom has different characteristics compared to other phantoms found in the literature or to those commercially available. Indeed, it was designed as composed of two separate compartments for GM and WM, which can be filled with solutions with different concentrations of radioactive isotopes for PET/SPECT imaging, para-/ferromagnetic metals for MRI, and iodine for CT. The physical model was constructed using a rapid prototyping stereolithographic technique applied to a digital model derived from a 1.5T MRI image dataset of a 35-year-old normal volunteer, consisting of 150 partially overlapping 3 mm thick slices (1 mm of increase) to cover the whole brain. T1w, PDw and T2w spin-echo images were obtained for each slice, then segmented into GW, WM and CSF using a multi-parametric technique. The segmented images were then further processed using home-made and industrial software to fill the vessels located in the parenchyma and eliminate the "voxel islands" inside a tissue not connected in 3D to other voxels of the same tissue. In addition, the basal ganglia were manually edited to ensure their connection to the GM for filling. The surfaces of the segmented brain tissues were then converted into a vector representation by commercial software and the cavities for the GM and WM compartment were obtained

defining a thickness of 1.5 mm. Finally, tubes were added to the model for filling the GM and WM compartments.

The 3D model was then materialized with a first generation stereolithography machine. The printed phantom was not watertight, and the two compartments were in communication. Therefore, an artisanal waterproofing process using sealing wax and liquid latex was used to close the spaces between the layers. The result was thickened walls, but also watertightness of the phantom compartments. The GM and WM of the phantom are refillable with different isotope concentrations for PET/SPECT scanning, so that the normal 4 to 1 ratio of GM to WM in FDG concentration can be simulated. Furthermore, the different relaxometric properties of GM and WM can be simulated with different concentrations of paramagnetic ions.
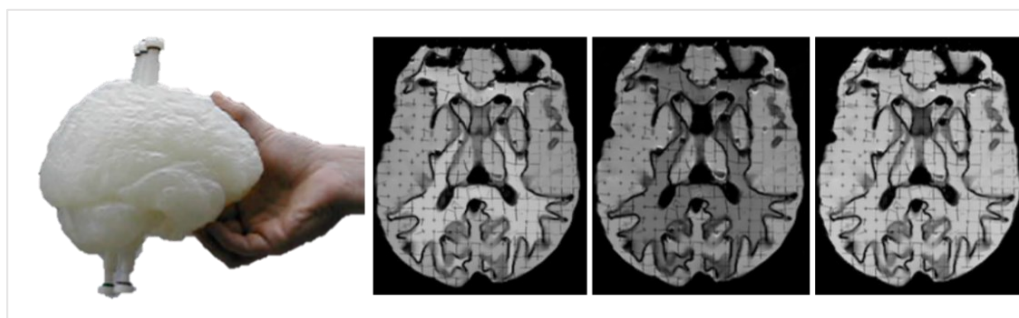
*Figure 13 – **STEPBrain Phantom**. The figure shows (from left to right) the physical phantom, a selected T1-weighted, T2-weighted an PD-weighted MRI image of the brain phantom. In this figure it is evident how this brain phantom can simulate the different contrasts of MRI, but there are also numerous air bubbles due to a non-optimized filling process, as well as the reticulate of supporting elements.*

Compared to *Hoffman 3D Brain Phantom*, which is certainly the most widespread to date, the *STEPBrain* phantom has several potential advantages. It is made up of two independent compartments, while the *Hoffman 3D Brain Phantom* has only one compartment. In the *Hoffman 3D Brain Phantom*, the area corresponding to the GM is empty, while the WM area is 3/4 in plastic to simulate a concentration of activity in the WM that is 1/4 of that of the GM. Since in *STEPBrain* the GM and WM compartments are separate and independent, it is possible to simulate any concentration ratio of the isotope.

Chapter 3

3D Modelling of the New Brain Phantom

3.1. Introduction

The anthropomorphic brain phantom designed and built during the doctoral work is proposed as an evolution of the patented *STEPBrain* phantom (described in **Section 2.3.5.3**). The goal was to build a new anthropomorphic brain phantom even more complex than the previous one, with improved shapes (better representation of the brain sulci), while exploring the possibility of creating a greater number of compartments, thus trying to implement a new 3D modelling pipeline, integrating the potential of segmentation and medical image-to-STL software, finally trying to materialize it through a modern 3DP technology. For this reason, in a first step, we aimed at demonstrating the *proof-of-concept*, defining a design workflow to obtain the 3D model of phantom, and subsequently refine the modelling technique starting from the definition of a new segmentation method. In this chapter, the new phantom, and the design pipeline for obtaining a printable 3D model will be presented. The physical phantom will be illustrated here as the counterpart to the *Phantomag* digital phantom, which already provides exact segmentation of brain tissues. The same pipeline will then be directly applicable to segmented brain MRI images with the new method (discussed in **Chapter 5**) for personalized brain phantom. The new brain phantom design workflow is schematically summarized in the **Appendix**, **Flowchart (B)**.

3.2. The New Brain Phantom

The new anthropomorphic brain phantom consists of three separate compartments for simulating the activity of three brain tissues. The simulated compartments are that of GM and WM (as in **Section 2.3.5.3**), plus an important new element: the striatum compartment, which generally shows a high uptake in studies of nuclear medicine [50]. The striatum is a set of brain nuclei, formations of deep GM, immersed in the WM, located at the base of the cerebral hemispheres. Precisely, the neostriatum is a component of corpus striatum, formed by the caudate nucleus and the lenticular nucleus, in turn divided into

putamen and globus pallidus, also commonly referred to simply as pallidus or paleostriatum, while the caudate nucleus and the putamen together constitute the striatum.

The walls of the three (hollow) compartments of the new brain phantom should ideally have a sub-millimetre thickness, preferably in the range between 0.4 – 1 mm. The latter was chosen considering the resolution of the imaging methods, and the definition of minimum printable vertical wall thickness (**Section 1.5.2.2**). The walls of the physical phantom should not be visible to imaging, therefore with a thickness of less than one millimetre, also ensuring strength, stability, and durability of the final part. At the same time, the walls of the phantom should be watertight, so to avoid any leakage to the outside, or between the compartments, for a good simulation by means of different solutions for different brain imaging modalities. The filling system must be as simple and automatable as possible, to minimize the risk of contamination of the solutions per compartment and exposure of operators to radiations, when radioactive solutions are used for ECT studies. Furthermore, the filling technique should be such that air bubbles do not get trapped in the phantom (see **Section 4.5**).
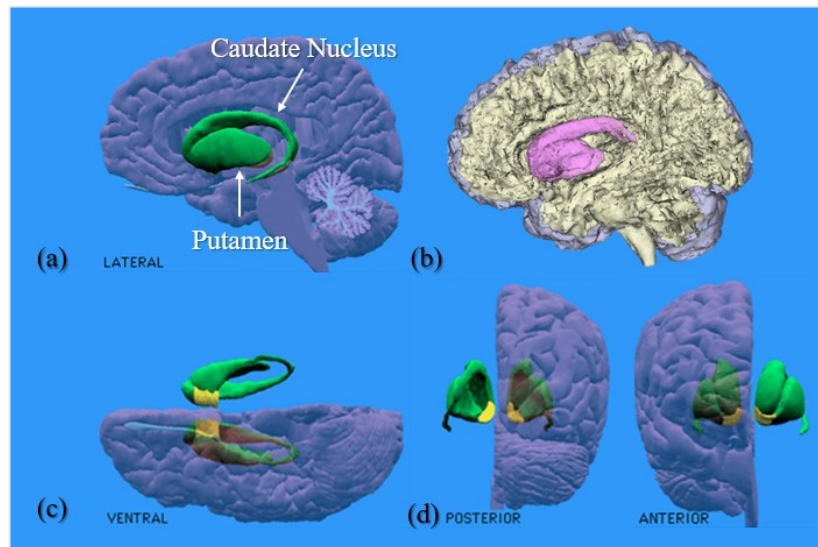
Figure 14 - Anatomy of the striatum. *In the figure, the structure of the striatum compartment that we are going to recreate in the brain phantom. In (a), (c) and (d) the lateral, ventral, posterior and anterior views of the Caudate Nucleus and Putamen can be observed, respectively. (b) shows a lateral view of the created 3D model of phantom. As can be seen, the caudate nucleus is curved, forming a sagittal "ram's horn" that surrounds the upper margin of the thalamus, while the putamen is the outer portion of the lenticular nucleus.*

3.3. Brain Phantom Design Workflow

An anthropomorphic brain phantom can be extracted from brain MRI images of a normal brain. Therefore, acquisition of a brain from a normal volunteer is necessary. In MRI, different types of sequences lead to images that highlight different characteristics of the tissues. The different sequences set up configurations (obtainable through magnetic resonance equipment), which concern the series of radiofrequency pulses and field gradients that allow generating specific resonance images, frequently used in the clinical setting (further details are in **Section 5.2.2**). In the design workflow, the acquisition step defines the maximum resolution obtainable for the 3D model, because it is linked to the resolution of the images, and consequently to the smallest materializable detail for the anatomy of interest. However, the most critical step in the workflow for designing a printable brain phantom remains tissue segmentation. Once accurate segmentation is achieved, the designer should take care of extracting, manipulating, and refining an error-free STL model, ready for printing.

3.3.1.   Image Segmentation

In the literature, many methods of brain segmentation of different accuracy and degree of complexity are reported. Besides manual ones, there are semi-automatic and automatic methods. Automated methods are by far preferable for operator bias-free segmentation, even if in the absence of "ground-truth" the results of the automatic segmentation methods must be compared with the manual segmentation of neuroradiologists for validation [51]. Therefore, automated segmentation of brain images from MRI is still a challenging task due to image artifacts (such as intensity inhomogeneity, also known as bias field, and partial volume effects), and because different anatomical structures can share the same tissue contrast. Although the ability to accurately segment a brain image is part of the more general design pipeline of an anthropomorphic brain phantom, the complexity of this step deserves further discussion. Having a generalizable method for segmenting MRI images from different clinical sequences to achieve accurate segmentation useful for 3DP is certainly an open challenge. A new multiparametric segmentation approach basically based on label propagation will be presented in **Chapter 5**. In the context of 3DP, software that can be used for these purposes, once integrated into the software that allow the extraction of 3D models from medical images, would pave the way for the personalization of phantoms. However, in this section, pursuing the aim of obtaining the *proof-of-concept* for the new brain phantom, knowing that segmentations of a healthy brain (already validated by neuroradiologists) are available in digital phantoms, we intend to define the design workflow of the 3D model of a physical

counterpart of the digital brain phantom. Therefore, the modelling was carried out starting from the classification contained in the digital phantom *Phantomag* (described in the **Section 2.3.4.1**). The phantom provides an accurate description of the tissues of interest for modelling, providing in addition to the segmentation of GM and WM also that of the cerebral nuclei of interest for modelling the striatum [35].
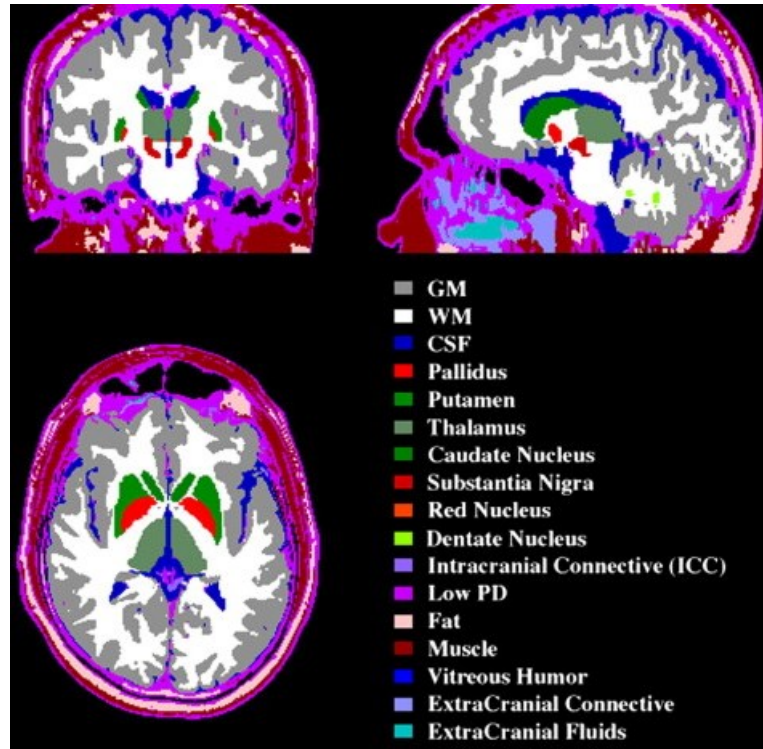
Figure 15 - Slices of Phantomag and tissue colour code of brain classification. The phantom represents an MRI study of a normal volunteer preliminarily segmented using a multi-parametric method based on a relaxometric approach.

For 3D modelling aimed at 3DP it is generally preferable to work with isotropic voxels, interpolating the images when voxels are anisotropic. The phantom has near-isotropic voxels of $0.9375 \times 0.9375 \times 1$ mm^3, which for our purposes, given the print resolutions (see **Section 1.6**) for which such differences would be irrelevant, can be considered isotropic of $1 \times 1 \times 1$ mm^3. For other reasons, which will become clearer in the following (**Section 3.3.2**), the phantom has been further interpolated (nearest neighbour, in order not to invalidate the binary segmentation) to bring it to a voxel resolution of $0.5 \times 0.5 \times 0.5$ mm^3.

3.3.2.   Design of Phantom Compartments

The segmentation of the digital phantom could not be directly used for the extraction of the 3D model of the new brain phantom. This observation would have been valid in general, since once a segmentation has been obtained, it must necessarily be "refined" for 3DP. First, to make sure that the brain compartments extracted from the images meet the design specifications. Secondly, because the segmentation should guarantee the definition of a correct STL model description and possibly ready for printing. Therefore, having observed the criticalities that would have occurred without further processing of the segmentation, it was necessary to implement an automatic refining procedure of the brain compartments of interest. The procedure was written in *Matlab® (R2018b)* and was followed by a manual editing phase for the connection of the parts of the striatum, and for the design of the tubes for filling. The processing made it possible to obtain three unique compartments on the images for the three required tissue compartments. Indeed, since this first phase of the creative process, we had found that the greatest difficulty lay in not wanting a solid model of the brain (which after segmentation and using the currently existing 3D modelling software would be relatively easy to obtain), but a phantom. In this case, an anatomical phantom, which is not simply an anatomical model. This implied the need to be able to extract the exact separation surfaces between the various tissues of interest. These surfaces will have to be closed, because they interface between separate compartments which will then be filled with different solutions to simulate CT, PET, SPECT, and MRI examinations.

3.3.2.1.   Definition of Compartments

As mentioned in the **Section 2.3.4.1**, seventeen brain compartments are identified in the brain images of *Phantomag* (**Figure 15**), while in our case we wanted to create only three compartments. Therefore, the first thing to do was to reduce the number of compartments from 17 to 3, considering the behaviour of the corresponding tissues from a nuclear-medical point of view. Having a clear map of the brain tissues available, it was defined the best association of the other tissues to the three of interest and which ones to associate with the value intensity of the background. In the association the brain anatomy was taken into account, reassigning the nuclei to the tissue between GM and WM according to position and physiology (i.e., by contiguity and appearance in nuclear medicine images). Low proton density extracranial tissues, fat, muscle, CSF, vitreous humour, nasal mucosa, extra-cranial fluids, and intracranial connective tissues have been associated with the background, in order to isolate only the brain matter from the background. Pallidus and thalamus have been associated with the GM to which

they are physically in contact and homogeneous in terms of tracer uptake for the ECT studies of interest (i.e., FDG-PET or ECD-SPECT). This association made the tissues a single compartment, which will be the compartment of GM. Substantia nigra, red nucleus and dentate nucleus, which are completely immersed in WM, without any direct contact with other GM structures, were associated with the WM to form the WM compartment of the phantom. In this way, each voxel of the images became distinctively associated with only one of the three compartments of interest. Finally, the caudate nucleus and the putamen have been associated to form the compartment of the striatum (**Figure 16**).
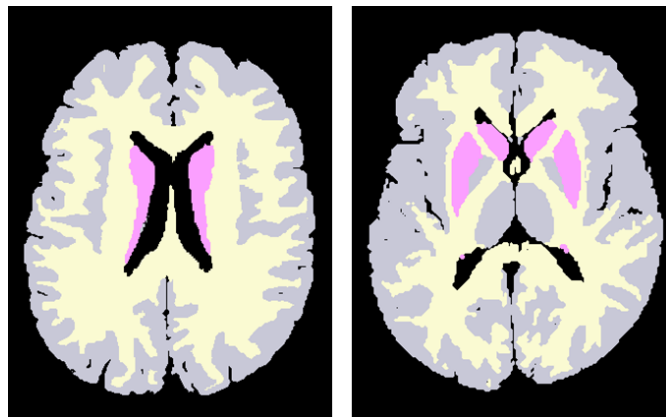
Figure 16 – Grey matter (GM), white matter (WM) and striatum segmentation. The figure shows two selected slices of the segmentation of GM (in grey), WM (in white) and of the striatum (in pink violet).

Following this initial assignment, it was necessary to verify that each of the three compartments was actually constituted by a unique section, without isolated subsections. This means that in the segmentation of the compartments there were no "voxel islands" of that same tissue, three-dimensionally disconnected from the main compartment. These would represent noise-shells (discussed in **Section 1.5.1.1**) in the STL model, resulting in problems for printing and impossible to fill with the remaining of the compartment.

3.3.2.2. Connection of the Voxels of the same Tissue

This check is onerous, as it is a punctual check made starting from one of the voxels of the selected tissue to define a neighbourhood and then a cluster of that tissue. Here, the term cluster refers to a group of contiguous voxels of the same type, three-dimensionally disconnected from other groups of that type or forming a single large group. The implemented routine automatically chooses the "seed" (i.e., a voxel of the specified tissue) from which to start the definition of a first cluster. Each cluster is defined using the automatic search for voxels of the same type adjacent to the seed in the three dimensions, which are then stored

in a stack. Once the first seed has been deleted (assigning it an intensity equal to that of the background), each voxel stored in the stack iteratively becomes the new "seed" around which to look to define the belonging of the adjacent voxels, then storing only those of the same tissue. Once all the voxels in the stack have been scanned, the first cluster is defined. At that point, it is checked whether there are still voxels of same tissue and, once one is found, the other clusters are defined iteratively. As an example, 47 tissue clusters for the GM compartment were identified on the *Phantomag* phantom. In particular, the largest cluster has been identified as the main cluster, and the others as "islands of voxels"; while 19 clusters were identified for the WM compartment. For the striatum compartment, only 4 clusters, corresponding to the two caudate nuclei and two putamina, were identified.

Having established the presence of these numerous small clusters for the GM and WM compartment, we studied how to transform them to make both GM and WM a single compartment (i.e., only one large cluster). This operation to reassign the "spurious" clusters is simple, but not trivial. Before defining how to proceed, a slice-by-slice visual analysis of the clusters of the entire volume was performed. In practice, being able to visualize the clusters in evidence with respect to the rest, it was observed that a valid method to eliminate them was to transform them into the tissue with the greatest occurrence among those adjacent to the specific cluster. To this end, a further routine has been developed, which reassigns them and finally verifies that both GM and WM have become a single cluster.

The striatum compartment also had to be a single compartment to be fillable. Therefore, also in this case, it was necessary to study a procedure useful for the unification of the four identified clusters. The initial idea was to create three-dimensional connections between right putamen and right caudate, right caudate and left caudate, and left caudate and left putamen. These connections would form tubes between one cluster and another, through which the filling liquid could flow into the physical phantom. However, going to act on the mesh, after the STL conversion, would not have been easy. The insertion of the connections between the various parts would have required a series of manipulations (cut and blending) with the consequent risk of running into the problems referred to in **Section 1.5.1.1**. Further to this, following this procedure the final model would significantly lose anatomical likeliness. Therefore, in this case, we have chosen to act directly on the segmented images. Wanting to maintain greater visual control over this procedure and not to distort the anatomical yield (the connections should be invisible at least to the nuclear medicine imaging) of this compartment, it was decided to recreate these fictitious connections in voxels, inserting them through manual editing. These connections have been imagined as a solid, in which (as for the rest of the phantom) walls of a chosen thickness

would have been excavated. Having defined as specific for the phantom a thickness that was between 0.4 – 1 mm (**Section 3.2**), channels were drawn in voxels such as to have a diameter of about 5 mm, to maintain a lumen of about 4 mm, inserted in the locations of minimal distance between the four clusters.

3.3.2.3. Inserting the Tubes

The same reasoning was followed for the insertion of the tubes of access to different compartments for filling (**Figure 17**). Therefore, having chosen the areas on the surface of the GM, the WM, and the striatum in which they were to be positioned, they are drawn directly on the images as solid cylindrical volumes (keeping for their voxels the label of the reference compartment) to have a lumen of about 6 mm (considering the maximum thickness).
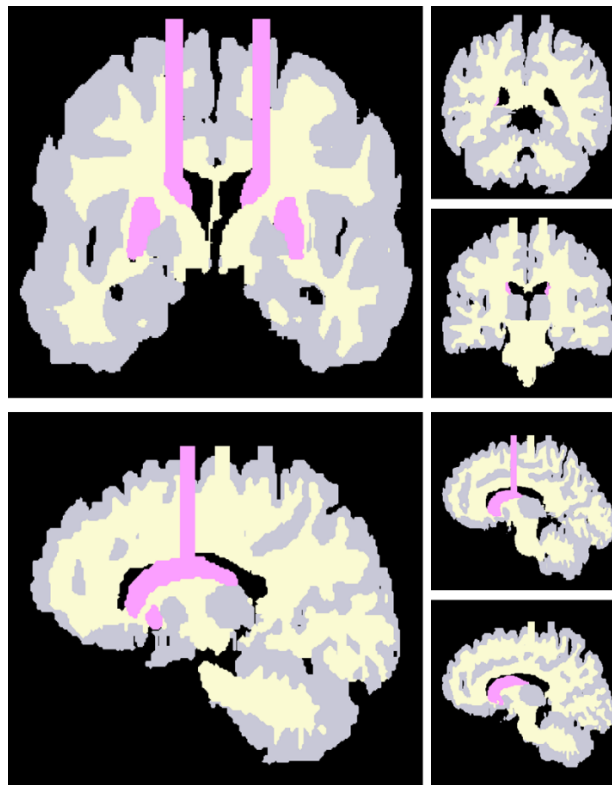
Figure 17 - Entering the volume of the tubes on the phantom images. The figure shows some coronal and sagittal sections of the phantom in which the segmentation of GM (in grey), WM (in white) and of the striatum (in violet-pink) is visible with the respective tubes inserted in the images.

3.3.3. STL Model of the Brain Phantom

We discussed the segmentation and its refining for the 3DP, still missing the extraction of the compartment surfaces to obtain a unique printable model and the realization of a correct STL file for printing. The solution that will be

presented was the result of the long research on 3D modelling, on STL phantoms and of several printing attempts. We have already repeated that printing cannot disregard the definition of the STL description, and vice versa, but what we want to underline in this section is how much the complexity of the shapes of the brain compartments inevitably complicates the transition to a polygonal mesh-based phantom and therefore to STL. The rendering of more complicated shapes requires an increase in the number of triangles in the mesh (and therefore a decrease in their area), significantly increasing their complexity and at the same time reducing the possibility of manipulating the mesh without incurring the typical errors of STLs (**Section 1.5.1.1**). Therefore, the rule was to find a fair compromise between the complexity of the shapes and the complexity of the STL, trying to minimize the manipulations steps on the mesh (extracted from the segmented images). The STL model of brain phantom was obtained according to the following steps.

3.3.3.1.   Extraction of Surfaces

It is certainly the most critical step of this section because it is fundamental for the creation of a correct and printable mesh. According to our initial idea, starting from the segmented images of the **Section 3.3.2**, the single compartments of GM, WM and striatum could be obtained through common medical image-to-STL conversion software. Hence, there were two ways to obtain the phantom: defining the anatomical models of GM, WM, and striatum (as volumes) and then obtaining the external surfaces through hollowing processes of the polygon mesh; or defining its mathematical surface and then giving it a thickness through extrusion processes from the surface mesh. Both solutions have been tested and considered extremely inconvenient for the realization of the phantom. Surface computation times became very long due to the same complexity of GM and WM shapes. Furthermore, even once the surfaces of each compartment were obtained, the Boolean union of the same could fail due to the high number of mergers of triangles on the interface surfaces between internal compartments. The resulting meshes then had overlapping triangles, duplicated faces, inverted normals and non-manifold shells (**Figure 2**), which made the model not exportable for printing. The polygonal meshes had so many problems that they could not be corrected even through the most popular and advanced mesh correction software (*NetFabb*, *MeshLab*, *MeshMixer*, *Magic*). Not being able to work directly on the meshes to define the surfaces, we went back to the images. Indeed, the surfaces at the interface between the various compartments can be defined in terms of voxels (voxelized surfaces). Obviously, this places a limitation on the thickness of the vertical and horizontal walls of the phantom, which can be at least equal to the size of the isotropic voxel. However, a

minimum vertical wall thickness of 0.5 mm is acceptable, since it is already below that declared by 3D printer manufacturers (see **Section 1.5.2.2**). The same goes for the minimum printable horizontal wall thickness which instead (as we will see in **Section 4.3.2.1**) depends on the setting of the layer height.

Therefore, the idea was to define the voxelized surfaces at the interface between the different compartments of the phantom, in order to obtain an already corrected STL file using the medical image-to-STL conversion software, on which only small manipulations for the insertion of threaded junctions would be required (see **Section 3.3.3.4**). For this purpose, the latest version of the developed pipeline, after correcting the segmented images (as in **Section 3.3.2**), automatically extracts single voxelized surfaces at the interface of compartments of interest from the segmented images of digital brain phantom by selecting voxels (from the outside towards the inside) sharing vertices, edges and faces (**Figure 18**). The voxelized surfaces was designed according to this criterion because the only one that ensures the extraction of a "non-perforated" STL surface connected in all its points. For this reason, as a last check, the extraction routine verifies that the final thickened surface of phantom is unique and closed.
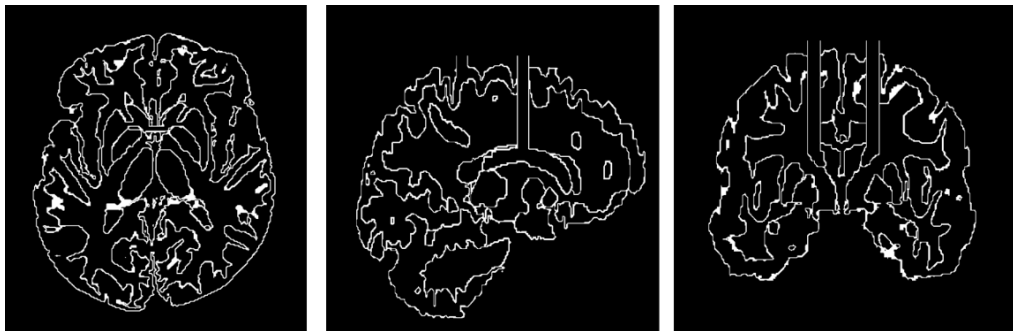
Figure 18 - Single voxelized surfaces at the interface of GM, WM, and striatum. From left to right the figure shows an axial, sagittal and coronal view of the voxelized surfaces extracted for the definition of the STL of the anthropomorphic brain phantom. Note, in the axial slice, the connections between the caudate and the putamen in the striatum, in the coronal and sagittal slices, the tubes of the GM, WM and striatum.

3.3.3.2.   Extraction of Polygonal Mesh-based Phantom

Starting from the voxelized surfaces, the extraction of the polygonal mesh of the phantom can be done using a medical image-to-STL conversion software. The thickness of the vertical walls will therefore be at least equal to the size of the voxel, 0.5 mm, and thicker in the oblique areas at the interface between the compartments. The triangular mesh was derived using the tools of the *3D Slicer* software, an open source software platform for medical image informatics, image processing, and three-dimensional visualisation [52]. The processed images therefore contained only the voxelized surface to which a label had been

assigned. Therefore, the Model Maker module of *3D Slicer* was used to create 3D surface models from label map, employing a high-resolution 3D surface construction algorithm called Marching Cubes [53]. For this operation it is possible to set a smoothing parameter (Smooth) according to the design requirements, which sets the number of iterations for smoothing with Laplacian filter, or the degree of the polynomial approximating the windowed Sinc function (setting it to 0 disables the smoothing). Furthermore, to ensure the model fits smoothly (like jigsaw puzzle pieces), it is possible to flag "Joint Smoothing". Also, a decimation parameter (Decimate) for the 3D mesh is available to help streamline the model by reducing the number of faces that make up the triangular mesh surface. Indeed, when not needed, having a 3D mesh with too many faces would make the manipulation of the 3D model unnecessarily too burdensome for the correction and printing software that would have to process it later (**Section 3.3.3.3** and **Section 4.3**), while, removing a few faces, does not necessarily mean compromising the shape and the structure of the meshed element, but simply lightens the STL file. The decimation of a mesh works respecting the characteristics of a model. The faces of a mesh on a quite uniform plane (a smooth vertical wall) are reduced more sensitively than those that define irregular and more complex shapes, such as GM circumvolution and WM fibres. Therefore, a scrupulous decimation factor still preserves the geometry and shapes, while saving a lot of weight of the exported model file. In the Model Maker tool, it is possible to reduce the number of polygons as a decimal percentage (between 0 and 1) of the number of polygons, specifying the percentage of triangles to be removed (for example, 0.1 means 10% reduction). We do not flag "Split normals", because this option could leave the creation of holes in surfaces, while we flag the padding option, "Pad", to ensure the production of closed surfaces. After several modelling (and printing) attempts with "Smooth" variable in the range between 0 and 10 (default value) and "Decimate" in the range between 0.1 and 0.25 (default value), the modelling (and printing) result, obtained setting 10 and 0.1 respectively, was found to be the best for our needs. With these settings, the right compromise was made to eliminate the unsightly effect of the voxelization on the surface (which could at the same time complicate the printing), while maintaining a faithful representation of the anatomy of the brain tissues. The polygonal mesh-based model so created, was then exported in STL format (**Figure 19**).

3.3.3.3.   STL Refinement

Before printing, the STL file needed further refinements and corrections. For these operations we used *Autodesk®'s NetFabb®* (v. 2019.0 64-Bit Edition) software for additive manufacturing, design, and simulation. The software

provides a set of tools designed for triangular mesh design and validation. In this case, the model in STL format had no problems in the triangular mesh, so no correction was initially needed. However, other manipulations were required to complete the accesses to the phantom via the tubes. The phantom has in fact two tubes for each compartment. One tube is used for filling, while the other is for the escape of air during filling (**Section 4.5**). The tubes had already been "drawn" on the images starting from two selected points to the right and left of the medial line at the apex for each of the compartments, thus becoming part of the compartment surfaces (**Section 3.3.2.2**). Threaded joints were added to each tube to screw caps on the phantom to ensure hermetic seal after filling. The junctions (specially designed, as described below in **Section 3.3.3.4**) were inserted on the phantom by means of Boolean union operations (performed in *NetFabb®*) and finally the mesh was corrected for any error that could be generated on the area of the pipes during the manipulation.
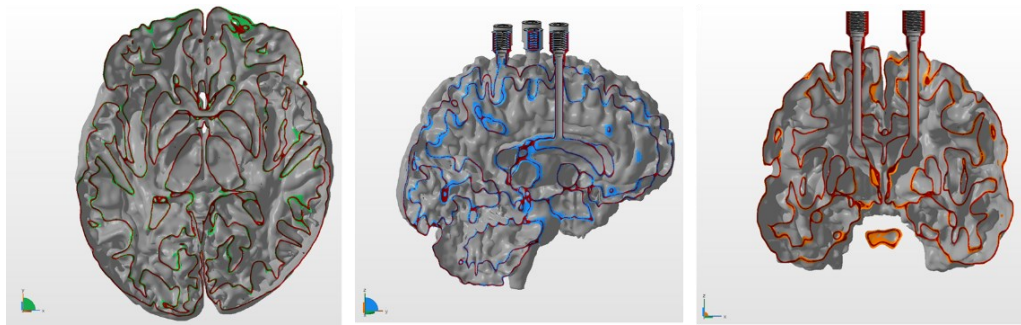
Figure 19 - Views of the internal structure of the anthropomorphic brain phantom. From left to right we have the axial view, the sagittal view, and the coronal view of the modelized anthropomorphic brain phantom. They correspond to the voxelized surfaces shown in figure Figure 18. Note the interface walls between the various compartments of GM, WM, and striatum.

3.3.3.4. Threaded Junctions and Caps

These parts have been designed to allow the screwing of caps to hermetically close the phantom after filling (**Figure 20**). Both the threads and the caps (also to be made with the 3D printer) have been designed in *Tinkercad®*. It can be used online, and it is another *Autodesk®* software, but compared to other CAD software it has the advantage of an extremely intuitive interface, which seems to transfer the strict rules of technical drawing in an environment suitable even for less experienced CAD design users. *Tinkercad®* exploits addition, subtraction and grouping logics that allow creating even quite complex models. Furthermore, the *Tinkercad®* community also makes available a series of already designed geometric figures and pieces, which can easily be combined to create the envisaged object. In our case, these tools have allowed the realization of the threaded joints and consequently also of the caps to screw into them.
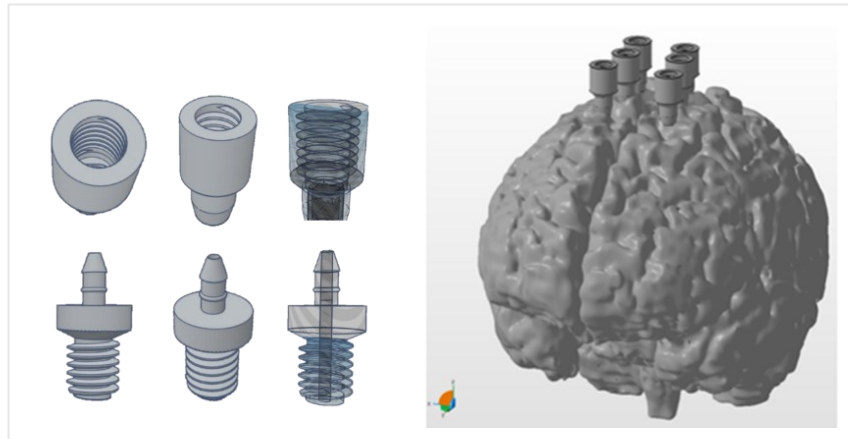
Figure 20 - Threaded joints and connecting caps for the filling system. *The figure shows (left) the threaded joints (upper row), designed in Tinkercad® and inserted on the finished phantom model (right). In the lower row (left) shows the threaded caps with fitting for connection to the silicon tubing of the filling system.*

Chapter 4

Prototyping of the New Brain Phantom

4.1. Introduction

In this chapter, the intention is to gradually transmit the experience gained in these years for the prototyping of the new brain phantom. The materialization of such a complex phantom using 3DP is not straightforward and requires a lot of time both for printing tests and to obtain the complete part. Despite the boom of the recent years, 3D printers are still far from being *plug-and-play* (or rather, *plug-and-print*) devices. To print an object, it is still necessary to personally define a printing toolchain, following a series of different steps. Therefore, the experimentation, the study of the problems and the continuous tests, have gradually inspired the path of in-depth analysis of the 3DP technologies (presented in **Chapter 1**), which has gradually detected a series of aspects (not always openly declared) regarding the deposition, and the actual characteristics and properties of different printers and materials. The choice of the technology and a printer suitable for the specific application was not immediate and required years of *trial-and-error*, and careful investigation before acquiring a professional machine of the highest level. Indeed, in order to understand the actual performance of 3D printers, beyond the overt ones, as well as any limitations, it would be necessary to be able to test them for the specific printing application. Clearly, this does not constitute a viable possibility, nor an optimizing choice, with respect to the waste of money and time that would result.

4.2. Choice of 3D Printing Technology

When selecting the most suitable 3DP technology for the specific task, it is reasonable to start from the most advantageous technologies, among those suitable for the purpose, in terms of cost, performance, range of usable materials and structural properties (surface finish, visual appearance, accuracy, precision, environmental resistance, useful life, thermal properties of components, etc.). We have reflected not only on the specifications of the brain phantom, but above all on the limits that each of the 3DP technologies could present for the realization of a phantom with such a complex shape due to the necessary support

structures/material. Indeed, among others, the most critical specification for the phantom, which also goes beyond the complexity of the brain shapes, is to want a single object, in which the compartments result only from the interface surfaces between the different brain tissues (as a kind of matryoshka). This entails the need to materialize empty parts that during printing must necessarily be "filled" with supports to ensure success. Starting from this point of view, among the technologies presented (see **Section 1.3.1**), the best candidates would be FDM (**Section 1.3.1.4**) and PolyJet (**Section 1.3.1.2**), both widely used for printing anatomical models and both with strengths and weaknesses for the realization of phantoms [31].

4.2.1. FDM and PolyJet in Comparison

FDM and PolyJet® are the two leading technologies of *Stratasys* (a leading company in the sector, see **Section 1.2**). These two 3DP technologies, in fact, are among the most advanced and effective ones available today, as they allow the production of robust and durable models with fine and precise details [54]. As discussed in **Chapter 1,** FDM is a material extrusion-based technology while PolyJet is based on material jetting. They offer the right solution for many applications, but before deciding which one to use for the prototyping of the brain phantom, it was necessary to carefully weigh the operational aspects, the characteristics of the parts, the materials available and the differences in the support structures/materials. These two technologies are quite distinct and provide different results, although there are some overlaps in terms of applications and advantages.

4.2.1.1. Operational Aspects

Compact and space-saving systems, suitable for office environments, and ease of use are aspects that only partially define the interest in these technologies. Approaching the world of 3DP, the workflow and construction times are by right the most relevant aspects which, in addition to the speed of the machine, also involve the preliminary and post-printing operations. The speed of construction, while being a priority for many users, is actually an imperfect measure of performance, and to define it many factors should be considered [55], so it is not an adequate term of comparison between the two technologies. As regards the preliminary operations, in particular, the processing of the STL files for printing, it is noted that both technologies allow preparing of slicing paths for printing through both user-friendly and more advanced slicing software. From this point of view, FDM production (even in FFF implementations, **Section 4.3.1**) has the further advantage of allowing the user to add advanced controls (by modifying

the parameters that regulate the construction process, **Section 4.3.2.1**) in order to meet specific application requirements. The operations after printing are instead those relating to the removal of the supports and any post-processing of finishing the piece (such as waterproofing and/or polishing).

4.2.1.2.   Differences in the Support Structures/Materials

The supports are usually created by automatic slicing software with the aim of supporting the projecting parts of the printed pieces for a limited time to their construction, for FDM and Polyjet printers, until the deposited material solidifies (see **Section 1.5.2.3**). As an example, we can refer to the scaffolding used in construction. To create balconies or attics a scaffolding is required, which must be placed before the deposition of the materials (such as cement, mortar, etc.), being pourable or malleable upon their deposition, to subsequently become rigid and capable of supporting a load. Following the solidification of the materials, the scaffolding is removed. The scaffolding must have at least two specific characteristics. It must be stable and strong enough to effectively support the material that will be placed and must be easily removable. Since the purpose is the same, our supports must also have these two characteristics. The supports are fundamental in the realization of complex models (which contain protruding parts) or hollow models (which do not have lower layers to support those printed at a certain level) [56, 57]. In these cases, in fact, printing is only possible thanks to the realization of supports. In FDM, if the printer has only one extruder, the support structures are made of the same material with which the piece was printed. They have a reticular structure whose manual removal can be rather complicated, sometimes impossible [58]. While with dual extruder FDM printers, the supports can be made of a material different from the main one. There are specific materials for supports which dissolve in specific liquid solutions. Also, with PolyJet printers can be created subsequently removable supports, which typically take on a dense honeycomb shape. Where support is required, the printer deposits a gel-like material, which can be removed at the end of the print by means of a strong waterjet and various soaking/rinsing phases [59]. Therefore, from the standpoint of support removal, this technology is best suited for materializing simple open phantoms, with few internal compartments (e.g., heart phantoms). In the realization of very complex closed phantoms, even if hollow and with access pipes, in fact, many areas may not be reached by the waterjet. For this reason, the PolyJet phantoms are printed in different parts to be assembled later [60]. This would have general advantages such as the reduction of the number of supports with consequent reduction of the printing time, and the saving of printing material, but at expenses of the quality and precision of the model. Our anthropomorphic brain phantom is characterized by

multiple convoluted compartments and internal structures, so in addition to the classic external supports it also requires many internal supports, necessarily soluble. Unless we greatly simplify the model, giving up the anatomical rendering, printing a brain phantom like ours, in several parts, would become very difficult. A cut made along any one plane at any level would result in some parts of the phantom being unconnected after the supports are removed, making the process of gluing the parts extremely complicated. The FDM phantoms, on the other hand, can be completely cleaned from the internal and external supports, without repeated washing, simply by immersing them in a washing tank filled with a basic solution (see **Section 4.3.2.2**). Therefore, since there are tubes for filling, the solution also fills the inside of the phantom, dissolving the support structures and leaving the compartments empty.

4.2.1.3.   Characteristics of the Parts

Part characteristics include important elements affecting print quality: surface finish, fine detail, precision, and size. In terms of surface finishing, PolyJet shows greater potential than FDM, a technology for which surface finishing is a more problematic aspect [54]. PolyJet allows obtaining practically ready surfaces, without particular evident imperfections, directly from the 3D printer. On the other hand, the FDM extrusion process can produce visible lines of the layers on the side walls, as well as any signs of tool paths on the upper and lower surfaces. In most cases, such imperfections can be eliminated, but this requires additional post-processing. Thanks to the post-finishing of the piece, and with appropriate waterproofing techniques (discussed in the **Section 4.4**), it is also possible to waterproof the objects printed in FDM to make them watertight. In fact, the deposition process inevitably leaves gaps in the print weft through which water can pass after a certain amount of time [61]. In our case, the waterproofing problem is critical mainly because we need a vertical wall thickness of less than one millimetre. However, even with wall thicknesses greater than a millimetre, a hollow object printed in FDM is still not watertight, while in PolyJet there would be fewer waterproofing problems, even for sub-millimetre wall thicknesses, but the problem of the supports would remain. On the other hand, as far as dimensional accuracy is concerned, the published specifications show that comparable FDM and PolyJet platforms have similar results for the size of the parts just removed from the system. Finally, over time and under load, FDM materials are dimensionally more stable than PolyJet materials [54]. This aspect is critical if, as in our case, the aim is to produce a final part, that is a phantom that will have to be used several times and in particular conditions.

4.2.1.4. Materials

The 3DP materials have already been described in detail in **Section 1.7**. The available materials determine the obtainable physical properties, such as stiffness, flexibility, durability, transparency, biocompatibility, and other performances. Currently, one of the main differences between FDM and PolyJet lies in the materials [54]. The options offered in both cases are many starting from real thermoplastics to thermoplastic-like resins, from rigid materials to more flexible ones, from opaque to transparent. PolyJet is the best platform in terms of range of product properties and realism, especially thanks to the ability to print multiple materials in one print job (multi-material printing). On the other hand, however, if the applications require the use of real, functional, and durable thermoplastics, the best choice is FDM.

Table 2 - Summary table of Pros and Cons of FDM and PolyJet technologies compared. Comparison of the pros and cons of using FDM or PolyJet technology in the production of the anthropomorphic brain phantom.

Technology	Pros	Cons
Fused Deposition Modelling (FDM)	• Strength, stability, and durability of the final part • Better mechanical properties of the final part • Use of common thermoplastics • Easily removable soluble supports	• Visible lines of the layers on the side walls • Waterproofing required • Post-finishing of the printed objects
PolyJet	• Smooth surfaces and fine details • Appearance and consistency of the final product • Flexible materials • Multi-material printing	• Greater weakness of printed parts • Soluble supports removable with waterjet • High costs

4.2.2. FDM Technology for the Materialization of the Phantom

Following the considerations discussed in the previous paragraphs, our technological choice fell on FDM (pros and cons of investigated technologies are summarized in **Table 2**). The goal was to materialize the modelized anthropomorphic brain phantom to complete the prototyping process of a new device for testing brain imaging equipment. Keeping in mind the extreme

complex shapes of the phantom, the possibility of obtaining a very refined object had to balance with the necessity that the object was functional, providing good performance, at least in terms of strength, stability durability. The main constraint that oriented us toward the FDM choice was however the need to produce a one-time printed, internally hollow object, with sub-millimetre wall thickness. Therefore, in addition to the classic external supports, many necessarily soluble internal supports also had to be printed. In this way, once washed/filled with specific solution and then emptied, the phantom would have been completely cleaned of the internal and external support structures.

4.2.2.1. Technical Characteristics of FDM 3D Printers

Once decided the technology to be used, the key point was the selection of a high-performance 3D printer to allow the materialization of our model at a sufficiently high level of definition, at a reasonable cost. Thus, having identified the 3DP technology, we moved on to select the FDM printer among the many and various possibilities on the market. The choice of a professional 3D printer could not ignore, in addition to the application requirements, the satisfaction of specific performance criteria that can guarantee, in their entirety, greater advantages. Below, we briefly discuss the main technical characteristics of the 3D printers to be taken into consideration for the choice.

Build volume (mm³). It is essential to consider the size of the object to be printed. The object must fit within the workspace, preferably not to the limit, as a space that is not large enough with respect to the model could cause defects or unexpected events during printing. The evaluation of build volume is especially important when objects cannot be printed in several parts, such as our brain phantom. For our model, we need a build size around $170{\times}200{\times}200$ mm³.

Nozzle diameter (mm). This feature of FDM printers is important because it mainly affects two other factors which are the printing speed and accuracy [62]. In practice, the smaller the diameter, the more precise and detailed, but therefore also the slower, the print is. Whereas the larger the diameter, the more difficult it is to recreate very small details, but at the same time the printing is faster. The nozzles have a diameter ranging from 0.25 to 1 mm, passing through various intermediate sizes. For the construction of the phantom, this diameter is of considerable importance. As stressed several times, in fact, the thickness of the vertical separation walls between the various compartments must be sub-millimetric, between 0.5 – 1 mm and, therefore, for printing to be successful, it is important to ensure an adequate diameter (thicknesses, lower than the diameter of the nozzle, are not printed).

Printed speed (mm/s). Often this information is provided for entry-level or semi-professional printers, while for high-end printers it is usually not indicated. Indeed, it is an imperfect, indicative and often unreliable measure of performance, because it is a parameter of difficult definition, which takes on different meanings depending on the type of FDM printer. The speed of 3D printers is not an absolute value, but depends on the possible acceleration, the shape of the object and the material [63]. Knowing that a machine has a certain maximum speed should not lead one to think that it can always work at that speed. On the contrary, it will hardly be able to reach it since the paths to be taken (especially when printing very complex and detailed objects that require several movements of the extrusion nozzle) are generally too short. Consequently, the speed with which the extruder manages to reach the desired speed, or acceleration, matters more. In addition, the printing speed is linked to the thermoplastic characteristics of the material, which impose limits. For the above, it is understandable that the speed indication is of little significance, if it is not matched to an indication of the print quality [64].

Resolution, layer thickness and accuracy. These metrics generate a lot of confusion and deserve special attention for this. As already extensively described in the **Section 1.6**, when it comes to printing resolution, we must distinguish the resolution in the (x, y) plane and the resolution in z, often referred to as layer thickness. It is well known that 3D printers work layer-by-layer, therefore, it is natural that the minimum obtainable layer thickness determines the maximum printing resolution in z [29]. However, a high-resolution object is not necessarily more accurate, as it is often inappropriately stated. Accuracy must also be distinguished from the ability to reproduce the smallest detail, which is instead the resolution in (x, y). The latter, like the one in z, allows us to obtain objects of excellent quality, but not necessarily accurate in terms of size. In this case, the smaller the slightest head movements, the better and more defined the details of a print [62]. However, it should be borne in mind that although the machine can perform perfect movements and micro-movements, everything is still linked to the diameter of the nozzle. In fact, the minimum reproducible detail/feature always depends on the nozzle diameter, and generally does not exceed the size of 0.3 mm [62, 63].

Number of extruders. This was of considerable importance in our case. To be printed, the brain phantom needed external supports, but above all internal ones, to support the parts, which necessarily had to be made of a soluble material in order to be able to remove them completely at the end of printing. Therefore, the FDM printer used had to have at least two extruders, one to deposit the main material and the other the material of the supports.

Maximum printing and printing-bed temperature. Often, especially for entry-level and semi-professional FDM (or rather, FFF) printers, these two characteristics are declared. They are both related to the range of thermoplastic materials that the printer can deposit [65]. Therefore, they are generally implicit for professional printers where temperatures are automatically set for the material loaded for printing.

Printing-bed. On entry-level and semi-professional printers, the print bed can be made of aluminum, steel, plexiglass, wood, glass, or other special materials. In professional printers, on the other hand, it is made of a plastic material similar to printing ones. It is a very important element that must, on the one hand, facilitate adhesion to the first print layer, and on the other, facilitate the detachment of the object at the end of printing. Generally, the printing bed is also heated to ensure better adhesion of the extruded filament and to avoid any deformations that may occur for cooling the deposited material. This feature is in fact essential to be able to print some types of materials, such as ABS.

Calibration. Another crucial aspect, related to the print bed, is calibration. Inaccurate calibration is often the main cause of poor-quality printouts. When the printer is not equipped with an automatic calibration system, manually recalibration is needed after only a few prints. The same goes for the calibration of the printheads.

4.2.2.2.   The 3D Printers used

We arrived at the materialization of the brain phantom prototype through two phases. In a preliminary phase, we tried to obtain the prototype using a semi-professional printer (*Raise3D N2 Plus*). While at an advanced stage, we chose a professional FDM printer (*Stratasys F370^{TM}*) of the F123 series, marketed by *Stratasys*, which then led to the working prototype (**Section 4.3.2**). This operational choice must be contextualized in today's 3D printer market.
As explained in **Chapter 1**, when the FDM patent expired with the birth of the open-source development communities, much cheaper printers than professional FDM machines were designed. For these, the technology was renamed Fused Filament Fabrication (FFF), in place of FDM which would refer exclusively to the *Stratasys* patent (**Section 1.2**). This breakthrough initially involved mainly hobbyists and anyone taking their first steps in 3DP field, with fairly high-performance machines, but with relatively lower characteristics and capabilities than the high-end ones. In recent years, however, the market for FFF 3D printers has also expanded a lot in the sense of semi-professional printing, leading to high-performance machines, but with a cost reduced by a factor of about 10 compared to the previous market targets. The processing methods of the FFF are

almost identical to those of the FDM, so it was the differences in the technical characteristics of the machine and in the proprietary materials (especially, support material) that made the second (*Stratasys F370^{TM}*) more suitable than the first (*RAISE3D N2 Plus*) to our production needs (**Table 3**).

*Table 3 - **Main technical characteristics of the 3D printers used.** The table shows the technical characteristics of the 3D printers identified and used in this work. It is possible to observe how some specifications declared for the FFF technology (nozzle diameter and printing speed), are instead not declared for the FDM technology, for which instead different layer heights are specified as the printing material varies.*

Technical Characteristics	Raise3D N2 Plus	Stratasys F370^{TM}
Printing Technology	FFF	FDM
Build Volume	280×305×605 mm³	355×254×355 mm³
Nozzle diameter	0.4 mm (Default), 0.2/0.6/0.8/1.0 mm (Available)	ND
Printing speed	30–150 mm/s	ND
Accuracy	XY-axes: 0.0125 mm Z-axis: 0.00125 mm (positioning accuracy)	Parts are produced with an accuracy of ±0.200 mm, or ±0.002 mm/mm, whichever is greater.
Layer height and Materials	0.01 – 0.25 mm • Construction materials: PLA, ABS, HIPS, PC, TPU, TPE, NYLON, PETG, ASA, PP, PVA, Glass Fiber Infused, Carbon Fiber Infused, Metal Fill, Wood Fill • Soluble support: HIPS for ABS and PVA for PLA.	• 0.330 mm (ABS, ASA, PC-ABS) • 0.254 mm (FDM TPU 92A, PLA, ABS, ASA, PC-ABS) • 0.178 mm (ABS, ASA, PC-ABS) • 0.127 mm (ABS, ASA, PC-ABS) • QSR support material (soluble) for ABS and TPU.
Number of extruders	2	2

4.3. Brain Phantom Materialization

Our experimental tests, carried out to date, highlighted two critical issues for our application, due to the current limits of the FDM/FFF technology.

The first problem is represented by the minimum vertical wall thickness that can be materialized with FDM/FFF, generally required at least 1 mm thick, even for high-end printers, while our brain phantom requires a submillimetre wall thickness (between 0.5 mm and 1 mm), sturdiness and impermeability.

The second problem we faced is that both external and internal supports are needed to print the phantom. These latter are particularly difficult to manage. Unlike external ones, they cannot be removed manually and when automatically generated by common slicing software could be not perfectly efficient. Furthermore, the required amount of internal support greatly extends the printing time. The reduction of supports using slicing software, does not always result in having efficient supports at critical points. The new brain phantom materialization workflow is schematically summarized in the **Appendix**, **Flowchart (C)**.

4.3.1. Development with Semi-professional Printer

Both problems have been evident since initial phases of our prototyping experience, during which we used the FFF technology printer (*Raise3D N2 Plus*). Working with this type of printer, even before experiencing the critical issues due to the specific application, we had the opportunity to experiment with all the common problems of FFF 3DP (warping, elephant foot, missing levels, pillowing, stringing), and understand the causes. According to our experience, all the problems of entry-level and/or semi-professional 3DP are related to thermoplastic materials and the deposition process. For each material, the printing parameters had to be studied, which also vary from manufacturer to manufacturer. Although this left more freedom in customizing the slicing settings for our application, on the other hand it inevitably requested a series of countless printing tests to find out which combination of printing parameters gave the expected printing result through a necessary *trial-and-error* approach. To demonstrate the printability of the designed 3D model, and to address the waterproofing problem (already found on test objects), in the first instance, we decided to "circumvent" the problem of soluble supports, to analyse it later, by leaving them of the same printing material (**Figure 21**). The first rudimentary prototype of the new brain phantom was printed using a very common plastic, Polyethylene Terephthalate Glycol (PET-G), using supports automatically generated by the slicing software that accompanies the *Raise3D* printers (*ideaMaker*). PLA and ABS have also been tested, however, PLA is not suitable

for objects that must be in contact with aqueous solutions (it can swell and deform), while the various types of ABS available for medium-low range printers could have problems of lifting and warping for long prints, which would require temperature-controlled printing chamber.
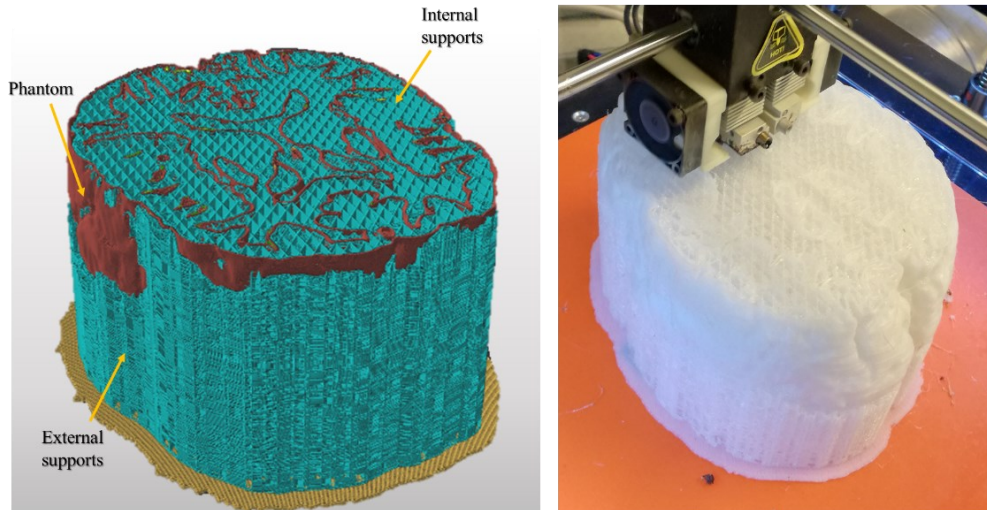
Figure 21 - Phantom with not soluble supports. On the left we see the slicing of the phantom obtained using the ideaMaker by Raise3D software. The yellow arrows indicate the phantom wall, external supports, and internal supports. As can be seen, these have a grid structure and fill the cavities of the brain phantom to support its walls. Furthermore, the structure of the supports (as can be seen on the external ones) has a texture with alternating layers that makes them permeable and allows to test the filling of the phantom. The figure on the right shows the corresponding phantom when printing with only one extruder and one material.

The default support settings (support type: lines, overhang: 45°, dense support: no) resulted in inefficient support structures generation at critical points. Consequently, the printed parts had holes and other defects. To ensure efficient support at all points we had to change the slicing settings for support structures (support type: grid, overhang: 10°, dense support: yes). In this way, the supports practically filled the cavities of the phantom at all points (**Figure 21**). The dense support, printed in the layer immediately preceding the one where the deposition of the phantom's surface begins, ensured more efficient supports in critical points. Furthermore, these grid supports were permeable and with a vertical wall that would be invisible to nuclear medicine imaging, which still made the phantom prototype usable.

However, the large amount of required supports greatly extended the printing time. If the printing time increases, the likelihood of printing problems increases, as these printers do not have efficient print head cleaning systems. Despite this, once we defined reliable automatic supports, we tried also to understand if it was possible to obtain waterproof walls by modifying other printing parameters. In

FFF printing it is possible to change the temperatures and the printing speed, among others. According to our experience, speed significantly affects quality, as well as printing time, although it is a difficult parameter to interpret. For PET-G by maintaining a printing temperature of 145°C and lowering the printing speed from 50 mm/sec (recommended) to 20 mm/sec, we were able to obtain an "apparent" impermeability (**Figure 22**).
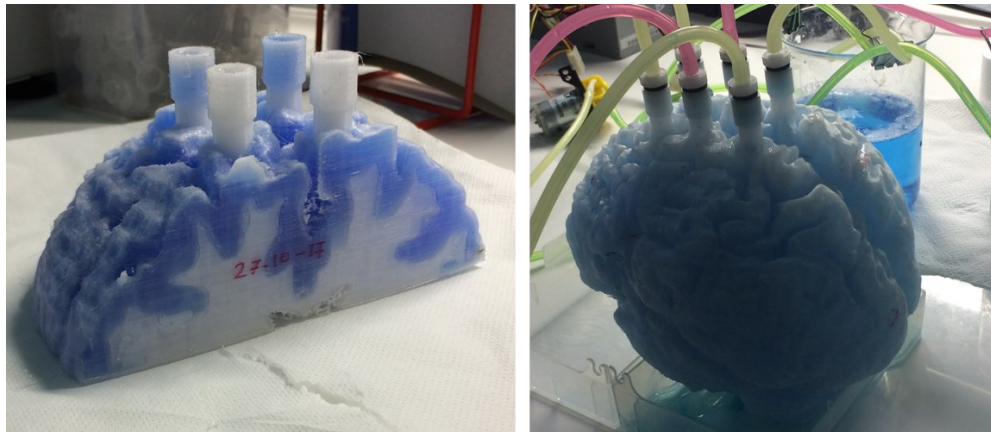
Figure 22 – Phantom waterproof tests. On the left is shown a partial print of the phantom obtained with transparent PET-G material on which the (apparent) impermeability, achieved by optimizing the printing parameters, has been tested. It was filled with blue coloured water to distinguish the two compartments on the side wall from the outside as well. The compartment of the GM was filled without passage of water in the WM. This situation was maintained for a short time (from 10 minutes to half an hour on test prints), after which there was an exudation of the liquid from the GM to the WM. On the right is shown the filling of the first rudimentary prototype of the complete phantom is shown.

"Apparent" because it was verified for short times (from 10 minutes to half an hour) while for long times the water was still able to cross the print weft, passing outside and between the compartments. For this reason, we concluded that with material extrusion 3DP it is practically impossible to obtain watertight parts with such thin wall thicknesses. The only possible alternative was to develop an appropriate waterproofing system (**Section 4.4**).

The complete model took 8 days and 16 hours to print. The absence of a temperature-controlled chamber makes long prints critical. In many cases, they fail because the piece detaches from the print bed. Among other materials, PET-G suffers less from shrinkage, although it has some stringing on the pieces. However, it does not have a soluble support material with which it can bind. Therefore, for FFF printing the alternatives to investigate could again be PLA, printed with PVA as the support material, and ABS printed with HIPS. PVA is a water-soluble material, while HIPS is soluble in limonene (**Section 1.7**). Due to its hygroscopicity, PVA is not suitable for long prints, while HIPS, despite having a good aesthetic yield, requires, like ABS, very high printing temperatures to be maintained throughout the construction process. Indeed, ABS

and HIPS could have been appropriate for our purpose, however, we verified that by switching to dual extrusion printing the printing times with the *RAISE3D N2 Plus* would be practically doubled compared to those of single material printing, becoming unacceptable, considering the limited stability of the system.

4.3.1.1.   Automated Design of Efficient Supports

The printing time mainly depends on the level of detail (resolution, layer height and accuracy) and the number of supports of the model. The brain phantom's compartments are very convoluted, resulting in numerous critical points for 3DP. These points are located mainly in correspondence of deep ripples and sulci that characterize the compartments of GM and WM. In these and other points, holes may be created during FFF 3DP due to a verisimilar absence or inadequacy of supports, which are automatically inserted by the printing software, following the overhangs of the surfaces, but sometimes failing to support the critical points due to complex shapes of the phantom. For this reason, we proposed an automatic method for the generation of efficient support structures useful for FFF 3DP of complex anthropomorphic phantoms to support exactly and only the critical points [66]. The whole procedure for the automated design of *ad-hoc* support structures was implemented in *MATLAB® (R2018b)*. The voxelized surfaces of modelized phantom (**Section 3.3.3.1**) were preliminary analysed to identify all those points that need to be supported during 3DP.
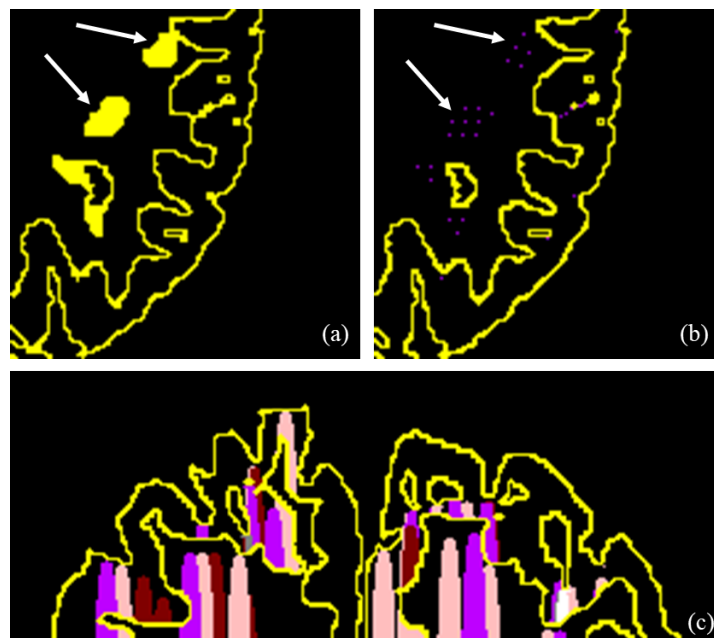
Figure 23 - Horizontal view of critical points and support structures. *(a) transversal critical areas (arrows); (b) their corresponding critical points (arrows) in the next lower slice; (c) example of a coronal view of labelled paraboloid-like generated supports.*

These critical points were selected by setting two searching rules:

1. All surface voxels being at a lower level than all neighbouring voxels per side or vertex are to be supported;
2. All voxels not having contiguous voxels at the lowest level, or previously individuated critical points, within a 2.5 mm (5 voxels) neighbourhood along the horizontal or vertical directions must be supported.

Then, the points from which the supports will start have been placed just below the critical points. In order to minimize the amount of support, our approach creates paraboloid-shaped shells, to support all and only the previously identified critical points. To this aim, paraboloid-like 3D voxels volumes were added to the images (**Figure 23**). They were first positioned to pin their vertices on critical points, and then truncated in correspondence of voxelized surfaces of the phantom, in order to avoid overlapping with those surfaces [66].
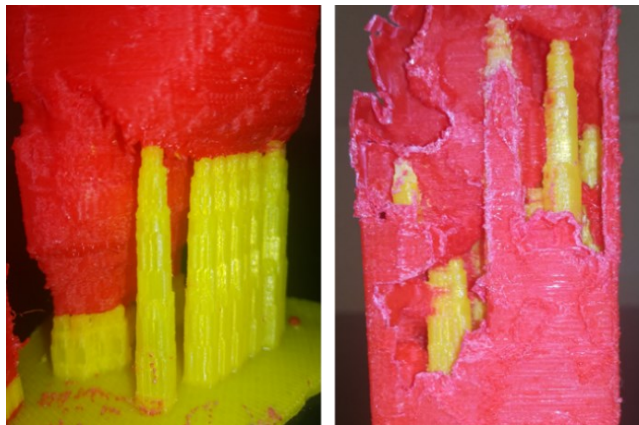
Figure 24 – Dual extrusion tests of ad-hoc supports. *The figure shows a double-extruder printing of a portion of our brain phantom printed with ad-hoc supports. In the figure on the right the piece was conveniently opened to show internal supports.*

The *ad-hoc* designed supports efficiently and adequately support all and only the critical points, requiring a smaller amount of support material along with a significant reduction in printing times compared to traditional support structures (**Figure 24**). Moreover, we tested the possibility of making them of soluble material to free the phantom from internal supports. The dissolution of our *ad-hoc* soluble supports, resulted faster than that of traditional ones on the same piece, since all supports surfaces were immediately reached by the liquid solvent [66]. Nevertheless, in entry-level and semi-professional printing, the interaction between the two nozzles still remains a difficult issue. Manual printhead calibration can be very inaccurate, causing interactions between the printheads and newly deposited material. Moreover, despite the retraction activation, these materials suffer from the annoying problem of dripping, which makes them

practically unusable for very long and complex prints. Reducing the amount of supports certainly reduces time, but as long as the materials of the FFF print are not improved it may not be the best choice in the creation of such complex anthropomorphic phantoms.

4.3.2. Development with Professional Printer

From our preliminary experiences with the FFF 3DP technology, we concluded that, although it takes up the principles of the FDM, to date it does not possess the necessary requisites for the printing of our anthropomorphic brain phantom. Therefore, the first actual prototypes, tracing all the characteristics defined in **Section 3.2**, were obtained using the *Stratasys F370^{TM}* professional 3D printer. This machine ensured greater reliability in successful printing of complex objects, shorter printing time and less man-hour wasted in solving the problems of not professional printing. The material chosen for printing is ABS, which has a specific material for printing soluble supports (QSR support). ABS is by far the most used plastic in 3DP, it has a very low cost and an extreme resistance, which allows it to be used for prototypes that must guarantee durability and stiffness over time. In fact, ABS is a particularly robust and impact-resistant plastic that provides durable parts (resistant to use and wear). In addition, it is very versatile and slightly flexible and can withstand temperatures up to about 85°C without undergoing deformation.

4.3.2.1. Optimization of Printing Parameters

STL models can be prepared for printing using *GrabCAD Print* slicing software for *Stratasys* 3D printers. The 3D slicing results' visualization allowed us to obtain more details on the model to be printed by being able to view the layer-by-layer deposition path of the printing material and supports. Thanks to the slicing preview, it is in fact possible to identify problems that can be corrected in advance before starting printing. However, not all problems in the extrusion path can be solved using the basic version of the software. Alternatively, files for the *Stratasys F370^{TM}* printer can be prepared using *Insight for GrabCAD* software, the *Stratasys' Advanced Slicer*. The latter was born for use in industrial contexts; therefore, it allows users to maintain maximum control over the support structures and the material extrusion paths. Unlike the basic *GrabCAD* software, with *Insight*, users can manually edit the printing parameters and manipulate the extrusion toolpaths for advanced controls on the properties of the printed object.

Study of the basic printing parameters. The first printing tests of the anthropomorphic phantom were obtained using the basic version of the

GradCAD Print slicing software. Only a few printing parameters could therefore be set, to simply define the finishing and sturdiness of the piece, without being able to intervene directly on the printing paths. The layer height values that can be set for ABS printing on *Stratasys* systems are 0.3302 mm, 0.2540 mm, 0.1778 mm, and 0.1270 mm (**Table 3**). For printing the modeled brain phantom (**Section 3.3**), layer height values greater than 0.1778 mm were found to be unsuitable. In FDM 3DP, the width of a line of deposited material is approximately twice the layer height, therefore where the vertical wall of the phantom had a minimum thickness of 0.5 mm, the extruder was unable to deposit two juxtaposed lines, because the sum of the line thicknesses would have been greater than that of the STL model. In this case, the printing path of the vertical walls was discontinuous, resulting in gaps and cracks in the walls (**Figure 25a**). Even selecting the "Increase Thin Wall Thickness" setting to allow the slicing software to automatically increase the thickness of thin vertical walls did not completely solve the problem (**Figure 25b**).
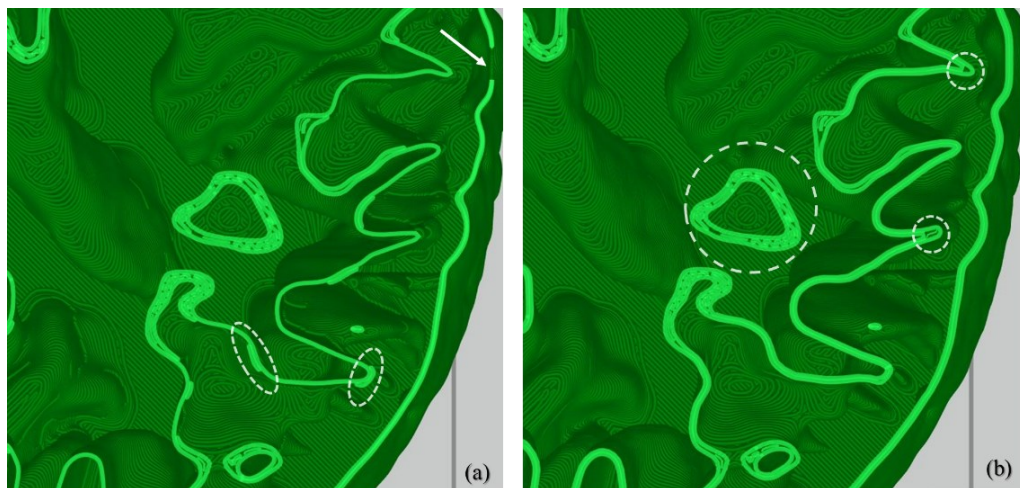
Figure 25 – Problems in the printing path of the vertical walls of the phantom with inappropriate layer height. Figure (a) shows the printing path obtained with a layer height of 0.254 mm. The arrow indicates a very thin wall area (equal to about 0.5 mm) on which slicing process is unable to describe a line (which would be about twice as thick as the layer height exceeding the thickness defined in the STL model). In the two circled areas there are two parts of the wall where the single printing line would have juxtaposed a broken line. The printing result would be a discontinuous wall with unsolvable permeability problems. Figure (b) shows the printing path obtained with a layer height of 0.254 mm, adding the option for thickening the vertical walls. These are composed of two juxtaposed lines, but problems of large air gaps persist in the print texture (circled areas).

Furthermore, when printing with a layer height of 0.2540 mm or more, the slicing of the horizontal (or near horizontal) walls of the 0.5 mm thick phantom would result in a single printed layer. The sum of two layers would actually have a thickness greater than the thickness defined by the project, hence only one layer would be described in the resulting path (**Figure 26).** Therefore, to ensure that

at least two juxtaposed material lines for the vertical walls and more than one layer for the horizontal walls (with a minimum thickness of 0.5 mm) were
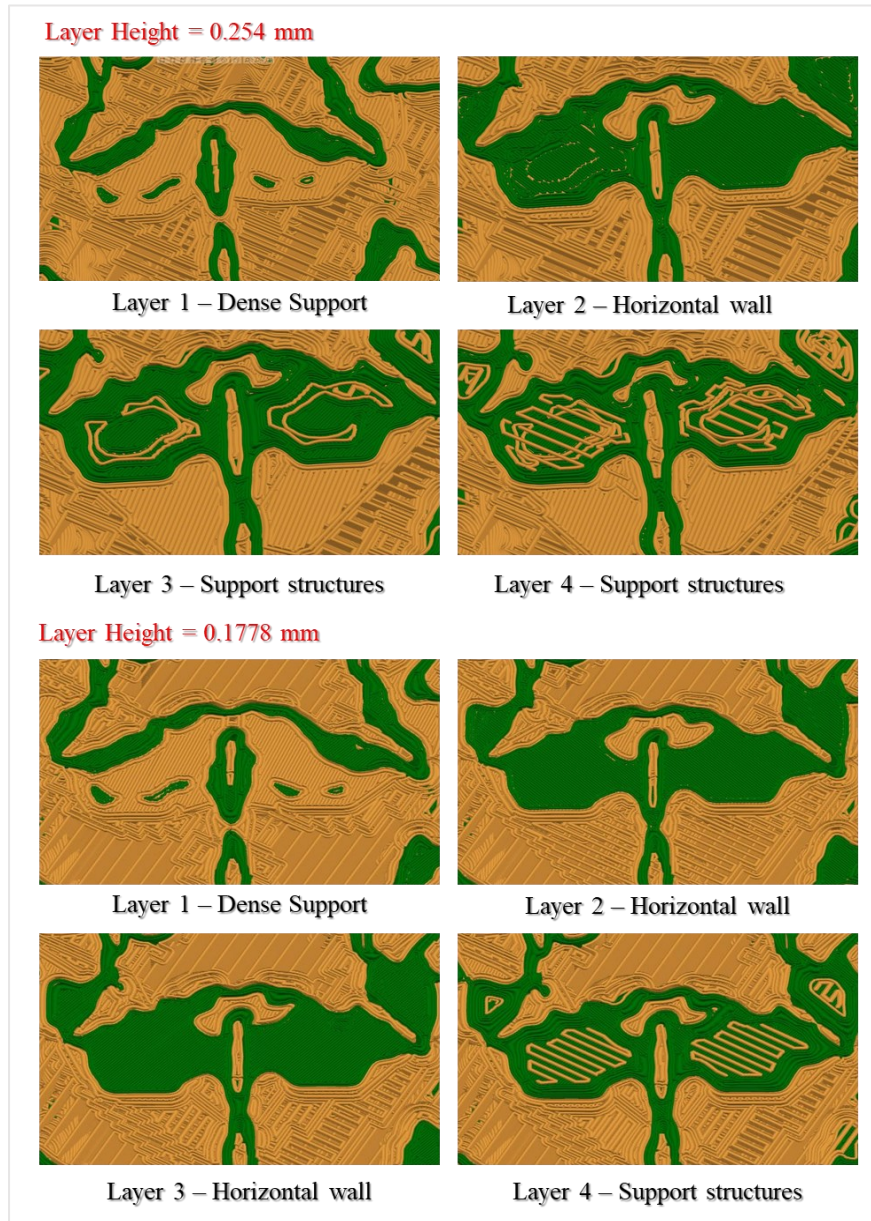
Figure 26 - Problems of the horizontal walls of the phantom with inappropriate layer height. *The figure shows the sequence of the four layers corresponding to the horizontal wall at the base of the thalamus in the phantom, for layer height equal to 0.254 mm and 0.1778 mm. In the first case (Layer Height = 0.254 mm) only one layer of material (Layer 2) is printed for the horizontal wall, while on all the others in that area support is deposited (on Layer 1 there is the dense support that supports Layer 2; on Layer 3 and 4 the support structures that will support the next higher layers). This means that the wall at the base of the thalamus is not strong and corresponds to a single 0.254 mm thick layer. In the second case (Layer Height = 0.1778 mm), however, two layers of material are printed (Layer 2 and Layer 3), while the supports are deposited on the layers placed before and after the base of the thalamus (Layer 1 and Layer 4, respectively). In this case, the wall of the base of the thalamus is robust because it consists of two 0.1778 mm thick layers.*

deposited, a layer height of at least 0.1778 mm had to be used (**Figure 26**). In theory, the most appropriate layer height value could be 0.1270 mm, however, in practice this setting should be avoided for at least two reasons. First because it would greatly lengthen printing times, not necessarily improving the printing result. Second because, contrary to intuition, the printing of such complex objects with a low layer height is not recommended (when not strictly necessary), to reduce the likelihood of running into problems during long and expensive prints. Therefore, prints obtained with a compromise layer thickness of 0.1778 mm are more stable and guarantee a higher probability of the printing success.

Study of the advanced printing parameters. The pieces printed with this printing resolution had an excellent surface yield without apparent holes in the wall. However, in pursuing the attempt to waterproof the phantom, further optimization of the printing parameters was necessary. This was in order to define the best printing toolpath, given the advanced settings available in the *Insight software for GrabCAD*. The goal was to identify the best configuration of the slicing parameters to strengthen the vertical walls, and to thicken as much as possible the texture deposited in the filling of the horizontal walls, while ensuring continuity of the printed walls, minimizing the presence of small holes and air gap in the same walls (**Figure 27**). The *Insight* toolpath setup offers the possibility to select an important advanced option for the slicing of brain phantom, "Use variable width remnant fill". By enabling this option, the slicing software tries to fill empty areas, which would remain in the print texture, using small amounts of material. Multiple contours (2 with thickness of 0.3048 mm), with negative contour to contour air gap and negative contour to raster air gap (both of -0.0254 mm) were selected as part fill style to ensure that there was an overlap between the deposited threads, to "sealing" the remaining space between two tracks of cylindrical material. According to the same logic, to improve the vertical and horizontal surfaces of the phantom, enhanced visible rasters and enhanced internal rasters were set at 0.3048, raster angles were set at 45°, with negative visible raster air and negative internal raster air gaps (both of -0.0254 mm).

Settings for generating support structures. The *Stratasys F370^{TM}* printer can print a support material (QSR support) which is soluble in a sodium hydroxide solution. Soluble support structures are designed to dissolve in a wash station (**Section 4.3.2.2**), leaving only the model material behind. The generation of complex structures, with hollow compartments and channel embedded within the parts is one of the biggest obstacles in design for 3DP, as the internal support structures should follow the internal surfaces of the compartments and channels/tubes along the entire piece. For this reason, the use of soluble support

material relieves issues that we encountered and explored for non-professional FFF printing (**Section 4.3.1**).
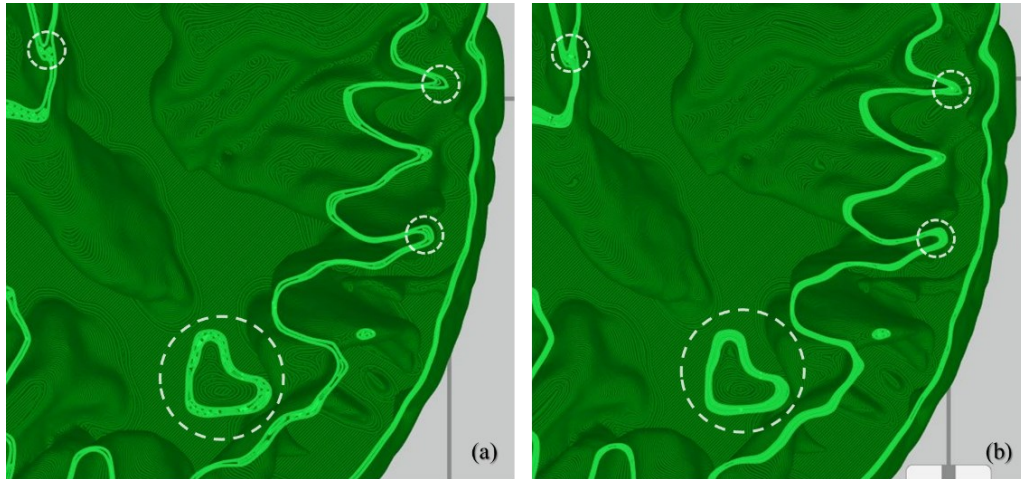
Figure 27 - Optimized printing toolpath. *Figure (a) shows the printing toolpath obtained with GrabCAD Print software setting layer height equal to 0.1778 mm and option for thickening thin walls. Many residual air gaps were present in the print texture (circled areas). Figure (b) shows the printing toolpath obtained by optimizing the printing parameters using the Insight for GrabCAD software. The air gaps in the phantom walls are significantly reduced (circled areas).*

Stratasys slicing software for FDM allows the automatic generation of optimized and customizable soluble support structures on the base of user input. In *GrabCAD Print* and *Insight* there are some options for generating the support, mainly "sparse", "surround" and "SMART". There are also some other types of support structure, such as "basic" and "box", which basically are variations of "sparse" and "surround" respectively. The different support structures can be briefly explained as follows:

- Sparse support uses the simplest support generation method to build structures based on the layer overhang. The overhang angle is different for each printer, but the average generally tends to be around 45 degrees (see **Section 1.5.2.3**).
- Surround support wraps the entire model inside a support shell to maintain stability during the printing process. This type of structure is excellent for tall parts with small areas.
- SMART support uses a series of optimization algorithms to determine the best possible support generation using the least amount of material. Basically, the supports contain sides that taper off reducing the amount of material required.
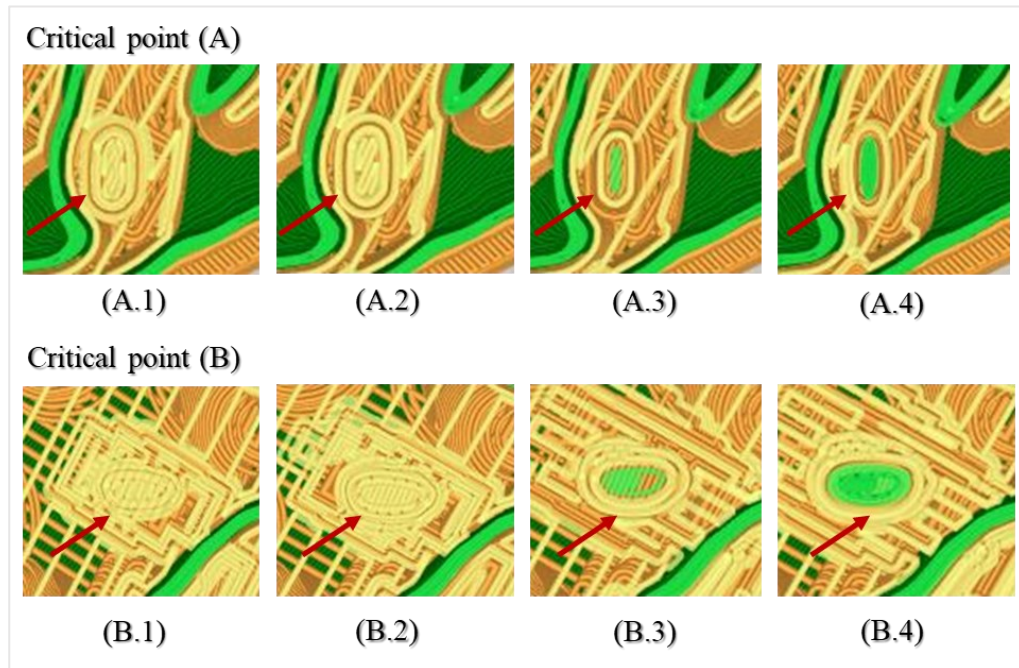
Figure 28 - Example of SMART support for critical points of the brain phantom. The figure shows four sequential layers of the printing path of two phantom's critical areas (red arrows) which we can call point A and point B. In both points the support structure is preceded by two layers of dense support (A.1, A.2 and B.1 and B.2). In the subsequent layers (A.3 and B.3) a trace of material is deposited which therefore has a minimum anchoring area to the support. If the substrate were not dense on the previous layers, the adhesion surface would be even smaller. Therefore, when layers A.4 and B.4 are printed, the traces on layers A.3 and B.3, while undergoing a slight stress due to the deposition process (during which there are minimal retraction forces of the material), remain firmly and construction can proceed. Otherwise, the track of material on layers A.3 and B.3 could become detached (flying off the print piece), effectively leaving a hole in the inner wall of the phantom.

In any case, the support structures provide dense layers just below the first layer of construction material deposited on them (**Figure 28**), to facilitate its adhesion to the support and prevent its detaching from the supports in the most critical points during the print. If a small area of material were deposited on a non-densified support, it could lift off the support (to which it is weakly attached) during the stresses for the construction of successive layers, or even fall into the structure of the supports. SMART support is the best option for most 3DP applications and is indeed already set as the default support type in *GrabCAD Print*. Densities cannot be changed in *GrabCAD Print*, however they can be manipulated using *Insight*. *Insight*'s toolpath customization parameters allow setting the distances between parallel and adjacent contours and rasters for supports as well. Although there is the availability of customizing the support, in this case it would not be the perfect compensation strategy to increase efficiency and reduce printing and washing times. Therefore, after various tests on partials of the phantom, we were able to detect the efficiency of SMART

supports in printing complex anatomical surfaces, without making further changes of the default parameters.
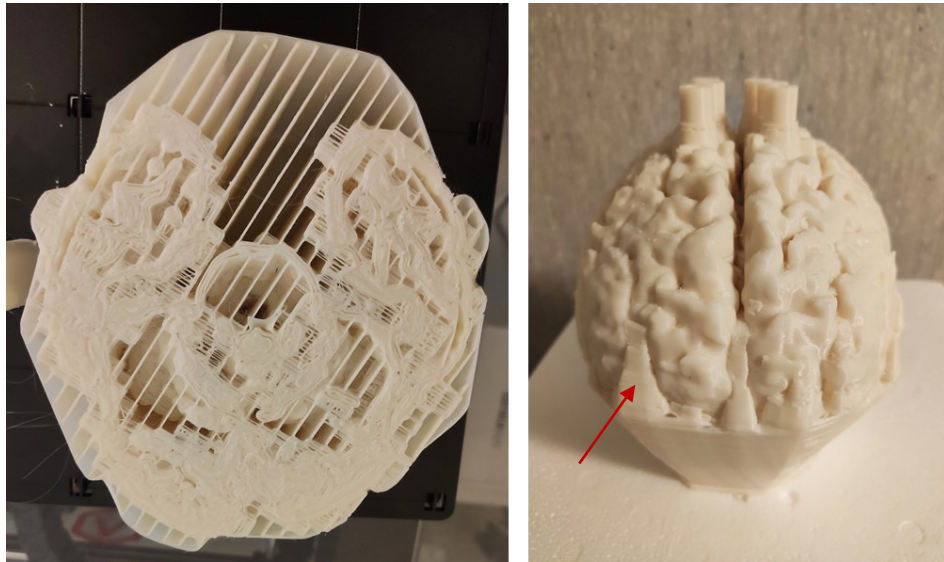
Figure 29 – Internal and external supports. The figure on the left shows the internal structure of SMART supports. In the figure on the right the external structure of the SMART supports for the printed prototype.

Printing the brain phantom took 7 days and 3 hours, 146.66 cm^3 of ABS material and 524.87 cm^3 of QSR support material. The printing time is still long, even if less than that required for printing the first rudimentary prototype in FFF technology (**Section 4.3.1**, **Figure 22**) in a single material (in FFF dual-extrusion printing would have required about twice as long). The increased reliability of professional FDM 3DP ensured the success of long prints and the repeatability of the prototype print.

4.3.2.2. Removal of Soluble Supports

The *Support Cleaning Apparatus* (SCA-1200HT) was used to remove support structures. SCA units, along with wash salts (based on sodium hydroxide), are specifically designed for the removal of soluble support materials on 3D printed parts and are compatible with *Stratasys* soluble support materials. The cleaning process is naturally very slow, and it is not easy to understand how long it will take to clean the specific part. Unfortunately, there is no proven method for accurately determining part washing times. It is possible to make very large estimates, but there are many factors constantly at play that could affect the dissolution process. The type of support and the density of the support structure are the first factors to determine the washing time, but they are not the only ones. SMART supports are "lighter" and take less time to dissolve, simply due to

material optimization. The temperature of the washing station is another determining factor, however, the SCA unit allows setting the right temperature (70°C) to maintain it throughout the washing process. Given all these factors, time also depends a lot on the complexity of the printed piece, and in the case of our phantom, on the internal support structures that fit into the entire volume of the compartments. Internal supports take much longer to clean than external supports as they do not get immediate exposure to the wash solution and there is also not the same exposure in all internal parts at the same time. The liquid can in fact reach and fill the cavities only as it encounters and dissolves the supports. The non-impermeability of the structures printed with FDM technology helps in a certain sense in the process, because it allows the liquid to permeate inside the compartments. In addition, the washing tank has a liquid handling system which, by moving the piece, facilitates washing, up to the most critical channels. After each wash, the tank decreases its washing power, in proportion to the amount of support dissolved therein. Consequently, another aspect that should be taken into account when washing such a complex phantom is how saturated the tank is with loose supports. A freshly prepared tank naturally has greater washing power, and therefore provides a clean piece in less time. In any case, according to our estimates, a phantom in a freshly prepared washing tank is cleaned of the external supports in about 4 hours, to complete the washing of the internal supports in about 24 hours of washing.
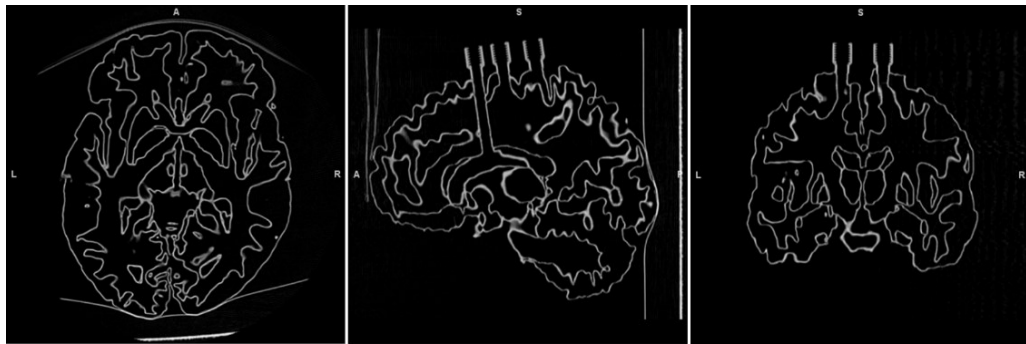
Figure 30 - CT scan of the phantom after washing. By CT scan it was verified that the washing system had dissolved all internal support structures. As can be seen in the figure, the compartments of the GM, WM and striatum are empty and completely free from the internal supports.

To verify that the phantom was completely cleaned of internal supports we performed a CT scan (**Figure 30**). The empty and dry phantom weighs approximately 250g (before waterproofing). This weight was taken as a reference for the phantoms printed subsequently. Starting from the weight it will be possible to understand if the phantom is empty without necessarily carrying out a CT.

4.4. Waterproofing

Although the walls have been designed to be a "solid" object, also through the optimization of the printing parameters (**Section 4.3.2.1**), several factors can preclude their complete waterproofing. Among the known factors, there are incomplete adhesion of the layers or compromises in the trajectory of the extruder [67]. To these, according to our experience, we also add the intention of printing vertical walls of reduced thickness, compared to the minimum thickness declared as materializable (without complications) by the 3D printer manufacturers (at least 1 mm, **Section 1.5.2.2**). All these factors are intrinsic to the FDM technology, therefore, more than optimizing the printing parameters to obtain a printing texture with a minimized number of air gaps, it cannot be done. This can be a problem when there should be no contamination between compartment specific solutions, as in our brain phantom. Therefore, once the prototype of the phantom was obtained, proving that walls with a thickness of less than 1 mm could be printed with a certain reliability, to make the phantom work it was however necessary to develop an appropriate waterproofing technique. Indeed, for this object it is not enough to guarantee the impermeability of the outermost compartment (GM), but it is also necessary to guarantee it for the internal compartments (WM and Striatum), so that once filled, the liquid does not pass from one compartment to another, and/or outwards.

Techniques for waterproofing FDM 3D-printed parts are known and widely used. Generally, the most reliable ones involve the use of waterproof epoxy resins to coat the external surfaces and, when possible, the internal ones [67]. The resins are very viscous, and, in most cases, they can solve the waterproofing problem. However, due to the viscosity, and the fact that the internal compartments are accessible only through tubes, it is not possible to use these resins for the waterproofing of our phantom. On the other hand, the resin would thicken the walls of the phantom and could remain and accumulate in the narrow channels of the phantom, invalidating the effort made to obtain the best anatomical performance, or even making the phantom unusable. This is also the reason why phantoms are generally printed in several parts, subsequently waterproofed and glued with the same resin [25, 67, 68].

Therefore, new techniques have been tested for the waterproofing of 3D-printed phantoms in one piece and with several internal compartments.

4.4.1. Waterproofing with Acetone

Chemical approaches with dimethylketone (acetone) have a significant effect on the surface roughness of some 3D-printed parts. It can penetrate the print weft, sealing the residual air gaps. Dimethylketone was chosen due to its low cost,

very low toxicity and to his very high diffusion. Although it might be inapplicable to some built materials, such as PLA, as they do not react chemically, it is a good choice for post processing ABS [69]. The latter is a polymer with a low degree of crosslinking, including the functionality of nitrile, which exhibits an interaction with polar solvents, such as dimethylketone, esters and chloride solvents [70]. The ABS printed parts are usually finished with a pure acetone vapor bath to increase the aesthetic result. The visual effect is in fact a smoothing and polishing of the piece which makes the appearance very pleasant. However, undiluted acetone could very quickly dissolve ABS and erode the features of the printed parts. The interaction process with pure acetone is difficult to control, therefore, the bath is usually added with water due to its very high mixability with acetone [70, 71].

Following this indication, we have established for how long and in what concentration to expose the printed phantom to acetone vapor, through an accurate *trial-and-error* procedure. The experimentation was performed on empty cubes with a wall thickness equal to that (minimum) of the phantom (0.5 mm), to evaluate the effect of acetone concentration and exposure time on thin walls (both in terms of resulting deformations than waterproofing). The mixtures, with a water-to-acetone ratio of 1, 1/2 and 2/3, were tested for different exposure times (20 minutes, 30 minutes, 1 hour). The best solution was that with a ratio of 1 for a duration of 30 minutes, for which waterproofing of the cubes was obtained without deformation in a short time and with acceptable deformations after 1 hour. The other two concentrations led to waterproofing with unacceptable deformation results. The same waterproofing procedure was tested on a (open) part of the phantom in which the compartments were observable, and the achieved waterproofing could be tested (**Figure 31**). The piece was waterproof and there was no passage of liquid from one compartment to another. However, although the acetone vapor bath waterproofing had immediate effect on the exposed external surfaces of the piece, or those that the steam can reach in half an hour, the same does not apply to the internal ones that cannot be reached. The same procedure applied to the complete phantom would waterproof only the external part, leaving the internal compartments permeable. Therefore, to waterproof the internal parts rather than the acetone vapor bath, we tried to identify the right concentration for a solution of water and acetone that could be poured into the internal compartments, to transfer the effect of acetone on the walls without causing damage. Pure acetone could not be used because once the phantom is emptied, a certain amount could become trapped in it and stagnate, to the point of generating holes in the ABS walls due to the long exposure time. On test cubes (like the previous ones) we proved that water prevented pure acetone from damaging the surface by lowering its solvent power. The same solutions were tested, with the same water-to-acetone ratios

and times tested for vapor bath. The best result was obtained again with a ratio of 1, for a time equal to 30 minutes, however, even extending the time to 1 hour there was no damage to the piece, but only more prominent deformations. After being exposed to the solution, the walls of the cubes remain wet, and the acetone has time to act until completely dry. The impermeability could therefore only be tested once the cube was dry.
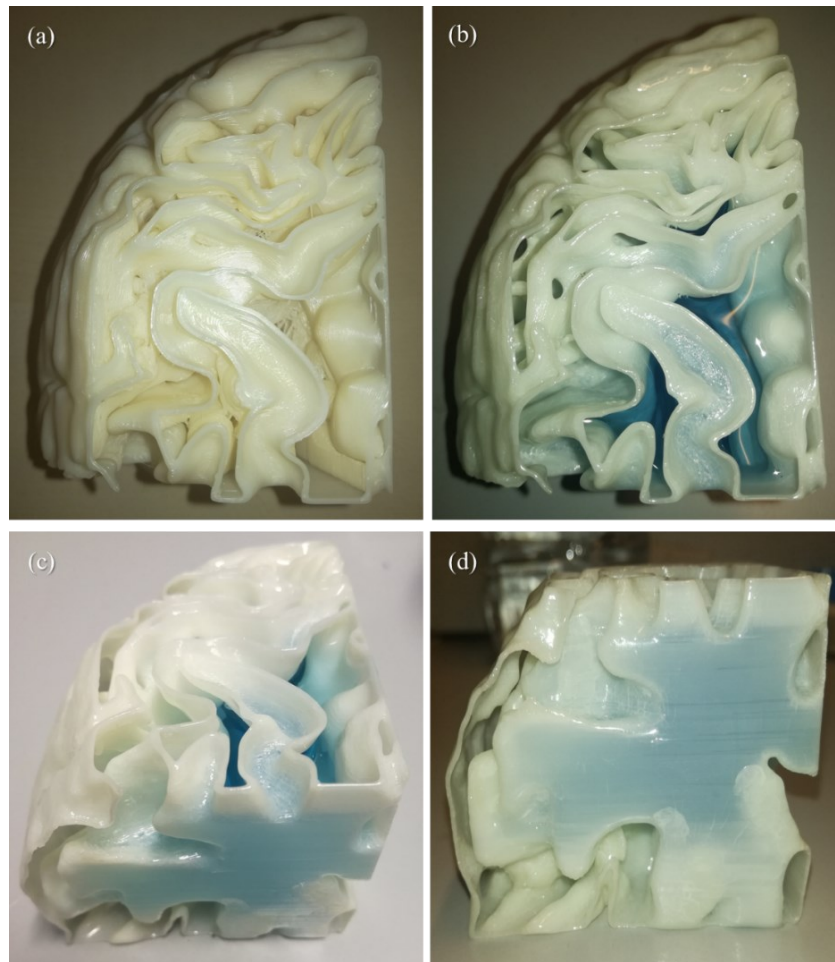
Figure 31 - Waterproofing test with acetone vapor bath. Figure (a) shows the piece just printed without any treatment. Figures (b), (c) and (d) show the piece after cleaning the supports and treatment with acetone vapor bath. The greater lucidity of the parts is due to the treatment. The piece was also waterproof and, as can be seen from figure (c) and figure (d), there was no passage of liquid between the two compartments. The compartment filled with blue coloured water is a part of the WM, enveloped by the GM in which the liquid did not pass by oozing the walls.

The whole phantom was filled with a similarly prepared solution of water and acetone. After the treatment (lasting 30 minutes) and the complete drying of the phantom (favoured by a heated environment) the impermeability between the compartments was tested, finding that a certain amount of liquid still passed between GM and WM. Another 5 treatments were required to complete the

waterproofing. The repeated treatments were justified by the fact that with each new treatment, the amount of liquid that passed into the WM, once the GM was filled (and vice versa), was reduced.
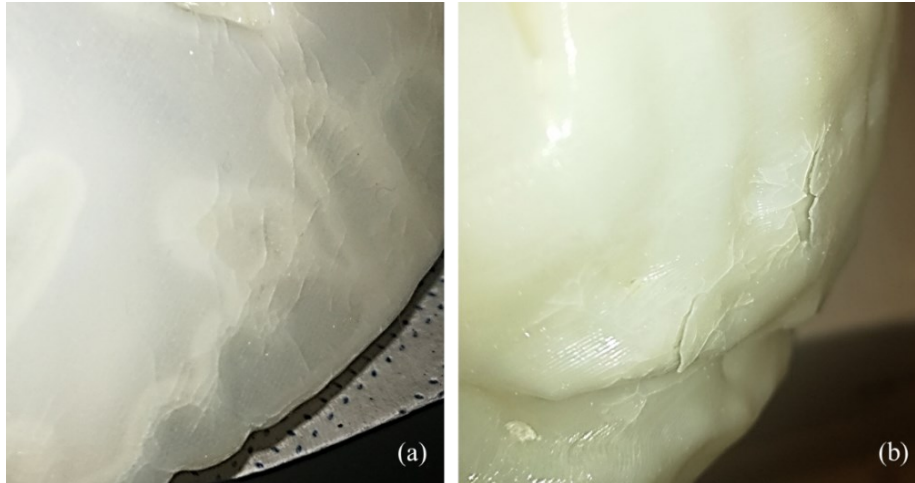
Figure 32 - Damage to the ABS walls after repeated treatments with acetone. Damage to the ABS walls after repeated treatments with acetone. Acetone actually deteriorates ABS, therefore, while it offers the possibility of waterproofing the pieces, on the other, the process is very difficult to control. The phantom has such complex walls that it is unthinkable to obtain waterproofing in all points with a single treatment. To allow the acetone to have an effect on all areas of the phantom, the treatments must be repeated. Repeated treatments cause cracks in the walls, as in figure (a), which in the long run led to detachment of layers of the same, as in figure (b).

Despite having obtained the waterproofing, the phantom with each further treatment presented more and more evident cracks in the external structure (and presumably also inside). These cracks have increased over time to the "flaking" of the two printed wall thicknesses in some areas (**Figure 32**). For this reason, the treatment with acetone for waterproofing was considered unreliable, unstable, and non-repeatable, as already suggested by other authors for other applications [69, 71]. For the watertight requirements of our brain phantom, repeated treatments are required (so that all areas are reached and sealed) which inevitably deteriorate the ABS.

4.4.2. Waterproofing with Polyvinyl-acetate

More recently, we have developed a more stable waterproofing technique that replaced the chemical approach using acetone in the treatment of ABS. The idea was to use a solution that did not chemically react with ABS, but that could penetrate the print texture by physically closing the micropores in the printed surfaces. To this aim, we looked for a sticky material that remained trapped in the air gaps of the structure, filling them, and then drying and remaining stuck to the walls in a stable manner. Generally, the glues have a viscosity that does

not make them suitable for filling the phantom, while the vinyl glue is a dispersion of water-based polyvinyl-acetate resins, therefore it can be diluted with warm water to lower its viscosity and make possible to fill the phantom. As an added benefit, it is widespread, has a low cost, low toxicity, and non-annoying smell. It is widely used also for gluing porous surfaces, because the hardened glue (by eliminating water) forms a soft, transparent, and elastic film that sticks to the surfaces. In the presence of water or humidity, the glue, even when hardened, tends to become soft again, but not melting. However, there are special resins to be added before gluing which allow obtaining glues that are also water resistant. For our treatment we have chosen a commercial water-repellent vinyl glue. The treatment was tested on test cubes to identify the right volumetric percentages of water and polyvinyl acetate in the dilution. The best percentage by volume, according to our experience, was 20% polyvinyl acetate and 80% water. The same treatment was applied to the printed phantom through various steps. In the first we immersed the phantom in a tank full of the dilution of polyvinyl acetate to obtain the waterproofing of the external surface. Due to the complexity of the shapes of the brain, this is followed by steps for filling the various internal compartments to ensure the formation of the vinyl film also on the internal surfaces. After complete drying, the effective waterproofing was verified, making sure that there was no longer passage of liquids towards the outside and between the compartments of the phantom.
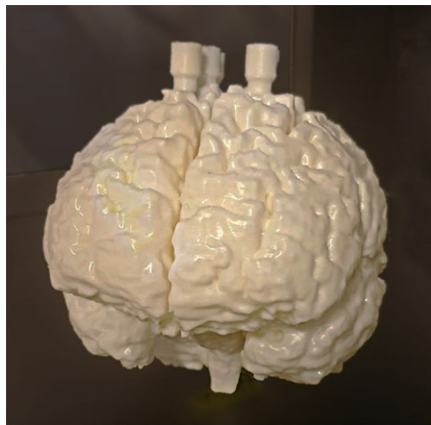
Figure 33 - Prototype of the new brain phantom. The waterproofing process with polyvinyl-acetate led to the creation of the first working prototype. The prototype was printed with the professional 3D printer. Also supplied with it are caps with fittings for filling, which are printed in PET-G or PC using the semi-professional printer.

4.5. Filling System

During the filling of each of the compartments, it is necessary to inhibit the formation of air bubbles, which could generate artifacts with areas of hypo-

intensity in the acquired images. For this reason, we have designed a special filling system for the brain phantom. In the first instance, the phantom is filled by immersing it in a tub full of water. During the immersion, the phantom is moved to facilitate the escape of air bubbles. Subsequently, the filling is completed (at the location where the imaging test takes place) by means of a dedicated filling console which consists of three peristaltic pumps (one for phantom compartment) that connect to the inlet and outlet tubes of the phantom. The console was 3D-printed in PLA using the *RAISE3D N2 Plus* printer and designed in *Tinkercad*® (**Figure 34**). It provides a compartment for the power supply, three compartments for the three pumps and for each of them a small compartment to mount a current intensity regulator. The latter is used to regulate flows and better manage the internal pressures that could be generated in the phantom. Therefore, fillers fixed with specific concentrations of contrast medium or radioisotopes, can circulate for a defined time during the imaging test. It should be noted that for nuclear medicine examinations, pump filling times must be accurately defined to promote diffusion of the radioisotope, while maintaining radiation protection requirements for users.
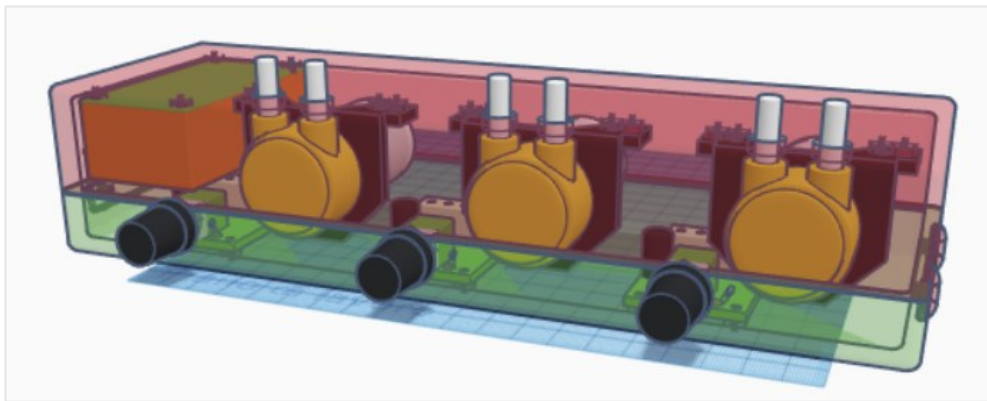
Figure 34 – Phantom filling system. The figure shows the 3D design of the filling console designed for the anthropomorphic brain phantom. The three peristaltic pumps are visible in yellow, with the current regulator (in black) attached. The orange compartment contains the power supply.

The complete filling system is shown in **Figure 35**, where the silicone filling tubes can be identified starting from the console (where they are attached to the pumps) and arriving at the designed caps (**Section 3.3.3.4**). The latter were printed in PET-G and Polycarbonate (PC) using the *RAISE 3D N2 Plus* printer. Both materials have excellent resistance to humidity and water and provide an excellent finishing of the pieces which facilitates screwing.
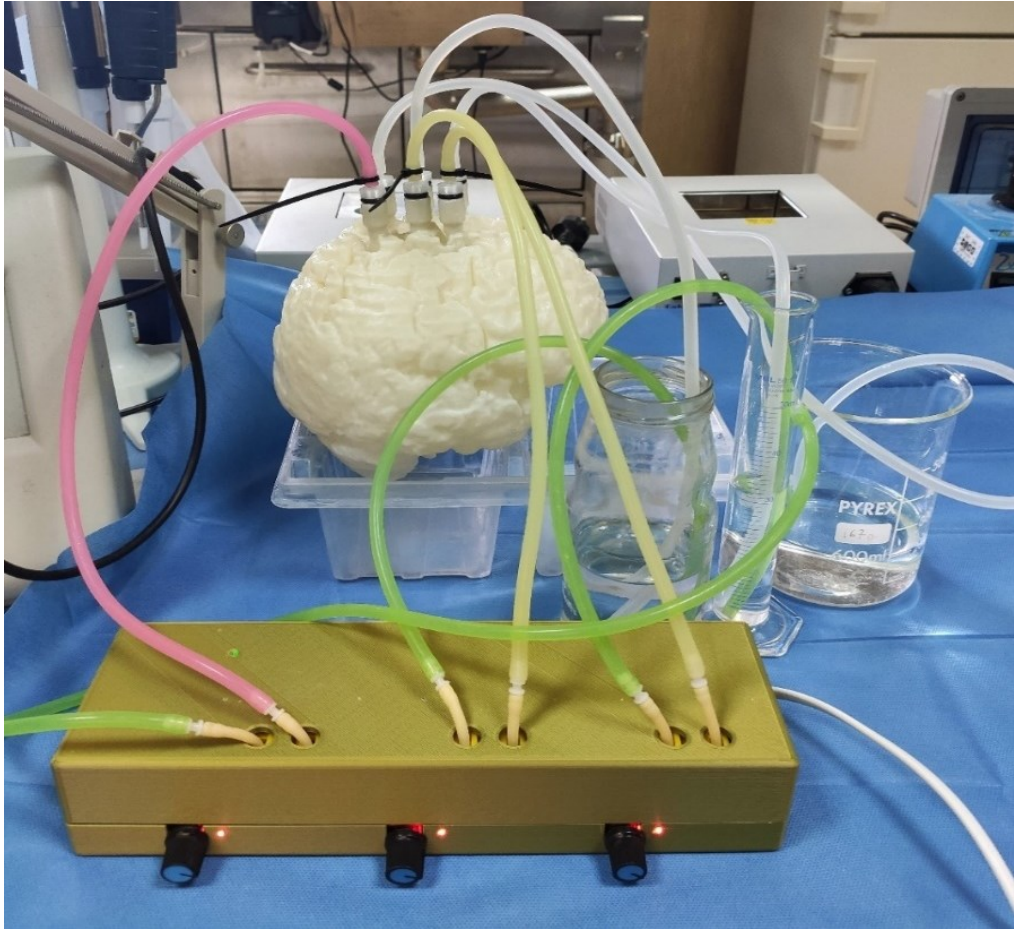
Figure 35 – Filling setup. *The figure shows the configuration used during filling in the radiology department. For each of the three compartments, the appropriate solutions were prepared and inserted in the graduated beakers. The left tube of each pump draws liquids from the beakers. The liquid is then introduced into the phantom compartment via the tube to the right of the pump, connected to the inlet of the phantom. Tubes are connected to the other tube of the phantom for the release of air bubbles.*

4.6. Prototype Scans

The prototype was finally scanned by CT and PET/CT to evaluate the effectiveness of the waterproofing, of the filling system (escape of residual air bubbles and diffusion of the contrast medium/radioisotope in the compartments) and to assess the realism of brain imaging simulation achievable through this device.

The CT scan performed has voxel resolution (x, y, z) equal to $0.446 \times 0.446 \times 0.3$ mm^3 (image size: $512 \times 512 \times 644$). For the simulation, contrast medium concentrations significantly higher than those normally encountered *in vivo* were chosen in order to obtain a signal-to-noise ratio more suitable for the test to validate the absence of diffusion of the contrast medium from one compartment to another. The concentration of the contrast medium in the striatum was

approximately quadruple than the WM one, while in the GM no contrast medium has been inserted. Uniform diffusion of contrast medium into the striatum compartment was achieved by running the corresponding peristaltic pump for 5 minutes, and that of the WM for additional 10 minutes, for a total of 15 minutes. Times were roughly decided based on the volumes of the compartments. **Figure 35** shows the setup of the phantom during filling.

The CT scan showed an unprecedented realism in the simulation of the anatomical shapes of the brain compartments and no diffusion of the contrast medium between the different compartments (**Figure 36**). The phantom walls are also poorly visible on CT imaging despite the high resolution of the imaging modalities. The system for removing air bubbles is certainly much more efficient than in the *STEPBrain* phantom (**Section 2.3.5.3**) and other commercial phantoms, even if it is not yet optimal (there are small areas of hypo-intensity). For this reason, we are experimenting with a solution that involves pre-filling with carbon dioxide.
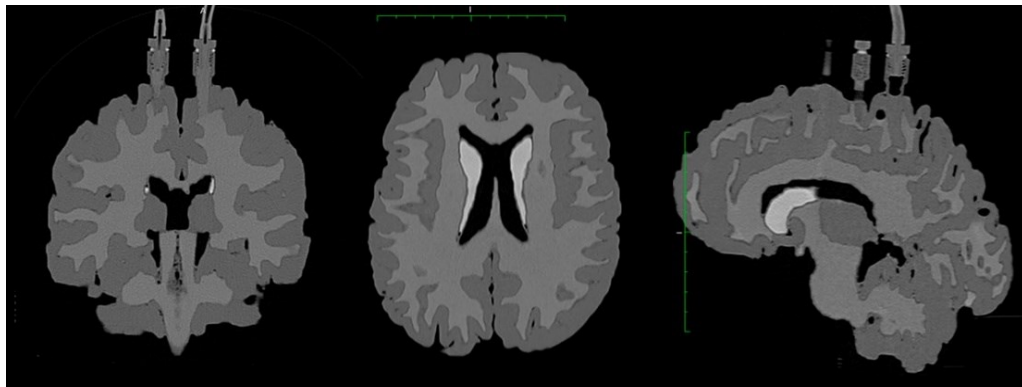
Figure 36 - CT scan with different concentrations of contrast per compartment. The figure shows, from left to right, a coronal, transverse, and sagittal section of the phantom CT scan. For the acquisition, no contrast medium was inserted in the GM, therefore filled only with water. The striatum compartment has a contrast concentration approximately quadruple than WM. The simulation of the anatomy is very realistic, there is no diffusion of contrast medium from one compartment to another (effective waterproofing) and the presence of air bubbles due to filling is considerably reduced.

Finally, we performed a PET/CT scan to assess the realism of the simulation (**Figure 37**). The CT scan performed has voxel resolution (x, y, z) equal to $2\times2\times2$ mm^3 (image size: $128\times128\times90$). At time zero the phantom was taken to the nuclear medicine laboratory for filling with radioisotope ^{18}F-FDG, of which approximately 80 MBq were simultaneously prepared. After that it took about 15 minutes to partition the radiation dose into three parts corresponding to 40 MBq, 6.6 MBq and 4.3 MBq.
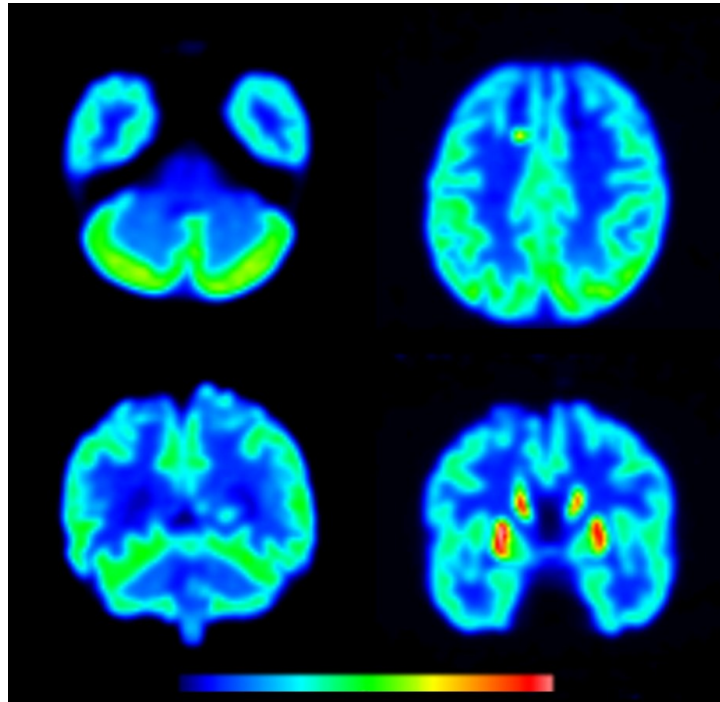
Figure 37 - Test PET/CT scan. *The scan was performed to demonstrate the realism of the PET/CT simulation achievable with the brain phantom. It is possible to notice the difference in radioisotope (^{18}F-FDG) concentration in the three compartments according to the chromatic scale (from 0 corresponding to blue, up to the maximum corresponding to red). The striatum compartment exhibits the highest uptake comparable to that found in PET/CT studies of healthy brains.*

The three doses were prepared in three different shielded containers, one per compartment, respectively, GM, WM, and Striatum. Until the moment of scanning the peristaltic pumps guide the diffusion of the radioactive in the phantom. During that time, the operator can leave the laboratory. After about 30 minutes from the dose entry (50 minutes from time 0), the phantom was placed in the PET/TC scanner for the examination. The realism of the simulation is remarkable. High uptake in the striatum compartment can be noted. In the next simulations, the diffusion of the radioisotope in the GM and WM compartments will be improved by recalibrating the filling times.

Chapter 5

Bases for Future Developments: A New Approach for Multiparametric Brain Segmentation

5.1. Introduction

Image segmentation is the first and most critical step in 3D modelling for 3DP applications. Brain segmentation is commonly used in brain MRI analysis to measure and visualize the brain's anatomical structures, pathological regions, and for surgical planning and image-guided interventions [51]. As discussed in previous chapters, errors can be generated during any stage of the process, including image capture, post-processing, and materialization through 3DP. However, although the accuracy of the source images and the proper choice of printing technology and materials are key to achieving optimum accuracy, image segmentation and STL conversion remain the most error-prone steps [7, 29]. Based on our experience, there are two main factors that may reduce errors at this stage. First, there must always be at least one expert in the field, in our case a neuroradiologist, willing to perform post-processing of the segmented image. This is because segmentation accuracy requires proper recognition of structures and their separation from imaging modality artifacts to ensure that the printed model matches the clinical interpretation of the images. Second, the segmentation software package plays an important role. Although starting from *Phantomag* (**Section 2.3.4.1**) allowed us to (temporarily) get around the segmentation problem to arrive at the *proof-of-concept* of our brain phantom, brain segmentation is the first aspect to be addressed to improve the anatomical rendering of the designed prototype. The *Phantomag* is only a model, which was accurately segmented by authors in a semi-automatic way, since the brain nuclei were defined by hand starting from the segmentation of GM, WM and CSF obtained automatically, but it has limitations related to image resolution, to be overcome in future versions of the physical phantom. As clarified, the supervision of the expert neuroradiologist will always be fundamental in completing the modelling task, but having a brain segmentation software,

dedicated to 3DP, to automatically classify, in addition to GM, WM and CSF, also the brain nuclei (such as caudate nucleus and putamen) in higher resolution brain MRI images (with isotropic voxel, possibly submillimetre), will be equally important for improving our brain phantom and for future brain phantom customizations.

5.2. State of the Art of Brain Segmentation

The advances in brain MRI made it possible to obtain images of ever higher quality standard that can be analysed by clinicians to explore the brain and its pathologies. In the segmentation of MRI images, as implemented for digital or physical phantom generation, each image element (voxel) is assigned a unique value based on the average MRI characteristics present in the tissue corresponding to that voxel [72]. Its dimensions are given by the pixel (in the x-y plane), together with the thickness of the slice (the measure along the third axis). The voxel size determines the spatial resolution or fineness of details that can be distinguished in an image, and varies with imaging parameters, magnet strength, time allowed for acquisition and other factors. Its dimensions along the x-y axes in mm dictates the in-plane spatial resolution. Pixel sizes in clinical MRI typically range from mm (e.g., 1×1 mm^2) to sub-mm. Slice thicknesses in clinical MRI vary from a maximum near 5 mm, achieved using 2D multislice imaging, to sub-mm, achieved with 3D scan techniques [73]. Greater spatial resolution can be achieved with a longer scan time, but this needs to be weighed against the patient's discomfort. In adult brain MRI studies the image acquisition time is approximately 20 minutes, while in paediatric MRI studies the image acquisition time is limited between 5 and 15 min [51].

In the case of normal brain MRI, voxels are typically classified into three main tissue: GM, WM, and CSF; only in more advanced applications are subcortical structures and basal ganglia also segmented separately from GM [74, 75]. Image segmentation can be performed on 2D image sequences or 3D volumetric images. The main difference between 2D and 3D image segmentation is in the processing elements, pixels/voxels, respectively, and their 2D or 3D surroundings on which the image characteristics are calculated. Therefore, 2D image segmentation could contain inconsistencies and non-smooth surface due to the omission of important anatomical information in 3D space. For this reason, in the development of new segmentation algorithms, especially if designed for 3DP applications, it is desirable that it is a 3D segmentation of the volumetric images, so that it is more accurate in 3D space.

5.2.1. Brain Segmentation Methods

In general, brain MRI segmentation is not a trivial task, because the acquired images are imperfect and can often be corrupted by noise and other image artifacts. The diversity of brain imaging applications has led to the development of various techniques for segmentation, but there is no single method that can be suitable for all brain studies acquired with different sequences, nor are all methods equally valid for a particular type of image [51, 72]. It is beyond the scope of this dissertation to discuss them in detail, but, in this section, the most used methods for segmenting brain MRI images are briefly presented to emphasize strengths and weaknesses for 3DP.

5.2.1.1.   Manual Segmentation

In manual brain segmentation, an experienced neuroradiologist manually segments and labels all brain tissues (or just some of interest) across the entire volume of images. This segmentation is typically done *slice-by-slice* for 3D volumetric images. The manual method is believed to be the most accurate due to the expert eye of the neuroradiologist who can accurately and reliably delineate structures in medical images, while the segmentation difficulties are related only to image quality and artifacts. A trained operator usually examines multiple slices for each patient to extract the contours of the affected structures. This procedure is not only tedious, but also particularly error prone, as evaluated by many studies on the intra- or inter-operator variability [76]. Given the resolution improvements achieved by MRI scanners, manual segmentation has become an intense and time-consuming task. Furthermore, the results of manual segmentation are often difficult and even impossible to reproduce, because even experienced operators show significant variability from their previous delineation.

The output data is made up of a series of 2D contours (drawn by the operator on the images through edit tools such as ITK-SNAP [77]) from which a continuous 3D surface can be extracted. This non-trivial post-processing activity is however particularly prone to errors. For example, due to inconsistencies between slices in the segmentation, abnormal bumps in the reconstructed 3D surface are inevitable. Therefore, for models intended for 3DP, manual segmentation is not the most suitable choice, although it is still used extensively to define a surrogate for the "ground truth" of delineation and quantitative evaluation of automated segmentation methods. Furthermore, manual segmentation of different brain structures is considered a fundamental step in the formation of the brain atlas, also used in atlas-based segmentation approaches (**Section 5.2.1.3**).

5.2.1.2. Intensity-based Methods

Intensity-based segmentation methods classify individual pixels/voxels based on their intensity. This allows distinguishing the three main tissue classes (GM, WM and CSF) based on signal intensity, but a more detailed classification is not possible because the intensity profiles of more detailed brain structures overlap [78]. Separating the three main tissue classes based on intensity itself also requires incorporating tools to treat artifacts in MRI (such as intensity inhomogeneity, noise and partial volume effect, as well as overlapping brain and non-brain tissue intensities) [51].

Thresholding. These methods consist of procedures for identifying thresholds on the image intensity histogram to separate the desired classes. Consequently, segmentation is achieved by grouping pixels/voxels between certain thresholds in a class. Generally, these methods are divided into global (single threshold), local (with thresholds chosen based on the position of the voxels on the images), multi-thresholding and adaptive thresholding [79]. Although these are very simple and fast methods, they are very sensitive to noise and inhomogeneity of intensities. Especially on low contrast images, they tend to produce "scattered" groups of voxels, rather than three-dimensionally connected regions. For this reason, although often found on medical image viewing software (even those that extract STL models, such as *3D Slicer*, *Mimics,* and others), they are not suitable for segmentation aimed at 3DP, as they would require a lot of post-processing effort.

Region growing. These methods are used to extract connected regions of the image that consist of groups of pixels/voxels with similar intensities. Generally, they start from the selection of a seed point, which belongs to the brain tissue of interest. In semi-automatic methods the seed is manually selected by the expert user at the beginning of the procedure; in more advanced algorithms, techniques for automatic seed research are proposed [80]. Once a seed is found, the region growing procedures examine all neighbouring pixels/voxels to identify those with similar intensity, according to predefined criteria of uniformity and homogeneity, growing a region around the seed, until no more new voxels are detected to be added. Therefore, region growing methods are suitable for segmenting volumetric images that are composed of large, connected homogeneous regions [81, 82]. The main disadvantage of the region growing methods is the sensitivity to seed point initialization. Especially, in semi-automated procedures, by selecting a different seed point, the result of the segmentation can be completely different. If the seed point and the homogeneity criterion are not defined correctly, the growing region can escape and merge with

the regions that do not belong to the object of interest. Furthermore, these procedures are sensitive to noise. What often happens is that segmented regions in the presence of noise may become disconnected or have holes or separate regions may be connected in the presence of partial volume effects [51, 80]. For these reasons, brain segmentations obtained with these methods would not be sufficiently reproducible and the post-processing effort to obtain segmentation suitable for 3DP would be considerable.

Classification methods. These methods use imaging data with known labels to partition the brain image feature space. Image features are typically brain MRI signal intensity values, which can also be related to texture or other properties of the tissues (such as, geometry or topology). The classification methods are supervised and require a set of training images, which are manually segmented and then used as references for automatic segmentation on a validation set. In addition to manual interaction, another disadvantage of supervised classification methods is that they generally do not take neighbourhood information into account and are therefore sensitive to noise. Furthermore, the use of the same training set for a large number of validation images, and therefore the disproportionate heterogeneity in training brain structures, can lead to distorted results, which fail to take into account the anatomical and physiological variability of the brain between different subjects. The simplest methods are based on the nearest-neighbour classifier, while others very common on the Bayes classifier [83]. A common approach of the first type is based on the k-nearest-neighbour (kNN) classifier to assign each pixel/voxel according to the majority vote of the closest intensity in training data. The kNN is a non-parametric classifier because it makes no assumptions about the statistical structure of the data and is therefore suitable for situations where a very large training set is available [51, 83]. One of the most common parametric classifiers used for brain segmentation is the Bayesian classifier [84]. It models the probabilistic relationships between a set of attributes and the variables of each class, which are then used to estimate the probability of belonging to a class for each unknown variable. In a Bayesian framework, the *a priori* distribution embodies knowledge of probable configurations before an image is observed, the a posteriori distribution is derived after an observation has been made, and conditional probability (also called likelihood) is defined as the probability of obtaining a particular observation given a series of model parameters [85]. These classifiers are used in Expectation Maximization (EM) segmentation methods, successfully implemented in several software packages used in the medical imaging community, such as *SPM* [86], *3DSlicer* [87], *FreeSurfer* [78], and *FAST* [88]. All these methods implement segmentation and bias correction

directly into the EM framework. These methods segment GM and WM with great accuracy, for a variety of applications. To segment subcortical structures, basal nuclei and lesions, especially designed packages are typically added to the general framework.

Clustering methods. These are unsupervised methods to partition brain images into clusters of pixel/voxels with similar intensities without using training sets [89]. In practice, clustering methods use the same data available for the segmentation task to train themselves. Training and segmentation are iteratively done in parallel through two steps: data clustering and estimation of tissue class properties. Among the most commonly used clustering methods are the EM method [90, 91], clustering k-means [91, 92], and the fuzzy C-means clustering methods [93, 94]. The k-means clustering methods are called hard because they force each pixel/voxel to belong exclusively to one class in each iteration, while the fuzzy C-means clustering methods are defined as "soft" because they are based on fuzzy set theory [51, 95]. The EM method has the same "soft" classification principle as the fuzzy C-means, but generally assumes that the MRI intensities of different brain tissues can be represented with a Gaussian mixture model [91]. While clustering methods do not require training images, they do require some parameters to be initialized. Among those mentioned, the EM method showed the highest sensitivity to initialization compared to the fuzzy C-means and k-means clustering methods. As the classification methods, clustering methods do not incorporate spatial proximity information and therefore are sensitive to noise and bias field inhomogeneity. Many extensions of the classical clustering methods have been proposed to improve their performance on noisy images [96-98].

5.2.1.3. Atlas-based Methods

Atlas-based methods are powerful tools for brain MRI segmentation. These approaches are similar to classification methods, except that they are implemented in the spatial domain rather than in the feature space. The main advantage of these methods is the ability to segment any brain structure available in the atlas at no additional cost [51]. An atlas is a model of the human brain for a specific population of interest (infants, children, adults, pathology), which therefore contains information about the anatomy of the brain (for example, information on the location of different brain structures) and is used as a reference (a preliminary knowledge) to segment new images. Before it can be used as a preliminary knowledge, the atlas must be aligned with the image to be segmented. Thus, the segmentation labels and the "ground truth" contained in the atlas are transferred to the target image after registration. As a consequence,

the performance of atlas-based methods is directly dependent on the quality of
the registration method used. Straightforward methods use affine registration;
however, an affine-only alignment may not be sufficient in cases where the brain
anatomy to segment differs significantly from the average anatomy of the atlas.
Therefore, several methods have been developed that aim to overcome affine-
only registration by iteratively refining the segmentation and non-rigid
registration of the probabilistic atlas. A very robust and validated method is the
one developed by Ashburner and Friston [86], included in the SPM software,
which simultaneously performs the non-rigid registration of a probabilistic atlas,
bias field correction and the segmentation of GM, WM and CSF [99]. Even with
non-rigid registration methods, accurate segmentation of smaller and more
complex structures (such as the basal ganglia) remains difficult in general due to
the anatomical variability between different subjects. Atlas-based segmentation
tends to fail on patients with large brain deformities, because probabilistic atlases
are based on populations of healthy subjects [51, 78]. In these cases, an atlas-
based approach is not a suitable method for image segmentation.

5.2.1.4. Surface-based Methods

Those discussed so far are certainly the most widespread brain MRI
segmentation methods, however there are valid alternatives that incorporate
some principles, but are based on the possibility of deforming models with active
contours and surfaces. Deformable models (also called active contours or snakes
in 2D and active surfaces or active balloons in 3D [51]) were conceived in 2D
space [100, 101] and have been further developed and generalized in 3D space
thereafter [102]. These models use closed parametric curves or surfaces to
delineate the region boundaries, which deform under the influence of external
(or image) forces (controlled by image attributes) and internal forces, which
control the regularity of the surface. These models blend the geometric, physical,
and approximate theoretical representation of the brain. Geometry defines the
shape of the object, physics defines constraints on how the shape can vary over
time and space, and theoretical approximation provides mechanisms for fitting
models to measured data. Image forces mainly come from local edge-based
information (for example, based on the intensity gradients of sharp images) in
traditional deformable models [103, 104]. However, this dependence on edge
information makes deformable models sensitive to noise and highly dependent
on the initial estimate. Significant efforts have been made to integrate more
global region information into deformable models [105-107].

5.2.1.5. Hybrid Methods

In recent years, new methods are continually being explored and introduced to address the emerging application-specific segmentation problems of brain MRI. However, selecting the most appropriate technique for a given application is often a difficult task, and a combination of different techniques may be required to achieve the specific segmentation goal. Following this trend, new hybrid or combined segmentation methods have already been proposed and used in different brain MRI segmentation applications [108]. The main idea of these approaches is to revisit and combine several complementary segmentation methods into a hybrid approach, which aims to avoid many of the disadvantages of single segmentation methods to improve segmentation accuracy [98, 109, 110]. Generally, these algorithms tend to combine classic iterations of classification methods with elastic registration steps to align a normal brain anatomy model to the patient's tissues. In other cases, multimodal methods are proposed, or still others based on artificial neural networks (ANN), which, however, can only be used when there is a greater availability of data, in particular, different MRI scans for multimodal methods (also called multiparametric), and large training sets of images for ANN-based methods [108, 111]. These methods have the drawback of being more complex than any single method integrated into a hybrid one, thus also leading to a greater number of different parameters that need to be adjusted for a specific application. Therefore, a hybrid segmentation method should always be carefully and wisely designed to provide efficient, good quality segmentation in a reasonable time.

5.2.2. Multiparametric Segmentation Based on Relaxometry

In presenting the various segmentation methods, we generally referred to the intensities of brain tissue in the magnetic resonance (MR) images. In the previous chapters, we also referred to the T1 and T2 relaxation times, the respective R1 and R2 relaxation rates, and T1-, T2- and PD-weighted (T1w, T2w, PDw) magnetic resonance images. For the sake of clarity, it is useful to briefly review the well-known physical principles of magnetic resonance to define what is the relative intensity of the tissue signal in an MR image and to orientate among the various possible magnetic resonance maps that can be produced by changing the acquisition sequences. The same concepts are useful for describing the principles of relaxometry and the segmentation method discussed in **Section 5.3**.

5.2.2.1.   Basics of Brain MRI

MR uses magnetic fields and radio waves to produce thin-layer images of tissues (tomographic images). The hydrogen protons (commonly called spin) contained within the tissues rotate, generating small magnetic fields that are initially aligned randomly. Once they are "inserted" into the strong magnetic field of MRI (1T, 1.5T or 3T), their magnetic axis aligns along that field. Subsequently, the application of a radiofrequency pulse causes the axis of many protons to align momentarily in the opposite direction with respect to the field, in a condition of high energy. After the pulse, the protons relax and resume their original alignment in the magnetic field of MRI. The magnitude and speed of the energy release, that occurs with the return to basal alignment of the protons (T1 longitudinal relaxation time or lattice-spin relaxation), and their oscillation (precession) during the release of energy (T2 transverse relaxation time or spin-spin relaxation) are recorded as spatially localized signal intensity from a coil (antenna) inside the RM device. Computer algorithms, based on Fourier transformation, analyze these signals, and produce the detailed anatomical images converting the frequency information contained in the signal from each location in the slice to corresponding intensity levels. These levels are then displayed as shades of grey in a matrix arrangement of pixels. The magnetic signal intensity (brightness) of tissues in an MR image is therefore determined by different factors, the main ones being:

- Proton density (PD) of the different tissues;
- Local magnetic field inhomogeneities;
- T1 and T2 intrinsic characteristics of the different tissues;
- Radiofrequency pulses and gradients used to obtain the image.

By controlling the radiofrequency pulses and the oscillations of the gradient, it is possible to obtain images with different sensitivity to the different (T1 and T2) relaxation rates, thus having different signal intensities in different tissues. Computer programs embedded in MR devices produce specific pulse sequences varying, for example, the Repetition Time (TR) and the Echo Time (TE), that influence how the image is obtained (weighted) and how different tissues appear. TR is the time between successive pulse sequences applied to the same slice, while TE is the time between the delivery of the RF pulse and the receipt of the echo signal (produced by the return to coherence in phase of the spins after a time T2). Each brain tissue is characterized by the two different relaxation times T1 and T2. The first is the time constant which determines the rate at which the excited protons return to equilibrium. It is a measure of the time it takes for the spinning protons to realign with the external magnetic field. The second is the

time constant which determines the rate at which excited protons reach equilibrium or go out of phase with each other. It is a measure of the time it takes for the rotating protons to lose phase coherence between the spins rotating perpendicular to the main field. For one of the most widely used families of MRI sequences, called Spin-echo sequences, images can be weighted in T1, T2 or PD. T1w images are obtained with short TE and TR times, in this way the contrast and brightness of voxels are predominately determined by T1 properties of tissue. T2w images are obtained with longer TE and TR times, thus in these images, the contrast and brightness are predominately determined by T2 properties of tissue. T1w and T2w images can be easily differentiated by looking to CSF, because water and liquids appear relatively dark (hypointense) on T1w images and bright (hyperintense) on T2w images (as in the CSF area of the ventricles indicated by the red arrow on the T2w image of **Figure 38**).
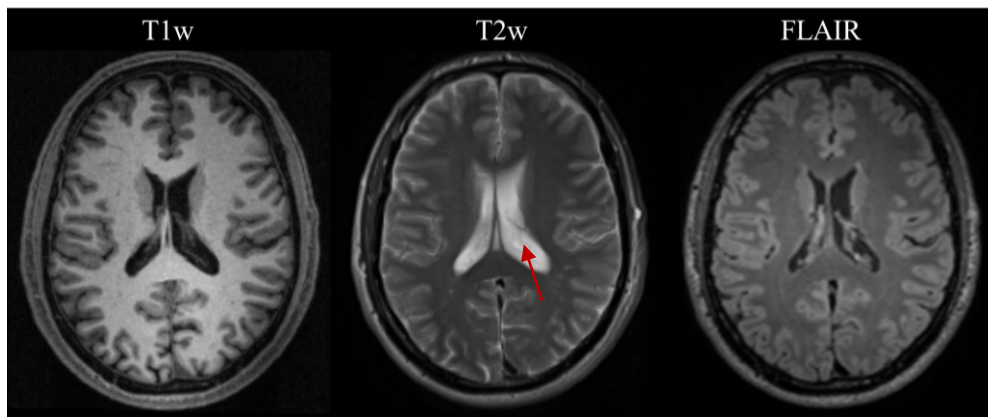
Figure 38 – T1-weighted, T2-weighted and FLAIR brain MRI image. The figure shows T1w, T2w and FLAIR images of a selected slice from an MRI study of a healthy subject. By comparing the images, it can be seen that CSF (red arrow) appears dark in T1w, bright in T2w and dark in FLAIR. The cortex (GM) appears grey in T1w, light grey in T2w and FLAIR. The WM appears light in T1w, dark grey in T2w and FLAIR.

Furthermore, fat appears bright on T1w images and relatively dark on T2w images. Generally, T1w images optimally show normal soft-tissue and adipose tissue anatomy (e.g., to confirm the fat component of a mass). T2w images optimally show fluid and pathological conditions (e.g., brain tumors, demyelinated regions, inflammation, trauma) [112]. Another sequence, commonly used in clinical studies, is the Fluid Attenuated Inversion Recovery (FLAIR) [113], which is similar to a T2w image, but obtained with the addition of an inversion pre-pulse to null fluids in the images. In this way, pathological areas (such as multiple sclerosis lesions, meningitis, lacunar infarction, brain lacerations due to head trauma) remain bright, while the normal CSF signal is attenuated and dark in FLAIR images. Finally, PDw images are obtained using

a long TR and a short TE. In brain images, this sequence allows for a more
marked distinction between GM (lighter) and WM (dark gray), but with little
contrast between brain and CSF.

Hence, the T1w, T2w, PDw and FLAIR images provide complementary
information, which can be very important in the characterization, not only of
healthy tissues, but also of pathologies. Multi-contrast magnetic resonance and
multiparametric automatic segmentation methods are, for this reason, widely
used for quantitative measurements on large patient cohorts for the evaluation of
normal and abnormal intracranial tissues.

5.2.2.2.   Basics of MRI Relaxometry

Relaxation times reflect changes in tissue density of chemical composition.
Among the possible quantitative measurements, the calculation of the time
constants/relaxation rate of the water proton (e.g., relaxometry) is considered
capable of providing objective measures relating to the tissue properties, adding
sensitivity to conventional MRI scans, and detecting abnormalities not
necessarily observable on T1w, T2w and PDw images. Relaxometry represents
a group of quantitative MRI techniques which measure relaxation variables
directly adherent to the biological properties of the tissue, such as T1, T2 or their
reciprocals [114, 115]. In this regard, it is well known that the longitudinal
relaxation rate (spin-lattice) (R1 = 1/T1), the transverse relaxation rate (spin-
spin) (R2 = 1/T2) and the proton density (PD) depend on the local physical and
chemical properties of the tissues in a complex way, also reflecting the molecular
constituents of the different microenvironments [116]. In addition to objective
quantitative measurements of tissue properties, it is possible to obtain maps
representing relaxation parameters derived from MRI, which allow detecting
diffuse changes throughout the brain [117, 118]. These parameters provide an
absolute scale, independent of MR scanner settings and imperfections (i.e.,
differences in coil sensitivity or field inhomogeneity). Intensity of brain tissues
is certainly one of the most important characteristics for brain segmentation,
however, when values are corrupted by artifacts (such as noise, partial volume
effect, field inhomogeneity), intensity-based segmentation methods can lead to
incorrect results [119, 120]. The maps of the relaxation parameters, on the other
hand, provide consistent images relatively free of the imperfections due to the
variation of the scanner gain on the intensity of the signal obtained at different
times and/or on different subjects. Brain relaxometry thus provides in principle
a means of identifying the tissue composition of brain voxels, potentially
enabling the segmentation of different brain tissues based on their specific
relaxation parameters (i.e., R1, R2, PD). These quantitative maps of relaxation

parameters, spin-echo could be obtained through Conventional Spin-Echo (CSE) sequences, which represented the mainstay of early MRI studies [121].
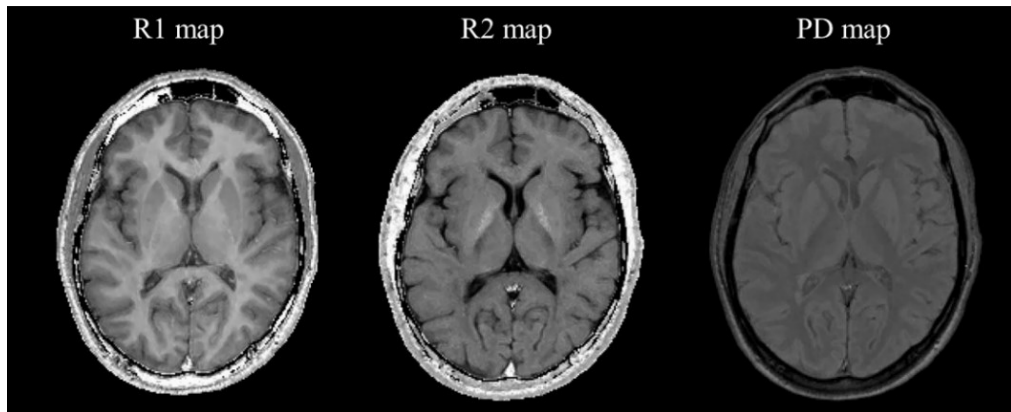
Figure 39 - R1, R2, PD maps of the brain. *The figure shows for a selected slice the maps R1, R2 and PD of the brain of a normal subject obtained from the data acquired by conventional spin-echo.*

5.2.2.3. Quantitative Magnetic Color Imaging (QMCI)

Full-colour representation approaches are frequently used to enhance contrast and to mediate the diagnostic interpretation through chromatic scales [117, 122, 123]. The combination of three monochromatic colour scales represents the best possibility of providing integrated information from multiple parameters, because we have three different colour receptors in the cones of retina (one for red, one for green and one for blue). This is helpful to easily distinguish different tissues that may be displayed with the same grey level on CSE images [117]. Quantitative magnetic color imaging (QMCI) is a multi-parameteric representation of MR data that combines relaxation parameters' maps into single color images, representing a global display of spin-echo information. In this representation, three linear monochromatic (red – R, green – G, and blue – B) scales are used to simultaneously display three relaxation parameters (R1, R2, PD) with a full-color approach [117]. The encoding of the R1, R2, PD maps as RGB, respectively, was selected to have a "pseudo-natural" representation of the brain structures that would provide the best results in terms of anatomical and diagnostic information (**Figure 40**).

Moreover, the same scale is efficient in representing different brain tissues diseases. In practice, the use of hybrid color maps can overcome the intrinsic limitation of the images depending on the signal intensity, on which the opposite effects of T1 and T2, depending on the selected spin-echo sequence parameters, could decrease or even eliminate the contrast between two different structures.

QMCI images therefore provide an enhanced tool for visualizing brain tissues, potentially useful for segmentation.
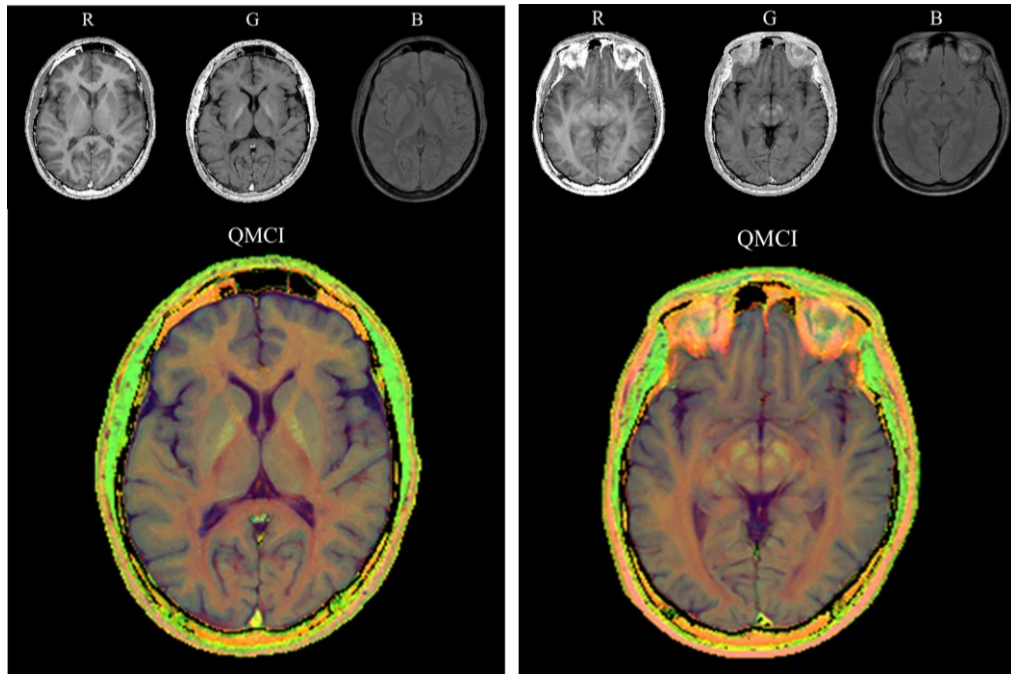
Figure 40 – QMCI derived from conventional spin-echo MRI scans. *Maps R1, R2 and PD, shown here as R (red), G (green), and B (blue), respectively, are combined to form the three channels of the colour QMCI image. In the QMCI images it is possible to distinguish the different brain structures by colours. GM appears in a greyish colour, while WM appears in salmon colour. The basal ganglia (pallidus, red nucleus, nigra and dentate nucleus) appearing in a bright green colour. The bright green is due to the brightness of these tissues in the R2 map (corresponding to green), which in turn is due to the high iron content of these tissues.*

5.2.2.4.   Multiparametric Segmentation Based on QMCI

There are many intensity-based techniques that use a multi-contrast approach to classify the voxels of brain MRI images. These approaches try to combine the intensity information of the brain tissues contained in multiple MRI acquisitions of the same subject, having different contrast, to obtain more features for each tissue. However, segmentation algorithms based on signal intensity require operator intervention at different levels [119, 124], and even those that propose a fully automated solution do not exactly segment brain structures, but only the three main compartments (GM, WM, and CSF). The maps of physical parameters of MR (R1, R2, PD) instead provide a standardized approach for the evaluation of MRI data. Indeed, unlike the intensity signal maps, the calculated relaxation rate maps provide a reproducible position of the voxel clusters of brain tissues in a multi-parametric space (**Figure 41**).
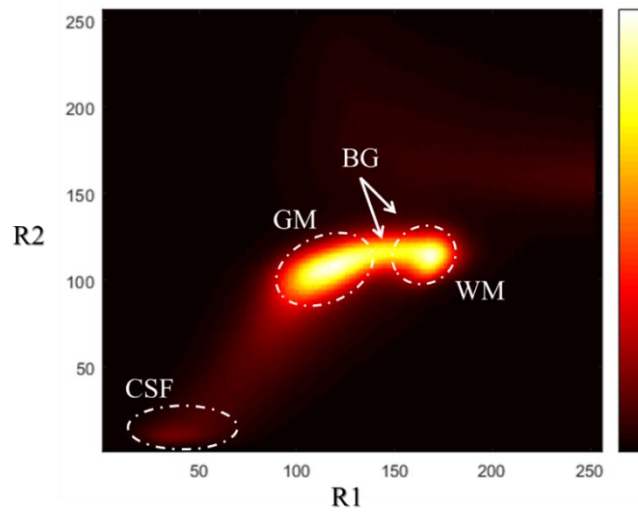
*Figure 41 – Two-dimensional distribution of voxels in the R1-R2 plane. The distribution shown was
derived from the segmentations of 37 CSE studies of normal volunteer subjects, segmented by the multi-
parametric segmentation software presented by Alfano et al [119]. The regions circled in the R1-R2 plane
identify the distribution of GM, WM, and CSF voxels in the plane. The density of GM and WM clusters
hides the basal ganglia clusters that are in the areas indicated by the arrows.*

Therefore, the distribution of the pixels in the space of the features R1, R2, PD,
allows separating a greater number of tissue components than the distribution of
the pixel in the intensity space of the T1w, T2w and PDw signals. The
preliminary calculation of parametric maps in a segmentation algorithm thus
overcomes problems created by the variable gain of an MR system on the signal
intensity obtained at different times on different subjects. For this reason,
relaxation parameter maps calculated on the basis of CSE images have been used
in the past, with considerable success, as an intermediate step for
multiparametric segmentation of brain tissues, based on their characteristic
relaxation parameters (R1, R2, PD), in normal subjects and patients with
neurodegenerative diseases (such as multiple sclerosis and Alzheimer's disease)
[119, 120, 124]. These approaches have long avoided the need to adopt
additional and dedicated sequences for segmentation purposes, obtaining the
parametric maps from pre-existing conventional sequences, and providing
simultaneous segmentation for both lesions and other brain tissues. Historically,
CSEs were the first sequences largely used in clinical MRI studies, but to date,
due to the long acquisition times, they are no longer suitable for clinical practice
[125]. Therefore, although there was a reasonable advantage in using relaxation
parameter maps for segmentation, without the spin-echo data provided by CSEs
it is no longer possible to derive them. Some authors have proposed new faster
acquisition sequences to obtain maps of R1, R2, and PD of the brain, but to date
they are used only for specific applications [118, 124]. Brain images obtained
through routine clinical MRI protocols (3D-GrE T1w, FLAIR and fast-T2w

sequences with ≤ 3 mm slice thickness) [126] are currently the most widespread
and provide optimal spatial and contrast resolution.

5.3. New Brain Segmentation Approach

As discussed, the spin-echo data that can in principle be obtained through CSE
sequences allow calculating the quantitative maps of the relaxation parameters
(we refer to R1, R2, PD). These provide a means of identifying the tissue
composition of brain voxels, potentially allowing the segmentation of different
brain tissues based on their specific relaxation parameters. In the past, maps of
R1, R2 and PD calculated from post-processing of CSE images have been used
as an intermediate step to segment normal and abnormal brain tissues, based on
their characteristic relaxation rates, in normal subjects, and patients with
neurodegenerative pathologies, through multi-parametric segmentation methods
[127]. Over time, faster sequences (e.g. TSE) and 3D (e.g. MPRAGE, 3D-TFE),
as well as sequences with improved sensitivity to pathological changes (e.g.
FLAIR), have progressively replaced CSE in routine clinical practice [125].
Therefore, the analytical approach to calculating relaxation rates based on
equations of state, previously used for CSE, cannot be translated into the new
scenario, unless new techniques are developed to calculate relaxation rate maps
from dedicated sequences, which must however, be acquired specifically for this
purpose [124, 128, 129], as they cannot be applied *a posteriori* on previously
acquired clinical studies.

5.3.1.   Pseudo-relaxation Parameter Maps Generation

We developed a polynomial regression-based approach for generating pseudo-
relaxation parameter maps to fill the lack of spin-echo data among those of
current clinical practice. We showed that it is possible to estimate a function that
correlates the signal intensities of the voxels in the MRI images obtained from a
set of heterogeneous sequences (at least one T1w, T2w and one FLAIR image),
with the R1, R2 and PD values of the same voxels, provided that both the signal
intensity and the relaxation rates are known for a considerable portion of the
voxels. The procedure was entirely developed in *Matlab® (R2018b)*.

5.3.1.1.   *A priori* Knowledge of Brain Relaxation Parameters

To obtain the predictive model to estimate the maps of the pseudo-relaxation
parameters of patients through our polynomial regression-based approach, *a
priori* knowledge of R1, R2 and PD values under normal conditions, valid for
the whole range of brain tissue relaxation rates and signal intensity values, was

necessary. This information was taken from the MRI digital phantom of the normal brain presented in the **Section 2.3.4.1**, *Phantomag*. The digital phantom was then used as a model for the extraction of *a priori* information on the properties of normal brain tissues in the space of the dependent variables R1, R2 and PD. The values of the relaxation parameters of the phantom intracranial voxels, which are derived from a single subject, were preliminarily adjusted to match the distribution to the mean distribution derived from a CSE dataset of normal volunteer subjects. To this end, the four-dimensional histogram (4D) in the relaxation parameters space (R1, R2, PD) of the digital phantom was co-registered by affine transformation in this space (maximizing the objective function given by the product of two histograms) to match the corresponding histogram obtained from normal tissues of all CSE studies. As seen, this digital phantom also provides a QMCI representation (**Section 5.2.2.3**), which was useful for qualitative comparison with the same obtained from the simulated maps of the patients' relaxation parameters.

5.3.1.2. Spatial Normalization

Brain normalization is an important registration step in multi-subject (group) whole-brain analyses that allows establishing spatial correspondence between brains of different subjects. Normalization of the brain is usually done by deforming each brain into a common space. The most used standard spaces for normalization are the Talairach space and the closely related Montreal Neurological Institute (MNI) template space [130, 131]. After normalization, a point in the common space (identified by its x, y, z coordinates) is assumed to refer to a similar region in any brain normalized in the same space. This image registration step is necessary and functional for the choice of data points for polynomial regression. In our procedure, spatial normalization is carried out using the dedicated module of the Statistical Parametric Mapping software (SPM12). The digital phantom and patient study (to be segmented) are normalized to be referenced in the standard MNI brain space. Since the MRI signal intensity maps of the patient studies are affected by spatially smooth intensity non-uniformities (also known as "bias") due to the inhomogeneity of the magnetic field, which would lead to segmentation errors, the SPM12 normalization procedure preliminary debiased them. After that, it calculates non-linear deformation field which estimates the best overlap between the probability atlas of the brain tissues and the image of the individual subjects. The atlas contains six average-shaped Tissue Probability Maps (TPM) of all various brain tissues (**Figure 42**), which encode the anatomical variability observed within a population of 368 healthy adults for neural and non-neural tissue types [132,

133]. Normalized images are brought to isotropic voxels of dimension 1×1×1 mm^3 and the same dimensions as the corresponding template (matrix 181×217×181). Patient studies are brought into the MNI space by 4-*th* degree B-Spline interpolation. The digital phantom and its tissues are instead interpolated using an interpolation of the nearest neighbour in order not to invalidate the pre-existing tissue classification of the model in its physical space. The latter provides the priors for the R1, R2 and PD maps to be correlated with the T1w, T2w and FLAIR signals of the patient studies by polynomial fit.
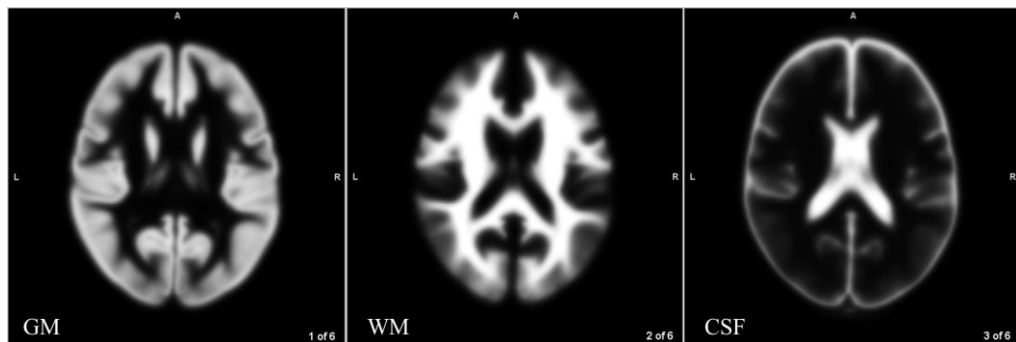
Figure 42 - Tissue probability maps of GM, WM and CSF. The figure shows the TPM used for GM, WM, and CSF. They encode the anatomical variability observed in a population of 368 healthy adult subjects.

5.3.1.3.   Skull Stripping

MRI devices provide 3D head volumetric scans that include brain and non-brain tissues, also referred to as intra and extra cranial tissues. Skull stripping is a common preliminary processing step in neuroimaging studies to isolate brain tissues from non-brain tissues (i.e., skin, fat, muscle, vitreous humour, dura, and skull). For brain MRI analyses, it is preferable to preliminarily remove non-brain tissue from the images before applying any other image processing algorithms. Hence, also for the choice of data points for polynomial fitting to estimate the predictive model of patients' brains R1, R2 and PD maps. Given the importance of this task for neuroimaging studies, a wide range of automated skull stripping methods exist in the literature, but none of them is failproof [134]. Common skull stripping techniques are mono-parametric (i.e., optimized for one sequence at a time). Most skull stripping methods were designed for T1w brain images only and since the appearance of brain images can vary significantly between scans, this complicates the task of devising an efficient skull stripping method that works through sequences and scanners. Therefore, existing skull stripping methods often need to be adapted specifically for a certain type of study or, at best, adapted to work on a specific population. Even the most commonly used methods, such as the Brain Surface Extractor (BSE) [92] and the Brain

Extraction Tool (BET) [135], may fail in the exact extrapolation of intracranial voxels (ICV) leading to unacceptable errors in segmentation. In our case, having available images obtained with different acquisition sequences (a fast T1w, a fast T2w and a FLAIR), we chose to mix the information contained in each acquisition and use the resulting images as a starting point for the extraction of the ICV. For the specific task, our algorithm works on the images obtained by adding the intensities in the T2w volume to those of the T1w volume with weight factors for the combination of the images defined automatically to have a flat image on GM and WM (the distribution of the sum of the weighted intensities is made a single gaussian-like bell). In the resulting volume, all voxels corresponding to the low density of protons appear "blackened", defining a darker demarcation region between the brain and non-brain tissue (**Figure 43**). A specific threshold is applied to this volume, defined by an automatic procedure, to mask the most intense regions on which subsequent erosions are performed to separate the extracranial from the intracranial voxel residues.
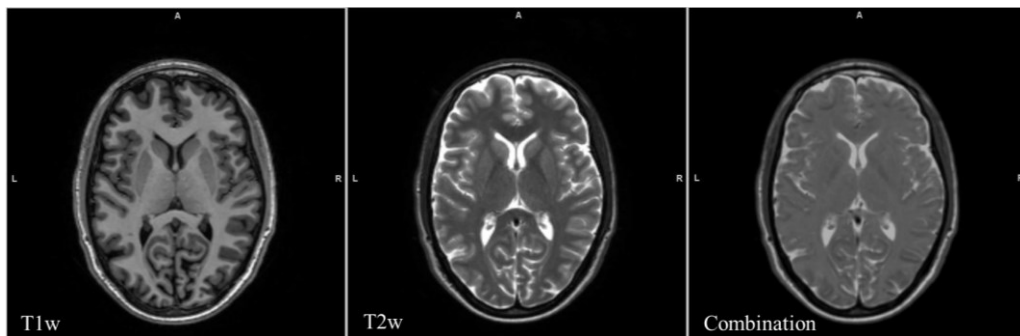
Figure 43 - T1w, T2w and combination for skull stripping. *The figure shows a section of the T1w and T2w volumes, and the same slice of the volume obtained by the automated combination of the two, calculated for skull stripping. As can be seen in the combined image, the difference in contrast between GM and WM is practically cancelled. This aspect is functional to the selection of a first cluster of ICV which during the skull-stripping procedure is then increased by adding the CSF voxels which are at higher intensity, without breaking the boundary between intracranial and extracranial tissues.*

These operations result in a main cluster of intracranial tissues which is then expanded with conditional logic to recover all the voxels of the CSF on T2w and those on the border between CSF, GM and a first layer of surrounding low proton density tissues. The automated multi-parametric intensity-based skull-stripping method was found to be robust and efficient, providing the best solution for the sequences used in this work (**Figure 44**). The procedure has also been successfully tested on cerebral magnetic resonance imaging of infants and children, including those with brain pathologies.
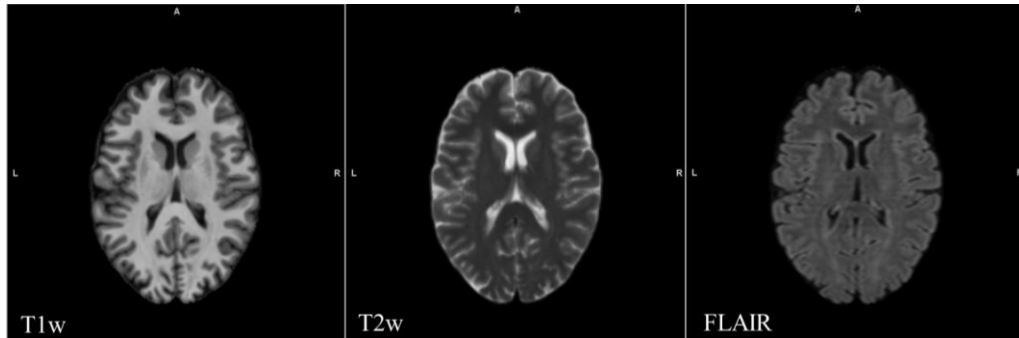
Figure 44 – Results of skull stripping on a healthy subject. *The figure shows a T1w section, a T2w section
and a FLAIR of a healthy subject on which the described skull-stripping procedure was applied.*

For the digital phantom, the segmentation of extracranial tissues is also available,
therefore, for it was sufficient to eliminate the voxels classified as extracranial
tissue in the classification made by the experts (**Figure 45**).
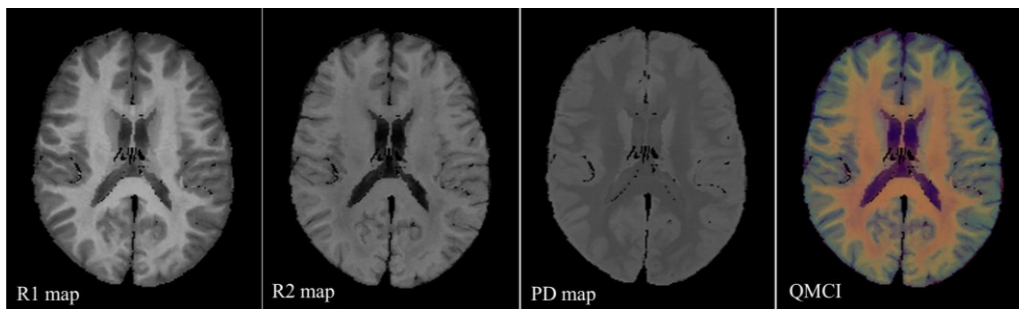
Figure 45 – Digital phantom skull-stripping. *Skull-stripping is also applied on the digital phantom for the
need to create a correspondence between the voxels of potentially the same tissue in the model and in the
patient.*

5.3.1.4.   Estimation of Pseudo-relaxation Parameter Maps

The developed polynomial regression approach aims to derive from patient data
(signal intensity in T1w, FLAIR and T2w acquisitions) and implicit information
(pseudo-R1, -R2, -PD maps). To this end, for both independent and dependent
variables, the corresponding observation points are selected from the patient's
magnetic resonance and from the model (*a priori* knowledge, **Section 5.3.1.1**),
to apply the polynomial regression algorithm. After spatial normalization and
skull stripping, data points for polynomial fit are extracted by selecting the
voxels of the MRI images with a higher probability of belonging to the same
tissue on both the patient and the digital phantom. The step-by-step procedure to
obtain a predictive model of the patient's intracranial relaxation parameters from
T1w, FLAIR and T2w fast sequences is described below.

Brain tissue selection. The spatial normalization procedure re-establishes an anatomical correspondence of the brain structures, but variations in the shape, volume and thickness of the cerebral cortex remain among the different subjects, as well as different sulcal patterns and misalignments in the boundaries of the brain tissues. A first step to ensure the goodness of the final fit is the extraction of groups of points from the MRI images, which are representative observations of all major brain tissues. Therefore, only the voxels most likely belonging to major brain tissues (named as potential GM, WM, and CSF at this stage) are extracted from the normalized MRI images, avoiding those at the interface between tissues that are most likely to mismatch in the subject and in the digital phantom. First, the digital phantom is eroded by one voxel (inward for each tissue) to erase all boundary voxels between different tissues, which presumably contain "mixed" information about the two neighbouring tissues, and not "pure" information of a single tissue. Then, for the selection of brain tissue voxels the software exploits the information on the spatial distribution of the tissues contained in the digital phantom on the one hand and in the TPM on the other. The latter express the Bayesian a priori probability that any voxel in the MNI space belongs to a class of tissues (GM, WM, CSF, soft tissue, skull and air). Subsequently, only voxels above predefined thresholds on the GM, WM or CSF TPM are selected. Furthermore, only voxels classified in the same tissue in both the binarized TPM and the eroded digital phantom are accepted as the first set of possible data points. The choice of thresholds modifies the attribution of correspondence by voxel between neighbouring tissues in the polynomial fit. Since the behaviour of the fit curve at the point of separation between GM/WM and GM/CSF is critical, an optimization is performed to select voxels from each GM, WM, and CSF area in the brain, to have almost the same proportion of volumes voxels collected for GM, WM, and CSF tissues. Note, the need to extract points for each brain tissue from all areas of the brain, as the tissues do not have the same signal intensity over the entire visual field, both for physiological reasons and for the effect of the inhomogeneity of the residual field on MRI images.

Balancing of observations distribution. The problem of unbalanced domains often occurs in the context of predictive tasks, where a set of data is considered unbalanced if groups (or classes) are not approximately equally represented [136]. In unbalanced scenarios, the distribution of observations is skewed, since representatives of some groups appear much more frequently, and therefore the predictive model is skewed towards majority groups. The effect of unbalanced datasets on prediction has been studied mainly in the context of classification tasks, where the predicted target variables are nominal, but less so in the context

of regression, where the target variables are continuous [137, 138]. Pre-
processing strategies to collect observation data points, such as the one discussed
so far, are useful and necessary, but often not sufficient to overcome this
problem. Also, in regression, the continuous nature of target variables adds
complexity because there are a potentially infinite number of values to manage.
In general, in this context the specification of the more/less relevant values of
the target is not easy [137], while, for our application, having a pre-segmentation
of the chosen points (through the digital phantom and TPM), it was easier to
explore the points to discover their imbalance. Obviously, looking at the mask
of the selected voxels, we were faced with a scenario that could change from
patient to patient. The points selected as potentially belonging to GM, WM, CSF,
and other tissues were always in the same quantity, because they were selected
with thresholds on the TPM. Therefore, in order not to distort the data, but simply
to want to balance them, a simple method at the data level [138] was used to
under-sample the majority groups of GM and WM to obtain a good
representation in the fitting also of basal ganglia. These are naturally small and
therefore consist of very few voxels. Random subsampling is achieved by
eliminating the GM and WM voxels from the mask to reduce the number of
voxels to approximately ¼ of the initial amount, alternately eliminating
transverse and coronal slices to maintain GM and WM voxels from all brain
regions.

Predictive model evaluation. The voxels of the model of the relaxation
parameters of normal brain tissues (digital phantom) are thus coupled by position
to those of the patient's T1w, T2w and FLAIR images. The information about
the intensities of the paired voxels is used as input for a multiple and multivariate
linear polynomial regression model (hereinafter also referred to as the predictive
model). In particular, the "predictors" for polynomial fit are the intensity values
of the brain tissue voxels that describe the patient's MRI signals in the T1w,
FLAIR and T2w sequences, while the "predicted" (dependent) variables are the
values of the corresponding voxels on the resulting R1, R2 and PD simulation
maps. The regression model chosen is multiple, since it has more than one
independent variable (predictors) in a formula; multivariate, since it has more
than one dependent variable in different formulas; linear, since the
coefficients/weights associated with the characteristics are still linear; and
polynomial, since the nonlinear model is a polynomial formula of n-*th* degree
[139, 140]. For each patient 3 predictive models are extracted (one for R1, one
for R2 and one for PD) using an extension of the polynomial curve fitting
function (*polyfit*) of *Matlab® (R2018b)*, called *polyfitn [141],* and displayed as
QMCI images for visual evaluation. Polynomial fit using 4-*th* or 5-*th* degree

polynomials produces a clearer definition of the basal ganglia and clearer boundaries between GM and WM in the pseudo-QMCI, compared to 2-*nd* and 3-*rd* degree polynomial fit. Since in some cases overfitting artifacts become evident in the basal ganglia (**Figure 46**) when using 5-*th* degree polynomial interpolation (a rather predictable behaviour, considering the limited number of voxels available for these small structures), the 4-*th* polynomial regression is generally the best for the studies done so far.
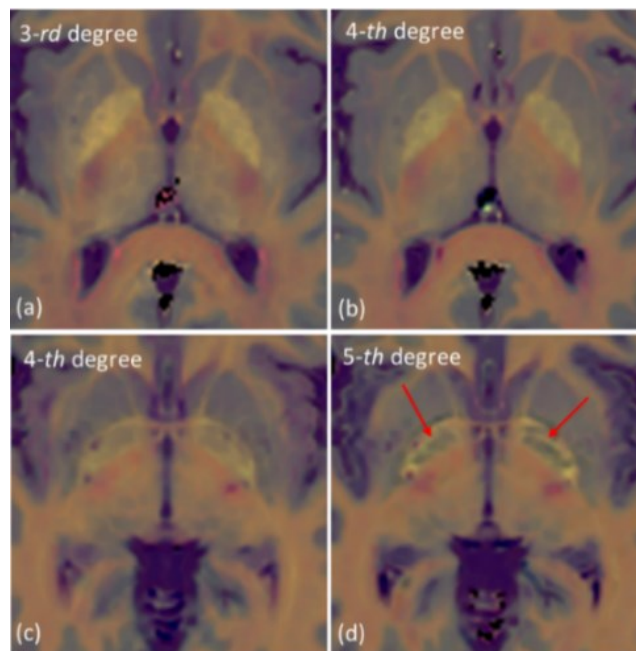
Figure 46 - Improved definition of basal ganglia with the 4-th degree of polynomial regression. Figures (a) and (b) are magnifications of the 3-rd and 4-th degree pseudo-QMCI images; (c) and (d) are enlargements of the 4-th and 5-th degree pseudo-QMCI images of another patient, showing abnormal pseudo-relaxation rates in the globus pallidus (indicated by the red arrows) due to overfitting.

Pseudo-relaxation parameter maps calculation. For each clinical study, the three sequences are preliminarily co-registered in the patient space using the automatic rigid body co-registration routine available in SPM12 and then interpolated to have an isotropic voxel of $1\times1\times1$ mm^3. For co-registration, SPM12 default parameters and normalized reciprocal information can be left as an objective function. The three predictive models obtained in the previous step are then applied to the co-registered MRI volumes to calculate the pseudo-R1, -R2 and -PD maps in the original patient space. MRI volumes are also colour coded to obtain patient pseudo-QMCI for visual assessment of image quality (**Figure 47**).

5.3.2.   Segmentation

The developed segmentation approach takes advantage of QMCI features (R1, R2 and PD) to segment brain images. It can segment both the studies obtained by CSE and those obtained with the fast MRI sequences of today's clinical practice, through the pseudo-QMCI maps' calculation process illustrated in the previous **Section 5.3.1**. The software works on isotropic (or "almost isotropic") voxel images, so the patient's QMCI or pseudo-QMCI (which we will refer to directly as QMCI) are interpolated in advance to have, as already mentioned, isotropic voxels equal to $1\times1\times1$ mm^3. The software aims to segment most of the
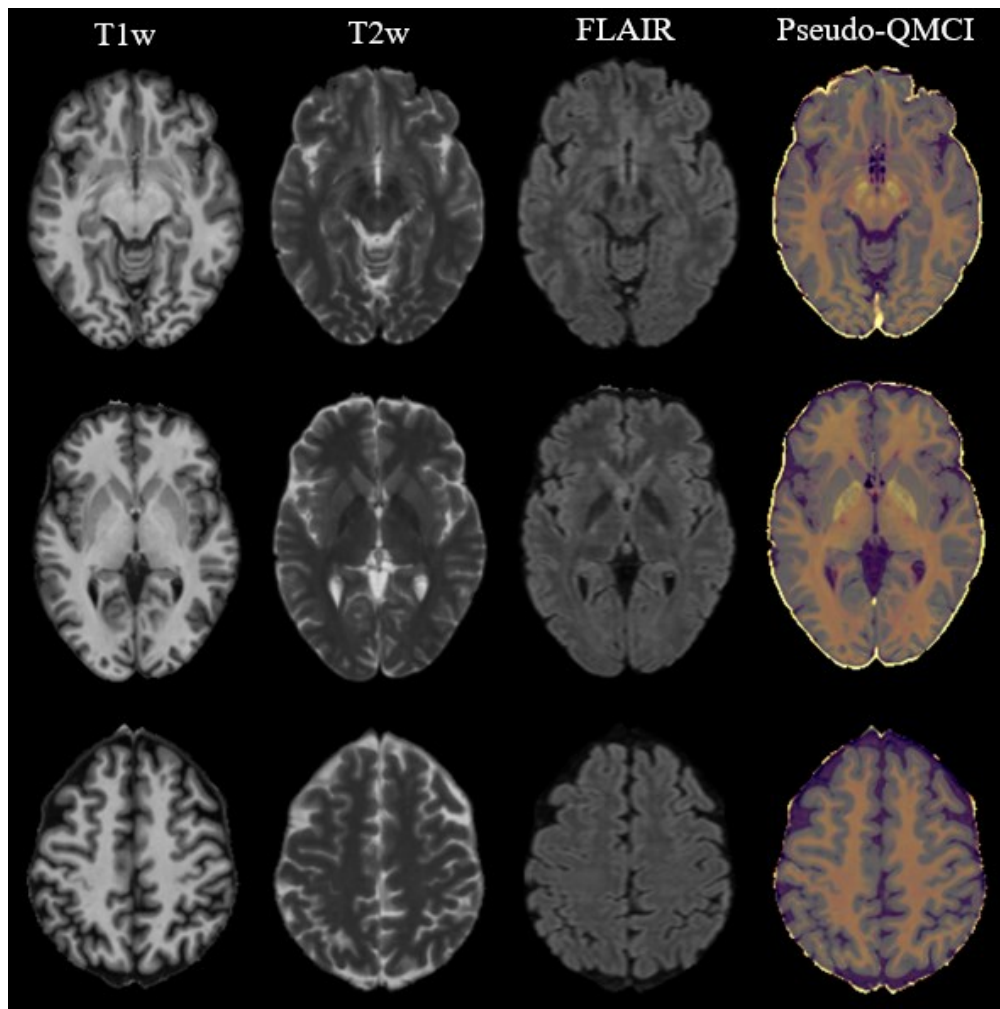
Figure 47 - Pseudo QMCI of a healthy subject. *The figure shows the pseudo-QMCI obtained by means of the polynomial regression-based approach starting from the intensities in the T1w, T2w and FLAIR images of a healthy subject. The bright voxels on the outline represent a layer of low-density proton tissue surrounding the CSF.*

normal brain tissues GM, WM, CSF, thalamus, and basal nuclei (caudate
nucleus, putamen, pallidus, nigra, red nucleus, dentate) adapting to the different
acquisition sequences. The tissues to be segmented are defined by the user. In
the current implementation it is also possible to segment the lesions of WM due
to multiple sclerosis disease.

The software uses two types of *a priori* knowledge:

1) that coming from a model which gives the distribution of tissues in
   physical space and the related features (relaxation parameters), coherently
   with the tissues to be segmented;
2) the anatomical (topological) one described by a series of parameters
   (number of possible agglomerates per tissue, minimum number of voxels
   per agglomerate, grouping by similarity in the feature space, spatial
   contiguity).

In the workflow, the model data (both spatial and feature) are continuously
updated based on those that are gradually obtained from the patient. Another
series of parameters that can be modified by the user affect the entire behaviour
of the code.

5.3.2.1.   Model

By model we mean a voxel-based description both in three-dimensional physical
space and in n-dimensional space of the characteristics derived from different
MRI acquisitions, of normal and possibly pathological intra- and extra-cerebral
tissues. *Phantomag* is an example, which we used as a segmentation template in
this implementation.

5.3.2.2.   Pipeline

The pipeline is divided into three main parts:

1) Elastic registration of the model to the patient:
   a. Affine-only registration of the 4D histogram of the model and the patient
      in the feature space (R1, R2, PD).
   b. Elastic registration of the model on the patient in the patient's space.
2) Pre-classification:
   a. Identification of seeds of brain tissues based on the position-feature
      coincidence of the realigned model.
   b. Extension of seeds by contiguity based on the probability derived from
      the features and the one derived from the position in the model.

c. Definition of a provisional classification map (pre-classification) of all voxels obtained by combining the position probability (derived from the extension) and the similarity of the feature values both to the realigned model and to the patient's already classified voxels.

3) Final classification

a. Starting from the most probable values of the provisional map, classifies the remaining ones taking into consideration not only the spatial position of the tissues already classified, but also the local values of the features in the patient (to take into account any residual inhomogeneities on the rates).

b. Checking of the topological consistency of the result with the anatomical model by declassifying the incompatible voxels.

c. Checking of the coherence of the number and size of the anatomical structures, possibly declassifying the supernumerary and/or undersized ones.

d. Reclassification as in point (3a) but proceeding by contiguity and considering the constraints of the previous points (3b, and 3c); at this point all healthy tissues are classified (and when required also a tissue defined as "potential" MS lesions, followed by the classification of actual lesions).

5.3.2.3. Elastic Registration of the Model to the Patient

The first phase is the realignment, in the feature space, of the distribution of the model to that of the patient, by affine transformation of the 4D histogram of the model and of the patient in the feature space (**Figure 48**). The objective function in this phase is the maximization of the integral of the product of the single features. The transformation is applied to the multi-parametric maps of the model. This first phase makes the subsequent spatial registration much more reliable. In fact, immediately afterwards, the model is registered in an elastic way in the physical space of the patient through the normalization module of SPM12 (*Old_Normalize: Estimate & Write*), which allows defining a template image (our digital model) to be matched with the source image (the patient). Therefore, it is necessary that the contrast in the template image is similar to that of the source image to have a good registration. The transformation, calculated using the R1 maps of the model and the patient, is finally applied both to the multi-parametric maps and to the tissue classification of the model (nearest-neighbor interpolation in order not to invalidate the classification).
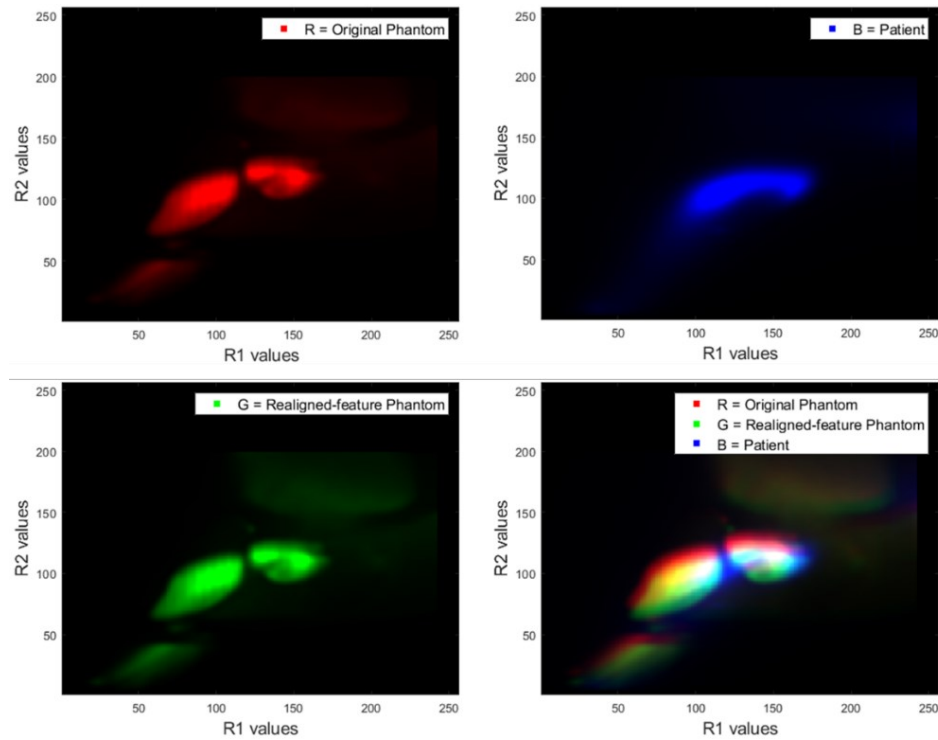
Figure 48 - Realignment of tissue distribution in the R1-R2 plane of the model to the patient. The two-dimensional distribution of the tissues of the digital phantom in the R1-R2 plane (obtained by projecting the 4D histogram in this plane) is shown in red. The one of a patient is shown in blue. Green shows that of the phantom realigned in the feature space. Finally, the overlap of the three is shown, where it can be seen how the green has moved over the blue, which means that the model has been registered to the patient in the feature space.

5.3.2.4. Pre-classification

As anticipated in **Section 5.3.2.2**, the pre-classification phase is in turn divided into 3 phases.

Identification of seed. The seeds of the segmentation are defined differently for the various tissues. Seeds are defined as those patient voxels which, spatially corresponding to a certain tissue of the model (defined as Region of Interest, ROI), also have a value for each feature within a certain range. In particular, they have a feature value that meets three conditions:

1) it is within a given fraction of standard deviation from the center of gravity of the distribution of that tissue in the model;
2) it is within a certain neighbourhood of the maximum of the product between the distribution of the model and that of the patient in the ROI;
3) within the same neighbourhood, the maximum of the patient distribution in the ROI is found and it is verified if the feature falls in the neighbourhood of this maximum.

119
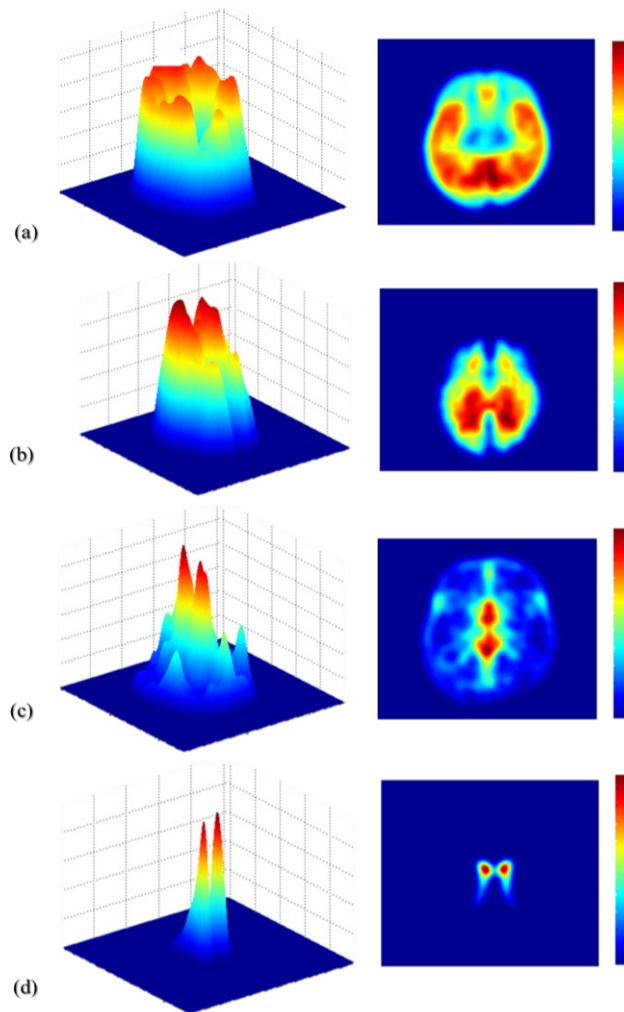
Figure 49 – Position probability map of the patient's tissues in its space. *The first time it is obtained from the model registered in an elastic way to the patient. Subsequently, it is updated according to the pre-segmentation obtained by the patient himself. Figure (a) shows the probability distribution in 3D space of the patient's GM, alongside with the colour coding represents the probability that each spatial voxel belongs to the GM (from 0, which is blue, to red). Figure (b) represents that of the WM, at (c) the CSF and (d) the caudate. It was calculated for all segmented tissues, the four shown here are examples.*

Region growing by contiguity with seeds. Regions grow based on an estimated probability map. It is obtained as the product of the one derived from the combination of the model-patient feature distributions, for that derived from the position of the tissues in the model, resulting from a convolution of the seeds with a given kernel. It is calculated for all brain tissues (**Figure 49**). To admit a voxel to extension, two conditions are used:

1) the voxel contiguous to the tissue to be extended must have a probability greater than a certain percentage threshold of the sum of the probabilities of all tissues;

2) it must exceed the probability of the second most likely by a certain other percentage threshold (current default: 65% and 45%, respectively).

Provisional classification of all other voxels. After updating the probability map in the feature space with the new classified patient voxels and after defining a new spatial probability map of brain tissues derived from the patient's already classified voxels, they are multiplied, and all other voxels are classified according to the maximum probability. Probability maps of all tissues are kept for later use.
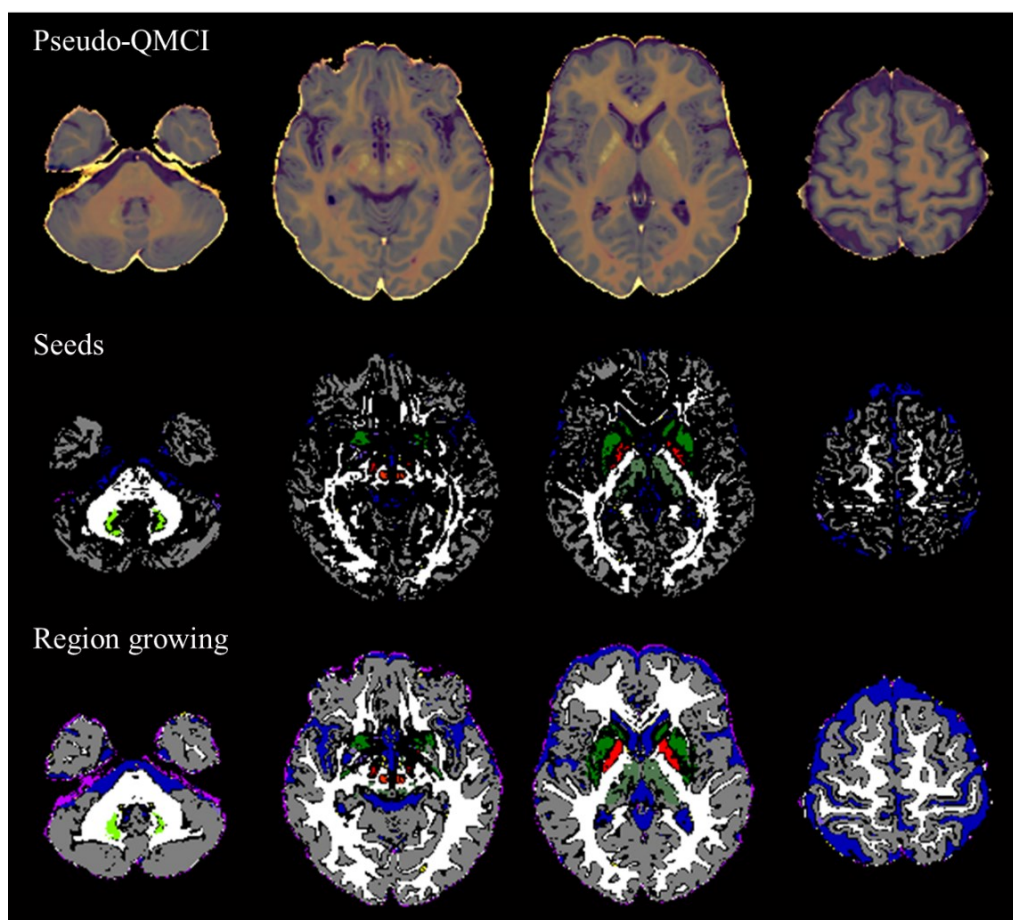
Figure 50 – Steps of pre-classification. *GM is coded in grey, WM in white, the thalamus and some nuclei of the base (dentate, caudate, putamen) in different shades of green, others in red (pale, nigra and red nucleus). The figure shows the results of the various steps of pre-classification starting from QMCI images for four selected slices of interest of a healthy subject.*

5.3.2.5.   Final Classification

As anticipated in **Section 5.3.2.2**, the final classification phase is in turn divided into 4 phases.

Reclassification of "doubtful" voxels based on local features. "Doubtful"
means voxels whose probability of belonging to a particular tissue is less than a
given percentage of the sum of the probabilities of all tissues or the difference in
probability with the second most likely is less than another percentage (current
default values: 72% and 60%, respectively). When reclassifying these voxels,
the feature values considered are those measured in a local window, to take into
account any non-homogeneity. The position probability is updated with all
undoubted voxels.
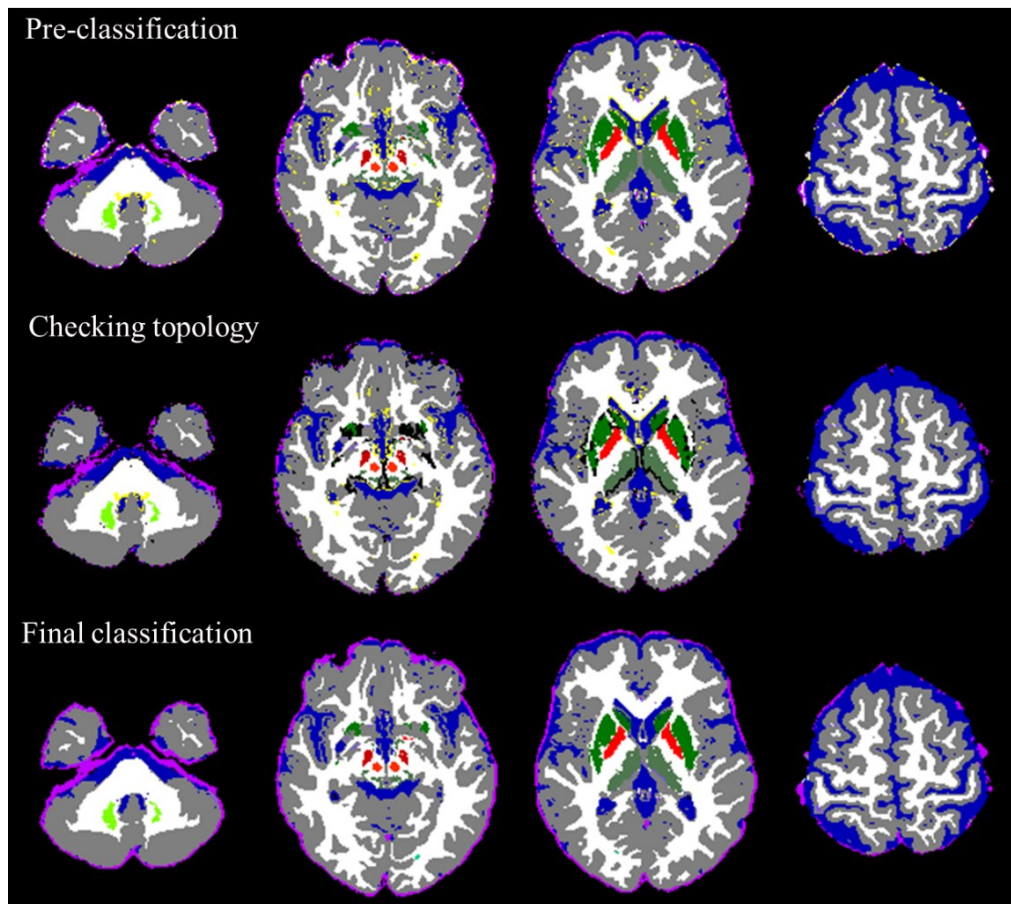
Figure 51 - Steps of segmentation after registration. *The figure shows the results of the various steps of
the segmentation starting from QMCI images (from top to bottom) for four selected slices of interest of a
healthy subject. The first row shows the pre-classification phase that precedes the subsequent definitive
classification phases of checking topology and final classification. In the latter it is possible to observe how
the tissue incompatibilities found between the tissues are resolved, even reclassifying the potential
abnormal white matter (PAWM) tissue (coded in yellow). The colour code of other brain tissues is described
in* ***Figure 50***.

Declassification of topologically incompatible voxels. For the border voxels
between the different tissues the anatomical compatibility is checked and in the
case of incompatibility the one with the lowest probability or both is declassified.

Declassification of supernumerary and/or undersized structures. Each group
of contiguous voxels (agglomerate) classified as the same tissue constitutes a
structure. In the anatomical description the minimum dimensions and the
number of structures for each tissue are defined. All structures inconsistent with
the anatomical description are declassified.

Reclassification by contiguity. The classification proceeds as in the previous
case, but by contiguity, taking into account the anatomical and topological
constraints. At the end of this procedure, all healthy tissues are classified as well
as a possible other, defined as "potential" demyelination lesion tissue (PAWM).
Finally, the lesion classification, which is optional, proceeds according to a
sophisticated demyelination lesion classification algorithm, which improves on
one previously developed for multiparametric segmentation based on relaxation
parameter maps [120]. In the case of healthy subjects, PAWM classification
proceeds by reassigning them to GM, WM, or CSF.

The results of the entire procedure are shown in **Figure 50** and **Figure 51**.

5.3.3.   Results

Figure 52 shows the result of segmentation on a healthy subject for which a
T1w, a T2w and a FLAIR were available.
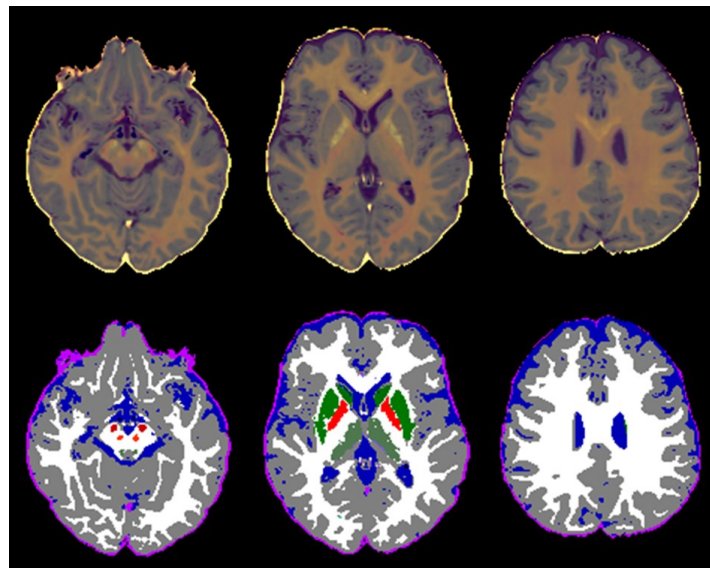
Figure 52 - Result of segmentation on a healthy subject. *The first row shows the pseudo-QMCI of three
different cross brain sections, obtained through the polynomial regression-based approach, starting from
the T1w, T2w and FLAIR images of the subject. The second line shows the result of the segmentation applied
on the pseudo-QMCI. In grey is the segmentation of GM, in white WM, in blue CSF, in pink a contour of
low PD tissues. The three different green colour coding represent caudate nucleus, putamen, and thalamus.
The three different red colour coding represent substantia nigra, red nucleus and pallidus.*

The pseudo-QMCI (**Section 5.3.1**) were calculated from the signal intensities, on which the multi-parameter segmentation pipeline was then applied (**Section 5.3.2**). The pipeline was optimized on real CSE-based QMCI studies; however, the segmentation result is accurate even on the basal nuclei, showing good reliability of pseudo-relaxation parameter maps simulation.

For completeness, **Figure 53** shows the result of the segmentation obtained on a patient with multiple sclerosis of which the three clinical studies containing a T1w, T2w and FLAIR were available.
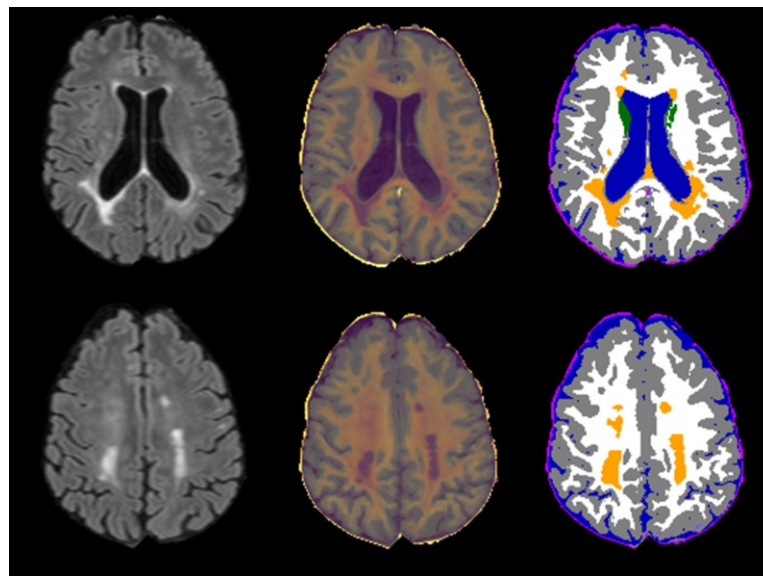
Figure 53 - Result of the segmentation of a multiple sclerosis patient. The figure shows two selected cross sections of the patient. From left to right we find FLAIR, pseudo-QMCI and segmentation. In FLAIR, multiple sclerosis lesions appear as hyperintense changes in the focal signal. In pseudo-QMCI the lesions have the typical appearance they did in real QMCI derived from CSE. They occur in a distinguishable purplish colour on the WM. In segmentation, multiple sclerosis lesions are represented in orange.

The developed multi-parametric segmentation approach was validated on a set of 66 CSE studies of patients with multiple sclerosis (22 males, 36.4 ± 6.9 y.o., EDSS 3.0 ± 0.8). The results were compared with those obtained with previously validated software for the segmentation of the R1, R2 and PD maps [119, 120]. The volume of each tissue was calculated from the segmented maps and, to take into account the size of the head, for the subsequent statistical analysis, it was divided for each subject by the corresponding total intracranial volume (ICV, the sum of the voxels of all tissues intracranial including CSF), thus providing fractional tissue volumes (fGM, fWM, fCSF). Regression analysis of fGM, fWM and fCSF with age showed non-significant differences ($p < 0.05$) between the two segmentations. In particular, in both cases a significant decrease ($p > 0.05$) in GM and a significant increase in CSF with age was obtained. This is due to

the natural atrophy of the cerebral cortex that occurs with aging and also to the pathology (**Figure 54**). The same was then applied to a group of 64 patients with multiple sclerosis of comparable age, sex and disease severity (25 males, 36 ± 9.0 y.o, EDSS 3.2 ± 0.8) for which clinical studies (including a T1w, FLAIR and T2w sequence) were available. For these, the software first calculates the maps of the pseudo-relaxation parameters and then applies the segmentation. The regression results are not significantly different ($p < 0.05$) from those obtained on the similar CSE group of subjects. While the regressions of fGM and fCSF with age show a significant ($p > 0.05$) decrease in GM and a growth in CSF, comparable to those obtained for CSE studies.
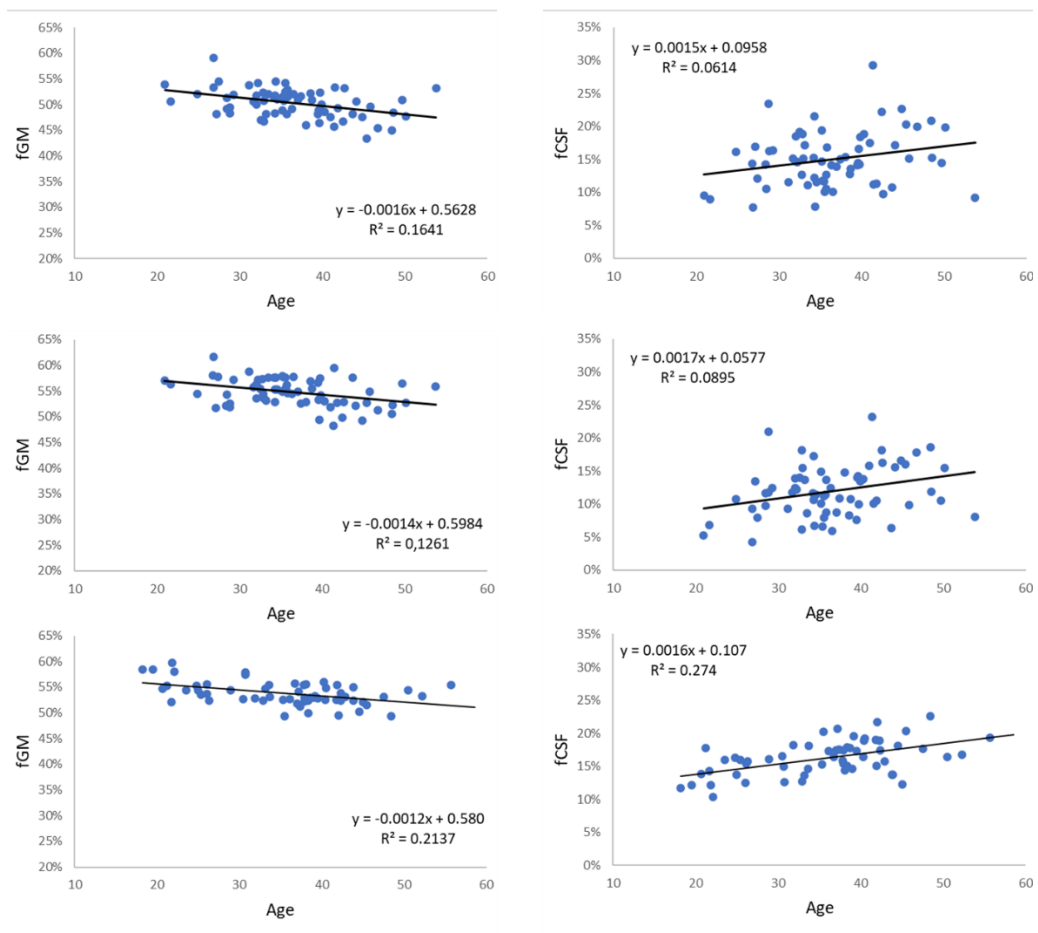
Figure 54 - Regression analysis of tissue volumes with age. *Comparison of the regression of the fractions of GM, WM, CSF with the age measured on the CSE with the previous multiparametric segmentation method (top row) and with the new segmentation approach (middle row). The last row shows the result obtained on pseudo-relaxation maps obtained from a similar group of MRI clinical studies (including a T1w, T2w and FLAIR). A significant decrease in fGM with age coupled with an increase in fCSF, with no significant changes in fWM with age, could be demonstrated using both methods, with no significant differences in the slopes corresponding to the general linear model.*

Chapter 6

Discussions and Conclusions

6.1. Discussions

The thesis work addresses the different development phases (segmentation, modelling and prototyping) of innovative techniques to devise anthropomorphic brain phantoms using modern 3DP technologies. These devices are used as test objects for morpho-functional medical imaging studies. They can simultaneously simulate the physical, geometric, and physiological characteristics of the normal human brain, and provide a useful tool for the evaluation of inaccuracies in medical imaging systems. Brain phantoms are used to reduce quantitative variability due to differences in acquisition settings and intrinsic characteristics of the various imaging modalities, reproducing images similar to those detectable in healthy brain tissues according to the distribution of densities for CT, signal intensity for MRI and radiotracer for ECT. In the latter case, they allow detecting quantitative or semi-quantitative measurements of the physiological and metabolic activities of *in vivo* brain tissues. For this reason, they are particularly used for the evaluation of inaccuracies in PET/SPECT studies (registration error, limited spatial resolution, partial volume effect and noise on images), since, once characterized by natural shapes and sizes, they can render tests on nuclear medicine systems more realistic and intuitive than those carried out by simple geometric (calibration) phantoms.

6.1.1.   A New Brain Phantom

Since the human brain is both a topologically and functionally complex organ, physical phantoms typically do not reproduce the variety, nor the inhomogeneities in the brain tissues density/intensity/uptake. The physical brain phantoms rather try to emulate the external shape of the brain with a reduced depth of the sulci and an unlikely representation of the circumvolutions. Generally, they are made using various types of moulds, obtained from MRI images of a normal subject, and, even when a cast that is fairly faithful to the brain anatomy is obtained, it is still not possible to simulate the physiological variety of brain tissues (through other compounds of wax and/or gel, or

polyvinyl-based) [68, 142, 143]. The moulds are usually preferred because the alternative would be to create phantoms that can be filled with chemical solutions (to mimic the different brain imaging studies), in a single piece, and with separation walls between the phantom compartments, tracing the interface surfaces between them. In these cases, the separation walls are visible in imaging, or often the production technology is not suitable to materialize surfaces as complex as the brain in a single object. Therefore, solutions that can be assembled or made in several parts are proposed.

To overcome the limitations of brain phantoms currently available, and to enrich the range of medical imaging applications, we have designed and implemented a new paradigm for the creation of anthropomorphic brain phantoms, starting from the idea of a new brain phantom (**Section 3.2**). While embodying some of the features of the previously patented *STEPBrain* phantom (**Section 2.3.5.3**), the new phantom is more advanced in terms of properties, production techniques and possible applications. It consists of three separate compartments to simulate the activity of three brain tissues: GM, WM, and striatum. The presence of striatum is a first important element of innovation. Indeed, to date, there is no brain phantom that can simulate these three compartments simultaneously. The phantoms at the current state of the art allow simulating only the compartments of GM and WM (**Section 2.3.5.1**), or the striatum (**Section 2.3.5.2**). Furthermore, the striatum has a high uptake in nuclear medicine studies, and for this reason it is of great interest for phantom simulation. During the design we also set out to create walls at the interface between the three (hollow) compartments with a thickness that was sub-millimetre, preferably in the range 0.4 – 1 mm. This requirement is necessary to make it suitable for the characterization of hybrid (morpho-functional) diagnostic scanners with MRI and CT (i.e., hybrid scanners PET-CT, PET-MRI, and SPET-CT). The latter constitute the frontier of diagnostic imaging, as they provide synergistically both the morphological and functional information of the patient. This would allow scans to be performed with a minimum thickness of the acquired slices of less than a millimetre, while in the state of the art of brain anatomical phantoms, this is generally not possible. An example is the *Hoffmann Brain Phantom* (**Section 2.3.5.1**), the most widespread among all, for which the minimum thickness of the acquired layers cannot be below 6 mm. In addition to the promising applications of the new brain phantom, there could be quantization and correction of the partial volume effect, which is a typical defect of ECT. This would be possible only thanks to the high resolution of the phantom and therefore to its usability in MRI, which is not always feasible with the other existing brain phantoms. For such applications, the three chambers of the phantom must be absolutely separated from each other (i.e., the compartments

must never be in connection) and the walls at the interface between the compartments and those towards the outside must be waterproof (**Section 3.2**).

6.1.2.   3D Modelling and Prototyping Techniques

The working prototype of the new brain phantom is the result of an innovative 3D modelling and materialization pipeline implemented *ad-hoc* for the most modern AM techniques. The additive logic of a production made *layer-by-layer* has the merit of the enormous potential expressed in the creation of anatomical models for various applications (**Section 1.4.2**). Compared to the spread in the biomedical field, the use of 3DP for the creation of anthropomorphic phantom is rather limited. 3DP technology is not yet mature enough to be considered *plug-and-print*, and probably this aspect can be daunting for the creation of very complex objects, such as anthropomorphic phantoms. As explained in **Chapter 1**, modelling errors may occur at any stage of the procedure, including image acquisition, segmentation, and post-processing, as well as printing. However, although the appropriate choice of 3DP modality and materials is critical to achieve optimum accuracy, image segmentation and STL conversion also remain error-prone steps. Indeed, according to our experience, it is not only the production of brain phantoms that still requires a considerable research effort for the improvement, and subsequent consolidation, of the techniques, but also the whole 3D modelling workflow to obtain a 3D printable phantom's model, and then the best product in the shortest possible time. As seen, both the model designing phase (discussed in **Chapter 3**) and the materialization phase through 3DP (discussed in **Chapter 4**) were very laborious. The two phases necessarily had to be experienced in parallel, because neither is independent of the other and required a *trial-and-error* experimentation approach. In the first phase, the difficulties were due to the integration of more software for the realization of a model adapted to the specifications, while in the second phase the potential and the limits of 3DP technologies in the physical realization of the phantom came into play. In a preliminary phase of phantom materialization, since the technological process behind it is basically the same of professional FDM, we tested the FFF technology of the entry-level or semi-professional material extrusion printing (**Section 1.3.1.4**), obtaining a first rudimentary phantom with internal non-removable supports (such as *STEPBrain* phantom, **Figure 13**), and then developing a procedure for the automatic design of *ad-hoc* soluble supports for modelling complex anatomical phantoms (**Section 4.3.1**). The automatic *ad-hoc* support structures generation is adaptable for various slicing software of entry-level and/or semi-professional 3DP, but currently cannot be used for professional printing. These 3DP systems allow only a minimal customization of the supports based on the parameters that can be set using the slicing software

(**Section 4.3.2.1**). However, FDM 3DP turned out to be the best candidate for the stability, durability, and robustness of the final product. It allows materializing submillimetre (0.5 mm) walls as per phantom specification and, unlike the PolyJet, completely cleaning the phantom from internal supports (**Figure 30**). The processing methods of the FFF are almost identical to those of the FDM, but the differences in the technical characteristics of the machine and in the proprietary materials (especially, QSR support material) made the second (*Stratasys F370^{TM}*) more suitable than the first (*RAISE3D N2 Plus*) to our production needs. The prototypes in ABS are pleasing to the eye (**Figure 29**), and even more if covered with a transparent and glossy protective plastic spray paint in post-production (**Figure 33**). In addition to the properties described in **Section 1.7**, ABS is a convenient choice for MRI applications due to its low magnetic sensitivity, whereby ABS structures can be "MRI-invisible". The only drawback of using ABS is that it produces a pungent smell during extrusion, so it is recommended to work with it in a ventilated environment. The professional machine is more reliable for very long prints in ABS, like that of the brain phantom which lasts a week (7 days and 3 hours). In addition, it has a temperature-controlled working environment, and more advanced nozzle cleaning system, which allows excellent control of the annoying problem of dripping material from the nozzles during printing due to high temperatures (present in FFF printers, for which it is still difficult to manage). Furthermore, the QSR support material efficiently matches to construction material and, if the machine is properly calibrated, there is no risk that the materials can mix during the deposition. The support structures do not leave marks on the printed pieces and, above all, do not cause imperfections in the printed wall (which could result in holes) due to lack of supports in the critical points (**Figure 28**).

As seen in **Chapter 4**, in addition to the build material and support structures, there are still other printing parameters that affect the creation of the anthropomorphic brain phantom, from print speed to layer height. According to our experience, the layer height affects not only the aesthetics and resolution of the printed piece but determines the minimum (vertical and horizontal) wall thickness that can be achieved, while maintaining strength and functionality (no holes) of the phantom walls. A basic design guideline is to keep the wall thicknesses as uniform as possible and not less than 1 mm (**Section 1.5.2.2**). However, our phantom had to have a wall thickness between 0.4 and 1 mm. The layer height available for ABS printing on *Stratasys F370^{TM}* 3D printer are 0.3302 mm, 0.2540 mm, 0.1778 mm, and 0.1270 mm (**Table 3**). We did not take into consideration the 0.3302 mm layer height because it is generally recommended for draft pieces, which do not need much surface finishing. In addition to a rough aesthetic rendering, there may also be holes in the print weft, which cannot be solved with the waterproofing processes identified for the

phantom. The 0.1270 mm layer height should be avoided, first because the print would become very long, and also because it is generally not recommended unless strictly necessary, as in the case of small pieces that require fine and precise details. In general, the prints obtained at layer height equal to 0.2540 mm or 0.1778 mm are considered the best compromise for printing complex large objects, such as the brain phantom. The choice between the two therefore depends on which allows obtaining the lowest wall thickness in the indicated range of 0.4 – 1 mm, respecting all the other specifications of the phantom (robustness and impermeability). The wall thickness in the 3D model of the brain phantom depends primarily on the voxelized surfaces extracted from the segmented images by our automatic procedure (**Section 3.3.3.1**), and therefore on the size of the isotropic voxel. It determines the minimum wall thickness in the 3D model. The voxel size of 0.5 mm in all directions in our final 3D model also defines the minimum uniform wall thickness that can be printed according to the print specifications related to the layer height. Indeed, although choosing a multiple voxel size of layer height might seem intuitive, this solution would not have brought us to the minimum printable (uniform) wall thickness in the range set for the phantom. To clarify this aspect, it is necessary to distinguish the vertical wall thickness from the horizontal wall thickness. To ensure uniformity of the overall wall thickness they must be approximately equal, but, during the construction, the deposition of the vertical and the horizontal walls follows two different logics. To obtain a strong vertical wall, at least two juxtaposed shells must be printed (**Figure 25**), each having, by definition, a width approximately equal to the double of the layer height. Therefore, 2 juxtaposed shells of thickness equal to (2×0.2540 mm) for a vertical thickness of at least 1.0616 mm; or 2 juxtaposed shells of thickness equal to (2×0.1778 mm) for a vertical thickness of at least 0.7112 mm. For horizontal walls, on the other hand, it is necessary that they consist of at least two layers (equal to layer height) superimposed to be robust (**Figure 26**), therefore (2×0.2540 mm) = 0.508 mm; or (2×0.1778 mm) = 0.3556 mm. According to these calculations, setting a voxel size multiple of layer height would not have solved the problem of printing submillimetre thicknesses at all. For this reason, we have chosen for 3DP the layer height of 0.1778 mm in order to guarantee the lowest vertical and horizontal wall thickness, to then optimize the other printing parameters to be able to materialize a uniform wall thickness of about 0.5 mm. This was possible because the *Insight for GrabCAD* slicing software provides advanced settings, which regularize the wall thickness where it is too thin (in this case for the vertical thickness), going to thicken only in some parts according to the construction needs (depositing at least 2 juxtaposed shells for the vertical walls). Although the layer height had been appropriately set, further optimization of the printing parameters was necessary (**Section 4.3.2.1**) to reduce to the minimum

the airgaps in order to then be able to waterproof the phantom. With an optimized print texture, treatment with acetone can lead to the result, but it can also damage the phantom irreversibly (**Section 4.4.1**). Using a solution of polyvinyl-acetate glue and water, the waterproofing result is instead stable (**Section 4.4.2**), there is no thickening of the walls, nor deposition of the glue in the phantom that could obstruct the gooseneck passages (which would happen using resins). Finally, the filling system allows the homogeneous distribution of the radioisotope/contrast medium/mimetic solution in each single compartment (**Section 4.5**), also allows minimizing the exposure of operators.

The result of the first test scans obtained in CT (**Figure 36**) and PET-CT (**Figure 37**) show a realism of the simulation result not obtainable with any of the brain phantoms available at the state of the art.

6.1.3.   A New Brain Segmentation Approach for 3D Printing

To date, there is limited segmentation software designed specifically for medical 3DP, some open source, but most proprietary/commercial. On the other hand, most visual aids, and manipulation tools currently available to radiologists for post-processing are not suitable for 3DP purposes. This paucity should be addressed in parallel with the evolution of other aspects of medical 3DP, which however, as seen, currently still requires a lot of effort for experimenting and printing complex anatomical models. Therefore, in addition to demonstrating the feasibility of the complex anthropomorphic brain phantom, our attention has turned to the development of a new brain segmentation approach (**Chapter 5**), which incorporates established multiparametric segmentation methods [119, 120], extending them to allow segmentation of MRI sequences currently used in clinical practice with sufficient reliability. The aim was to obtain a versatile brain segmentation software (also usable for pathologies characterized by focal signal alterations in brain tissues, such as multiple sclerosis), which allows segmenting high-resolution MRI images. This was needed to obtain high-resolution brain tissue maps, that could allow improving the anatomic rendering of the already prototyped phantom, managing to render a greater depth of the sulci and fidelity of the convolutions. Secondly, to provide a tool for the creation of customizable anatomical brain phantoms/models starting from routine MRI studies acquired for clinical purposes, without the need of acquiring additional, dedicated sequences, that would reduce the diffusion of the method.

In the past, quantitative maps of relaxation parameters R1, R2 and PD were computed by status equation from CSE images and used as an intermediate step to segment normal and abnormal brain tissues, using multiparametric segmentation methods (**Section 5.2.2.4**). Over time, faster sequences (e.g., TSE) and 3D (e.g., MPRAGE, 3D-TFE with higher resolution), as well as sequences

with improved sensitivity to pathological changes (e.g., FLAIR), have progressively replaced CSE in routine clinical practice [125]. When brain MRI images are acquired for modeling purposes it is acceptable to obtain them from different acquisition sequences. Image resolution also remains an important aspect for segmentation, as well as for modeling intended for 3DP. We showed that it is possible to define a polynomial function that correlates the signal intensities of the voxels in the MRI images obtained from a set of heterogeneous sequences of a subject (T1w, T2w and FLAIR) with the R1, R2 and PD values of the same voxels, provided that both the signal intensity and the relaxation rates are known for a considerable portion of the voxels (**Section 5.3.1**). The pseudo-relaxation parameter maps obtained for a subject (**Section 5.3.1.4**) are thus usable for multi-parameter segmentation based on relaxometry. The new multiparametric segmentation approach is basically based on propagation of the labels deriving from a digital phantom (**Section 5.3.2.1**), which provides the *a priori* knowledge for relaxation parameter maps (R1, R2, PD) and tissue classification. The developed multiparametric segmentation pipeline (**Section 5.3.2.2**), being based on relaxometry, allows simultaneously segmenting the main normal brain tissues (GM, WM, CSF), thalamus, basal nuclei (caudate nucleus, putamen, pallidus, nigra, red nucleus, dentate), as can be seen in the **Figure 52**. In the current version of the software, it is also possible to segment multiple sclerosis lesions (**Figure 53**). To the best of our knowledge, this is not currently possible with other brain segmentation software. The pipeline has been tested on a healthy volunteer and successfully validated on QMCI and pseudo-QMCI studies of patients with multiple sclerosis (**Section 5.3.3, Figure 54**). The versatility of this approach makes it a valuable tool for brain modeling aimed at 3DP, particularly for the creation of customized and/or pathology-specific phantoms.

6.2. Conclusions

The design and construction of an accurate 3D-printed anthropomorphic brain phantom is a complex process that requires the integration of diversified skills that involve many disciplines (from biomedical engineering to physics and radiology). Although a 3D-printed anatomical model derived from medical images represents a natural progression from its 3D visualization, the techniques to move from images to the printable model are constantly evolving, and the workflows proposed for these operations are often very different depending on the application. The effort to improve 3DP applications in medical imaging research requires the development of new segmentation methodologies, leading to the creation of actual 3D modelling tools for 3DP, which can guide the designer from the idea to the finished product. According to our experience, a

lot of research is still needed to bring 3DP technologies and machines closer to the demands of 3DP in biomedical applications, specifically for cutting-edge applications, such as the creation of anthropomorphic phantoms. Although there are some examples of 3D-printed anatomical phantoms, and despite the enormous potential expressed by these objects, there are still few 3D modelling and manufacturing techniques expressly developed for these purposes. Probably, in the next few years, some of these applications could become case studies to be proposed directly to 3D printer manufacturers to try to overcome the current limits that FDM/FFF technology (as well as the others) places with respect to the materials available, but above all to production times.

The prototyping work of the anthropomorphic brain phantom proposed in this thesis has led to the development of new segmentation, modeling and 3DP techniques, exploring the creation process from the idea to the finished product. The technological limits have been promptly addressed and resolved, sometimes through compromise solutions. For example, printing time is certainly not optimal, but given the complexity of the structures of the designed anthropomorphic brain phantom, the possibility of repeating long prints, and considering that one of the current limits for printing complex objects is precisely the printing time, we considered that, at the moment, a week of printing is an acceptable compromise for the materialization, also for a possible future marketing of the product. Our brain phantom is an extremely innovative product compared to the current state of the art, and it is also in terms of the production process, which certainly can be further developed in the future. The specific waterproofing process, which is the result of research activities centered on the study of special waterproofing treatments of 3D-printed prototypes, will also be improved to reduce the time required for the complete waterproofing of the phantom. Currently, interior surfaces are the most difficult to waterproof because not all points are reached in a single treatment, and it is difficult to have control over this process. We are therefore implementing control strategies that allow us to solve some critical issues in the waterproofing process. Despite its complexity, the phantom, which simultaneously simulates three brain compartments, is designed to ensure a fair *ease-of-use*, and at the same time provide a unique tool for the characterization and validation of multiple imaging modalities. In this sense, it proposes an advance with respect to the brain physical phantoms currently available and, moreover, the developed technological solution opens the way to a diversification of the product to simulate different pathological situations (for example, brain tumors) or even other organs. The brain segmentation software will in fact be further validated on normal subjects to test the concept of phantom customization; but also integrated, where possible, with procedures for the segmentation of brain pathologies.

The filling system is also designed to be *easy-of-use*; however, it will need to be improved for optimal filling without air bubbles, which could cause areas of hypo-intensity in the imaging and prejudice the simulation result. Currently, the procedure for air bubbles removal is not straightforward, as it involves a series of steps (pre-filling by dipping and shaking before using the pump system). Since there is no control over the actual escape of air bubbles, we will try solutions for emptying the air from the phantom before filling, which must be carried out by the operators in simplicity and in the greatest possible safety. The pump system greatly simplifies the procedure, allowing the operator to exit the laboratory during filling to minimize radiation exposure. Therefore, we will proceed with further research to refine the design of the access routes to the compartments and the integrated system for placing radioisotopes/contrast media/mimetic solutions.

The need to create increasingly realistic anatomical phantoms, usable for different morpho-functional imaging simulations, is destined to emerge more and more given the growing interest in multi-modal and multi-parametric imaging modalities. Consequently, the effort aimed at customizing modeling processes and developing of 3DP technology for these applications is expected to grow significantly in the coming years. The increase in precision induced by technology will lead to a demand for the replacement of old technology products and a growing diffusion of these products, due to the widening of the application field. Furthermore, the ability to simulate three brain compartments at the same time, as well as the possibility of carrying out multi-modality studies, gives this device prospective characteristics, which will be quantifiable through multi-centric comparative studies that can be started in the next future.

Acknowledgments

First of all, I would like to express my gratitude to Dr. Bruno Alfano for having initiated this research activity and for having constantly followed its developments with enthusiasm. He has encouraged me to believe in the results of my research and his dedication to work has been a constant source of inspiration and valuable teachings. I also thank my co-tutors Dr. Mario Quarantelli and Ing. Mario Magliulo for the teachings, for always being ready to welcome my requests for the progress of research activities and for supporting me during the years of fellowship at the Institute of Biostructures and Bioimaging (IBB) of the National Research Council of Italy (CNR), based in Naples.

I thank my tutor Prof. Mario Cesarelli for advising me during my Ph.D. years and for having led me to explore the world of research in the biomedical field, also through experiences abroad and support activities for students of Biomedical Engineering. In the Biomedical Engineering (BME) group of the Department of Electrical Engineering and Information Technologies (DIETI) of the University of Naples "Federico II" I found a place where I can communicate with colleagues, grow, and learn.

I warmly extend my thanks to all my family, my life partner, and my friends. They know why.

Appendix

Below, we provide detailed flowcharts of each brain phantom prototyping phase.

The **Flowchart (A)** summarises, according to our experience, the complete workflow to obtain a 3D-printed anthropomorphic brain phantom to be used for morpho-functional imaging studies.

The **Flowchart (B)** summarises, with relevant details, the design stage of the brain phantom prototyping. The design, from segmentation to 3D modelling, and STL extraction and refinement, is presented in **Chapter 3**. The **Chapter 5** presents the new approach for brain imaging segmentation.

The **Flowchart (C)** summarises, with relevant details, the materialization stage of the brain phantom prototyping. The materialization, explored in **Chapter 4**, is achieved through FDM 3D Printing, then the phantom is waterproofed for filling. Different contrast medium/radioisotope concentrations can be used to simulate different brain imaging studies.

Flowchart (A) – Complete step-by-step workflow to obtain the brain phantom.

BRAIN PHANTOM – COMPLETE WORKFLOW

1 **MEDICAL IMAGING**
High-resolution acquisitions of brain images (MRI)

2 **IMAGE POST-PROCESSING**
Segmentation of brain images to extract the 3D model

3 **STL EXTRACTION**
Interface format suitable for 3D Printing

4 **MESH REFINEMENT**
Manifoldness check and mesh correction

5 **SLICING**
STL model is sliced by means of slicing software

6 **3D PRINTING**
Ready to print?!

7 **WATERPROOFING**
For filling with different solutions to simulate imaging modalities

8 **FILLING SYSTEM**
A special filling system for the brain phantom

9 **IMAGING SIMULATION**
CT, MRI, PET/TC, SPECT/TC, PET/MRI scan of brain phantom

Flowchart (B) – Design workflow to obtain the 3D model of brain phantom.
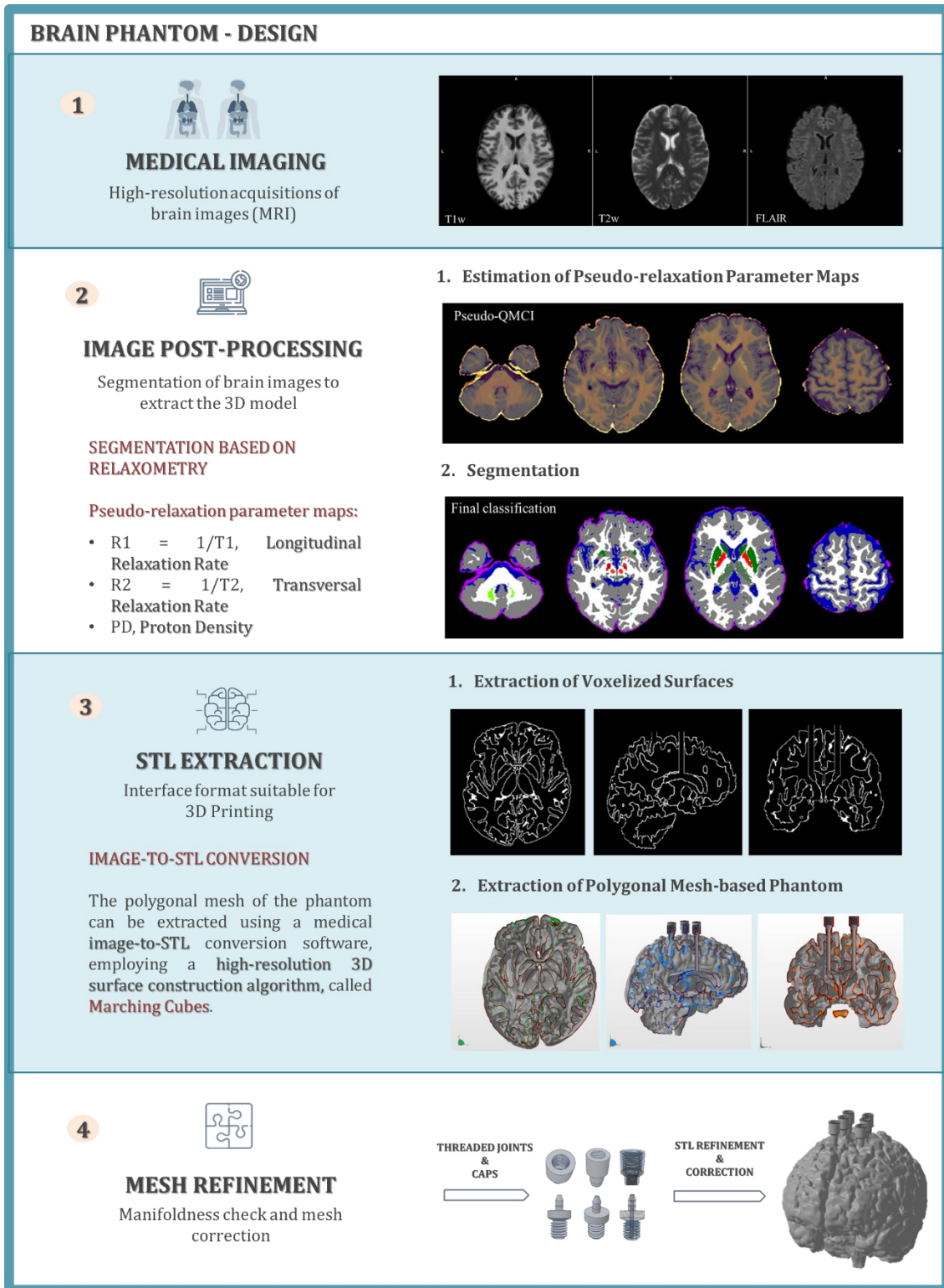
Flowchart (C) – 3D printing materialization of a functioning brain phantom.

BRAIN PHANTOM - MATERIALIZATION

5

SLICING

STL model is sliced by means of slicing software

LAYER HEIGHT (LH) SETTING

(a) LH = 0.1778 mm, option to thicken walls activated

↓

2 juxtaposed vertical walls (= 2 × LH thick)

(b) Advanced optimization of printing parameters to reduce airgaps

SUPPORTS OPTIMIZATION

• Smart supports with dense support layer

1. **Optimization of Printing Parameters**

(a)   (b)
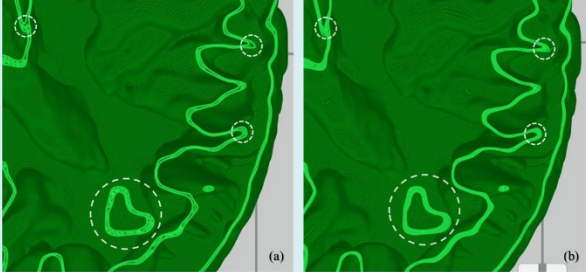
2. **Optimization of *Ad-hoc* Supports for Critical Points**

Critical point (A)
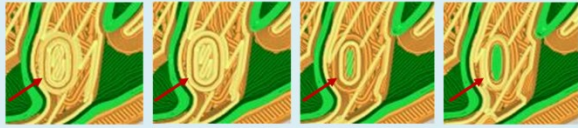
(A.1)   (A.2)   (A.3)   (A.4)

Critical point (B)
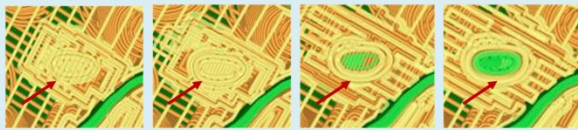
(B.1)   (B.2)   (B.3)   (B.4)

6

3D PRINTING

Ready to print?!

REMOVAL OF SOLUBLE SUPPORTS

The FDM washing system **Support Cleaning Apparatus** (SCA-1200HT) allows the removal of all internal supports.
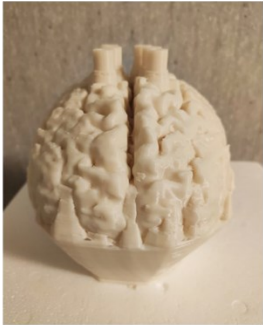
Printing Time

7 days and 3 hours

(2 extruders)

7

WATERPROOFING

For filling with different solutions to simulate imaging modalities

Solution

Water and polyvinyl acetate (20% and 80% of the total volume)

References

[1]   I. Gibson, D. W. Rosen, and B. Stucker, "Introduction and Basic Principles," in *Additive Manufacturing Technologies: Rapid Prototyping to Direct Digital Manufacturing*, I. Gibson, D. W. Rosen, and B. Stucker, Eds. Boston, MA: Springer US, 2010, pp. 20-35.

[2]   A. Aimar, A. Palermo, and B. J. J. o. h. e. Innocenti, "The role of 3D printing in medical applications: a state of the art," vol. 2019, 2019.

[3]   C. W. Hull *et al.*, "Methods and apparatus for production of three-dimensional objects by stereolithography," ed: Google Patents, 1991.

[4]   S. S. Crump, "Apparatus and method for creating three-dimensional objects," ed: Google Patents, 1992.

[5]   R. Jones *et al.*, "RepRap–the replicating rapid prototyper," vol. 29, no. 1, pp. 177-191, 2011.

[6]   G. Borenstein, *Making things see: 3D vision with kinect, processing, Arduino, and MakerBot*. " O'Reilly Media, Inc.", 2012.

[7]   D. Mitsouras *et al.*, "Medical 3D printing for the radiologist," vol. 35, no. 7, pp. 1965-1988, 2015.

[8]   F. J. Rybicki and G. T. J. C. S. I. P. Grant, "3D Printing in Medicine," 2017.

[9]   I. Gibson, D. Rosen, and B. Stucker, "Vat photopolymerization processes," in *Additive Manufacturing Technologies*: Springer, 2015, pp. 63-106.

[10]   I. Gibson, D. Rosen, and B. Stucker, "Material jetting," in *Additive Manufacturing Technologies*: Springer, 2015, pp. 175-203.

[11]   I. F. Ituarte, N. Boddeti, V. Hassani, M. L. Dunn, and D. W. Rosen, "Design and additive manufacture of functionally graded structures based on digital materials," *Additive Manufacturing,* vol. 30, p. 100839, 2019/12/01/ 2019.

[12]   I. Gibson, D. Rosen, and B. Stucker, "Binder jetting," in *Additive manufacturing technologies*: Springer, 2015, pp. 205-218.

[13]   S.-I. Park, D. W. Rosen, S.-k. Choi, and C. E. J. A. M. Duty, "Effective mechanical properties of lattice material fabricated by material extrusion additive manufacturing," vol. 1, pp. 12-23, 2014.

[14]   I. Gibson, D. Rosen, and B. Stucker, "Powder bed fusion processes," in *Additive Manufacturing Technologies*: Springer, 2015, pp. 107-145.

[15]   I. Gibson, D. W. Rosen, and B. Stucker, "Sheet lamination processes," in *Additive Manufacturing Technologies*: Springer, 2010, pp. 223-252.

[16] I. Gibson, D. Rosen, and B. Stucker, "Directed energy deposition processes," in *Additive Manufacturing Technologies*: Springer, 2015, pp. 245-268.

[17] S. V. Murphy and A. J. N. b. Atala, "3D bioprinting of tissues and organs," vol. 32, no. 8, pp. 773-785, 2014.

[18] W. C. Wilson Jr and T. Boland, "Cell and organ printing 1: Protein and cell printers," *The Anatomical Record Part A: Discoveries in Molecular, Cellular, and Evolutionary Biology,* https://doi.org/10.1002/ar.a.10057 vol. 272A, no. 2, pp. 491-496, 2003/06/01 2003.

[19] T. Boland, V. Mironov, A. Gutowska, E. A. Roth, and R. R. Markwald, "Cell and organ printing 2: Fusion of cell aggregates in three-dimensional gels," *The Anatomical Record Part A: Discoveries in Molecular, Cellular, and Evolutionary Biology,* https://doi.org/10.1002/ar.a.10059 vol. 272A, no. 2, pp. 497-502, 2003/06/01 2003.

[20] X. Wang *et al.*, "3D bioprinting technologies for hard tissue and organ engineering," vol. 9, no. 10, p. 802, 2016.

[21] A. D. Cetnar *et al.*, "Patient-Specific 3D Bioprinted Models of Developing Human Heart," *Advanced Healthcare Materials,* https://doi.org/10.1002/adhm.202001169 vol. n/a, no. n/a, p. 2001169, 2020/12/04 2020.

[22] C. Serrano, H. van den Brink, J. Pineau, P. Prognon, and N. Martelli, "Benefits of 3D printing applications in jaw reconstruction: A systematic review and meta-analysis," *Journal of Cranio-Maxillofacial Surgery,* vol. 47, no. 9, pp. 1387-1397, 2019/09/01/ 2019.

[23] C. Wang *et al.*, "3D printing in adult cardiovascular surgery and interventions: a systematic review," (in eng), *Journal of thoracic disease,* vol. 12, no. 6, pp. 3227-3237, 2020.

[24] M. Attaran, "The rise of 3-D printing: The advantages of additive manufacturing over traditional manufacturing," *Business Horizons,* vol. 60, no. 5, pp. 677-688, 2017/09/01/ 2017.

[25] T. Friedman, M. Michalski, T. R. Goodman, and J. E. Brown, "3D printing from diagnostic images: a radiologist's primer with an emphasis on musculoskeletal imaging—putting the 3D printing of pathology into the hands of every physician," *Skeletal Radiology,* vol. 45, no. 3, pp. 307-321, 2016/03/01 2016.

[26] J. D. Hiller and H. Lipson, "STL 2.0: a proposal for a universal multi-material additive manufacturing file format," in *Proceedings of the Solid Freeform Fabrication Symposium*, 2009, vol. 3, pp. 266-278: Citeseer.

[27] B. Ezair, F. Massarwi, and G. Elber, "Orientation analysis of 3D objects toward minimal support volume in 3D-printing," *Computers & Graphics,* vol. 51, pp. 117-124, 2015/10/01/ 2015.

[28] M. Taufik and P. K. Jain, "Role of build orientation in layered manufacturing: a review," *International Journal of Manufacturing Technology and Management,* vol. 27, no. 1-3, pp. 47-73, 2013/01/01 2013.

[29] E. George, P. Liacouras, F. J. Rybicki, and D. Mitsouras, "Measuring and Establishing the Accuracy and Reproducibility of 3D Printed Medical Models," *RadioGraphics,* vol. 37, no. 5, pp. 1424-1450, 2017/09/01 2017.

[30] C.-Y. Liaw and M. Guvendiren, "Current and emerging applications of 3D printing in medicine," *Biofabrication,* vol. 9, no. 2, p. 024102, 2017/06/07 2017.

[31] V. Filippou and C. Tsoumpas, "Recent advances on the development of phantoms using 3D printing for imaging with CT, MRI, PET, SPECT, and ultrasound," *Medical Physics,* https://doi.org/10.1002/mp.13058 vol. 45, no. 9, pp. e740-e760, 2018/09/01 2018.

[32] H. Zaidi and B. M. W. Tsui, "Review of Computational Anthropomorphic Anatomical and Physiological Models," *Proceedings of the IEEE,* vol. 97, no. 12, pp. 1938-1953, 2009.

[33] L. A. Shepp and B. F. Logan, "The Fourier reconstruction of a head section," *IEEE Transactions on Nuclear Science,* vol. 21, no. 3, pp. 21-43, 1974.

[34] X. G. Xu and K. F. Eckerman, *Handbook of anatomical models for radiation dosimetry*. CRC press, 2009.

[35] B. Alfano *et al.*, "An MRI digital brain phantom for validation of segmentation methods," (in eng), *Medical image analysis,* vol. 15, no. 3, pp. 329-339, 2011/06// 2011.

[36] V. Shapiro, "Chapter 20 - Solid Modeling," in *Handbook of Computer Aided Geometric Design*, G. Farin, J. Hoschek, and M.-S. Kim, Eds. Amsterdam: North-Holland, 2002, pp. 473-518.

[37] M. Bern and P. Plassmann, "Chapter 6 - Mesh Generation," in *Handbook of Computational Geometry*, J. R. Sack and J. Urrutia, Eds. Amsterdam: North-Holland, 2000, pp. 291-332.

[38] R. S. Snell, *Clinical neuroanatomy*. Lippincott Williams & Wilkins, 2010.

[39] J. H. Martin, M. E. Leonard, and H. Radzyner, *Neuroanatomy: text and atlas*. Elsevier New York, 1989.

[40] P. Videbech, "PET measurements of brain glucose metabolism and blood flow in major depressive disorder: a critical review," *Acta Psychiatrica*

Scandinavica, https://doi.org/10.1034/j.1600-0447.2000.101001011.x vol. 101, no. 1, pp. 11-20, 2000/01/01 2000.

[41] R. M. Lewitt and S. Matej, "Overview of methods for image reconstruction from projections in emission computed tomography," *Proceedings of the IEEE,* vol. 91, no. 10, pp. 1588-1611, 2003.

[42] C. A. Pelizzari, G. T. Chen, D. R. Spelbring, R. R. Weichselbaum, and C. T. Chen, "Accurate three-dimensional registration of CT, PET, and/or MR images of the brain," (in eng), *Journal of computer assisted tomography,* vol. 13, no. 1, pp. 20-26, 1989 Jan-Feb 1989.

[43] E. Lin and A. Alessio, "What are the basic concepts of temporal, contrast, and spatial resolution in cardiac CT?," (in eng), *Journal of cardiovascular computed tomography,* vol. 3, no. 6, pp. 403-408, Nov-Dec 2009.

[44] C. Catana, "Development of Dedicated Brain PET Imaging Devices: Recent Advances and Future Perspectives," *Journal of Nuclear Medicine,* vol. 60, no. 8, p. 1044, 2019.

[45] T. F. Budinger, "PET instrumentation: What are the limits?," *Seminars in Nuclear Medicine,* vol. 28, no. 3, pp. 247-267, 1998/07/01/ 1998.

[46] E. C. Frey, J. L. Humm, and M. Ljungberg, "Accuracy and Precision of Radioactivity Quantification in Nuclear Medicine Images," *Seminars in Nuclear Medicine,* vol. 42, no. 3, pp. 208-218, 2012/05/01/ 2012.

[47] E. J. Hoffman, P. D. Cutler, W. M. Digby, and J. C. Mazziotta, "3-D phantom to simulate cerebral blood flow and metabolic images for PET," *IEEE Transactions on Nuclear Science,* vol. 37, no. 2, pp. 616-620, 1990.

[48] E. J. Hoffman, P. D. Cutler, T. M. Guerrero, W. M. Digby, and J. C. Mazziotta, "Assessment of Accuracy of PET Utilizing a 3-D Phantom to Simulate the Activity Distribution of [18F]Fluorodeoxyglucose Uptake in the Human Brain," *Journal of Cerebral Blood Flow & Metabolism,* vol. 11, no. 1_suppl, pp. A17-A25, 1991/03/01 1991.

[49] B. Alfano, A. Prinster, and M. Quantarelli, "Process for realishing a biomorphic, stereolithographed phantom, which is multicompartmental and suitable for multanalytical examinations, and relevant device," ed: Google Patents, 2006.

[50] S. M. Aquilonius *et al.*, "In vivo evaluation of striatal dopamine reuptake sites using 11C-nomifensine and positron emission tomography," *Acta Neurologica Scandinavica,* https://doi.org/10.1111/j.1600-0404.1987.tb03582.x vol. 76, no. 4, pp. 283-287, 1987/10/01 1987.

[51] I. Despotović, B. Goossens, and W. Philips, "MRI Segmentation of the Human Brain: Challenges, Methods, and Applications," *Computational and*

Mathematical Methods in Medicine, vol. 2015, p. 450341, 2015/03/01 2015.

[52] A. Fedorov *et al.*, "3D Slicer as an image computing platform for the Quantitative Imaging Network," *Magnetic Resonance Imaging,* vol. 30, no. 9, pp. 1323-1341, 2012/11/01/ 2012.

[53] W. E. Lorensen and H. E. Cline, "Marching cubes: A high resolution 3D surface construction algorithm," presented at the Proceedings of the 14th annual conference on Computer graphics and interactive techniques, 1987. Available: https://doi.org/10.1145/37401.37422

[54] F. Fischer, "FDM and Polyjet 3D printing," vol. 60, no. 6, 2015.

[55] R. Hashemi Sanatgar, C. Campagne, and V. Nierstrasz, "Investigation of the adhesion properties of direct 3D printing of polymers and nanocomposites on textiles: Effect of FDM printing process parameters," *Applied Surface Science,* vol. 403, pp. 551-563, 2017/05/01/ 2017.

[56] R. Bannon, S. Parihar, Y. Skarparis, O. Varsou, and E. Cezayirli, "3D printing the pterygopalatine fossa: a negative space model of a complex structure," *Surgical and Radiologic Anatomy,* vol. 40, no. 2, pp. 185-191, 2018/02/01 2018.

[57] J. M. Ralph, C. Marc, T. Robert, E. S. Chester, and P. Kevin, "The utility of 3D printing for surgical planning and patient-specific implant design for complex spinal pathologies: case report," (in English), *Journal of Neurosurgery: Spine SPI,* vol. 26, no. 4, pp. 513-518, 01 Apr. 2017 2017.

[58] W. Oropallo and L. A. Piegl, "Ten challenges in 3D printing," *Engineering with Computers,* vol. 32, no. 1, pp. 135-148, 2016/01/01 2016.

[59] N. I. Ciprian *et al.*, "Challenges and limitations of patient-specific vascular phantom fabrication using 3D Polyjet printing," in *Proc.SPIE*, 2014, vol. 9038.

[60] C. Hazelaar *et al.*, "Using 3D printing techniques to create an anthropomorphic thorax phantom for medical imaging purposes," *Medical Physics,* https://doi.org/10.1002/mp.12644 vol. 45, no. 1, pp. 92-100, 2018/01/01 2018.

[61] E. G. Gordeev, A. S. Galushko, and V. P. Ananikov, "Improvement of quality of 3D printed objects by elimination of microscopic structural defects in fused deposition modeling," *PLOS ONE,* vol. 13, no. 6, p. e0198370, 2018.

[62] L. Yang, S. Li, Y. Li, M. Yang, Q. J. J. o. M. E. Yuan, and Performance, "Experimental investigations for optimizing the extrusion parameters on FDM PLA printed parts," vol. 28, no. 1, pp. 169-182, 2019.

[63] T.-C. Yang and C.-H. Yeh, "Morphology and Mechanical Properties of 3D Printed Wood Fiber/Polylactic Acid Composite Parts Using Fused Deposition Modeling (FDM): The Effects of Printing Speed," *Polymers,* vol. 12, no. 6, 2020.

[64] R. Anitha, S. Arunachalam, and P. Radhakrishnan, "Critical parameters influencing the quality of prototypes in fused deposition modelling," *Journal of Materials Processing Technology,* vol. 118, no. 1, pp. 385-388, 2001/12/03/ 2001.

[65] D. Popescu, A. Zapciu, C. Amza, F. Baciu, and R. Marinescu, "FDM process parameters influence over the mechanical properties of polymer specimens: A review," *Polymer Testing,* vol. 69, pp. 157-166, 2018/08/01/ 2018.

[66] M. A. Pirozzi, E. Andreozzi, M. Magliulo, P. Gargiulo, M. Cesarelli, and B. Alfano, "Automated Design of Efficient Supports in FDM 3D Printing of Anatomical Phantoms," in *XV Mediterranean Conference on Medical and Biological Engineering and Computing – MEDICON 2019*, Cham, 2020, pp. 292-300: Springer International Publishing.

[67] J. A. Kasten, T. Vetterli, F. Lazeyras, and D. Van De Ville, "3D-printed shepp-logan phantom as a real-world benchmark for MRI," *Magnetic Resonance in Medicine,* https://doi.org/10.1002/mrm.25593 vol. 75, no. 1, pp. 287-294, 2016/01/01 2016.

[68] A. Altermatt *et al.*, "Design and construction of an innovative brain phantom prototype for MRI," *Magnetic Resonance in Medicine,* https://doi.org/10.1002/mrm.27464 vol. 81, no. 2, pp. 1165-1171, 2019/02/01 2019.

[69] A. Lalehpour and A. Barari, "Post processing for Fused Deposition Modeling Parts with Acetone Vapour Bath," *IFAC-PapersOnLine,* vol. 49, no. 31, pp. 42-48, 2016/01/01/ 2016.

[70] L. M. Galantucci, F. Lavecchia, and G. Percoco, "Experimental study aiming to enhance the surface finish of fused deposition modeled parts," *CIRP Annals,* vol. 58, no. 1, pp. 189-192, 2009/01/01/ 2009.

[71] E. J. McCullough and V. K. Yadavalli, "Surface modification of fused deposition modeling ABS to enable rapid prototyping of biomedical microdevices," *Journal of Materials Processing Technology,* vol. 213, no. 6, pp. 947-954, 2013/06/01/ 2013.

[72] S. González-Villà, A. Oliver, S. Valverde, L. Wang, R. Zwiggelaar, and X. Lladó, "A review on brain structures segmentation in magnetic resonance imaging," *Artificial Intelligence in Medicine,* vol. 73, pp. 45-69, 2016/10/01/ 2016.

[73] R. Z. Shilling, T. Q. Robbie, T. Bailloeul, K. Mewes, R. M. Mersereau, and M. E. Brummer, "A Super-Resolution Framework for 3-D High-Resolution and High-Contrast Imaging Using 2-D Multislice MRI," *IEEE Transactions on Medical Imaging,* vol. 28, no. 5, pp. 633-644, 2009.

[74] E. Visser *et al.*, "Automatic segmentation of the striatum and globus pallidus using MIST: Multimodal Image Segmentation Tool," *NeuroImage,* vol. 125, pp. 479-497, 2016/01/15/ 2016.

[75] E. Visser, M. C. Keuken, B. U. Forstmann, and M. Jenkinson, "Automated segmentation of the substantia nigra, subthalamic nucleus and red nucleus in 7T data at young and old age," (in eng), *NeuroImage,* vol. 139, pp. 324-336, 2016.

[76] D. C. Collier *et al.*, "Assessment of consistency in contouring of normal-tissue anatomic structures," *Journal of Applied Clinical Medical Physics,* https://doi.org/10.1120/jacmp.v4i1.2538 vol. 4, no. 1, pp. 17-24, 2003/12/01 2003.

[77] P. A. Yushkevich *et al.*, "User-guided 3D active contour segmentation of anatomical structures: Significantly improved efficiency and reliability," *NeuroImage,* vol. 31, no. 3, pp. 1116-1128, 2006/07/01/ 2006.

[78] B. Fischl *et al.*, "Whole Brain Segmentation: Automated Labeling of Neuroanatomical Structures in the Human Brain," *Neuron,* vol. 33, no. 3, pp. 341-355, 2002/01/31/ 2002.

[79] S. Mehmet and S. Bülent, "Survey over image thresholding techniques and quantitative performance evaluation," *Journal of Electronic Imaging,* vol. 13, no. 1, pp. 146-165, 1/1 2004.

[80] R. Dehdasht-Heydari and S. Gholami, "Automatic Seeded Region Growing (ASRG) Using Genetic Algorithm for Brain MRI Segmentation," *Wireless Personal Communications,* vol. 109, no. 2, pp. 897-908, 2019/11/01 2019.

[81] N. Passat, C. Ronse, J. Baruthio, J.-P. Armspach, C. Maillot, and C. Jahn, "Region-growing segmentation of brain vessels: An atlas-based automatic approach," *Journal of Magnetic Resonance Imaging,* https://doi.org/10.1002/jmri.20307 vol. 21, no. 6, pp. 715-725, 2005/06/01 2005.

[82] T. Węgliński and A. Fabijańska, "Brain tumor segmentation from MRI data sets using region growing approach," in *Perspective Technologies and Methods in MEMS Design*, 2011, pp. 185-188.

[83] D. G. Stork, R. O. Duda, P. E. Hart, and D. J. A. W.-I. P. Stork, "Pattern classification," 2001.

[84] W. M. Wells, W. E. L. Grimson, R. Kikinis, and F. A. Jolesz, "Adaptive segmentation of MRI data," *IEEE Transactions on Medical Imaging,* vol. 15, no. 4, pp. 429-442, 1996.

[85] C. W. Therrien, *Decision estimation and classification: an introduction to pattern recognition and related topics*. John Wiley & Sons, Inc., 1989.

[86] J. Ashburner and K. J. Friston, "Unified segmentation," *NeuroImage,* vol. 26, no. 3, pp. 839-851, 2005/07/01/ 2005.

[87] K. M. Pohl, J. Fisher, W. E. L. Grimson, R. Kikinis, and W. M. Wells, "A Bayesian model for joint segmentation and registration," *NeuroImage,* vol. 31, no. 1, pp. 228-239, 2006/05/15/ 2006.

[88] Y. Zhang, M. Brady, and S. Smith, "Segmentation of brain MR images through a hidden Markov random field model and the expectation-maximization algorithm," *IEEE Transactions on Medical Imaging,* vol. 20, no. 1, pp. 45-57, 2001.

[89] G. B. Coleman and H. C. Andrews, "Image segmentation by clustering," *Proceedings of the IEEE,* vol. 67, no. 5, pp. 773-785, 1979.

[90] D. L. Pham, C. Xu, and J. L. Prince, "Current Methods in Medical Image Segmentation," *Annual Review of Biomedical Engineering,* vol. 2, no. 1, pp. 315-337, 2000/08/01 2000.

[91] J. Qiao *et al.*, "Data on MRI brain lesion segmentation using K-means and Gaussian Mixture Model-Expectation Maximization," *Data in Brief,* vol. 27, p. 104628, 2019/12/01/ 2019.

[92] D. W. Shattuck, S. R. Sandor-Leahy, K. A. Schaper, D. A. Rottenberg, and R. M. Leahy, "Magnetic Resonance Image Tissue Classification Using a Partial Volume Model," *NeuroImage,* vol. 13, no. 5, pp. 856-876, 2001/05/01/ 2001.

[93] Z. Ji, Y. Xia, Q. Chen, Q. Sun, D. Xia, and D. D. Feng, "Fuzzy c-means clustering with weighted image patch for image segmentation," *Applied Soft Computing,* vol. 12, no. 6, pp. 1659-1667, 2012/06/01/ 2012.

[94] Z.-X. Ji, Q.-S. Sun, and D.-S. Xia, "A modified possibilistic fuzzy c-means clustering algorithm for bias field estimation and segmentation of brain MR image," *Computerized Medical Imaging and Graphics,* vol. 35, no. 5, pp. 383-397, 2011/07/01/ 2011.

[95] L. A. Zadeh, "Fuzzy sets as a basis for a theory of possibility," *Fuzzy Sets and Systems,* vol. 1, no. 1, pp. 3-28, 1978/01/01/ 1978.

[96] W. Cai, S. Chen, and D. Zhang, "Fast and robust fuzzy c-means clustering algorithms incorporating local information for image segmentation," *Pattern Recognition,* vol. 40, no. 3, pp. 825-838, 2007/03/01/ 2007.

[97]   M. N. Ahmed, S. M. Yamany, N. Mohamed, A. A. Farag, and T. Moriarty, "A modified fuzzy c-means algorithm for bias field estimation and segmentation of MRI data," *IEEE Transactions on Medical Imaging,* vol. 21, no. 3, pp. 193-199, 2002.

[98]   B. N. Li, C. K. Chui, S. Chang, and S. H. Ong, "Integrating spatial fuzzy clustering with level set methods for automated medical image segmentation," *Computers in Biology and Medicine,* vol. 41, no. 1, pp. 1-10, 2011/01/01/ 2011.

[99]   J. Ashburner, "Computational anatomy with the SPM software," *Magnetic Resonance Imaging,* vol. 27, no. 8, pp. 1163-1174, 2009/10/01/ 2009.

[100] M. Kass, A. Witkin, and D. Terzopoulos, "Snakes: Active contour models," *International Journal of Computer Vision,* vol. 1, no. 4, pp. 321-331, 1988/01/01 1988.

[101] D. Terzopoulos, A. Witkin, and M. Kass, "Constraints on deformable models:Recovering 3D shape and nonrigid motion," *Artificial Intelligence,* vol. 36, no. 1, pp. 91-123, 1988/08/01/ 1988.

[102] L. D. Cohen and I. Cohen, "Finite-element methods for active contour models and balloons for 2-D and 3-D images," *IEEE Transactions on Pattern Analysis and Machine Intelligence,* vol. 15, no. 11, pp. 1131-1147, 1993.

[103] S. Kichenassamy, A. Kumar, P. Olver, A. Tannenbaum, and A. Yezzi, "Gradient flows and geometric active contour models," in *Proceedings of IEEE International Conference on Computer Vision*, 1995, pp. 810-815.

[104] V. Caselles, R. Kimmel, and G. Sapiro, "Geodesic Active Contours," *International Journal of Computer Vision,* vol. 22, no. 1, pp. 61-79, 1997/02/01 1997.

[105] P. Mesejo, A. Valsecchi, L. Marrakchi-Kacem, S. Cagnoni, and S. Damas, "Biomedical image segmentation using geometric deformable models and metaheuristics," *Computerized Medical Imaging and Graphics,* vol. 43, pp. 167-178, 2015/07/01/ 2015.

[106] A. Huang, R. Abugharbieh, and R. Tam, "A Hybrid Geometric–Statistical Deformable Model for Automated 3-D Segmentation in Brain MRI," *IEEE Transactions on Biomedical Engineering,* vol. 56, no. 7, pp. 1838-1848, 2009.

[107] L. Wang, F. Shi, W. Lin, J. H. Gilmore, and D. Shen, "Automatic segmentation of neonatal images using convex optimization and coupled level sets," *NeuroImage,* vol. 58, no. 3, pp. 805-817, 2011/10/01/ 2011.

[108] J.-H. Xue, A. Pizurica, W. Philips, E. Kerre, R. Van De Walle, and I. Lemahieu, "An integrated method of adaptive enhancement for

unsupervised segmentation of MRI brain images," *Pattern Recognition Letters,* vol. 24, no. 15, pp. 2549-2560, 2003/11/01/ 2003.

[109] Z. Tu, K. L. Narr, P. Dollar, I. Dinov, P. M. Thompson, and A. W. Toga, "Brain Anatomical Structure Segmentation by Hybrid Discriminative/Generative Models," *IEEE Transactions on Medical Imaging,* vol. 27, no. 4, pp. 495-508, 2008.

[110] I. Despotovic, E. Vansteenkiste, and W. Philips, "Brain volume segmentation in newborn infants using multi-modal MRI with a low inter-slice resolution," in *2010 Annual International Conference of the IEEE Engineering in Medicine and Biology*, 2010, pp. 5038-5041.

[111] A. Ortiz, J. M. Gorriz, J. Ramirez, and D. Salas-Gonzalez, "Improving MR brain image segmentation using self-organising maps and entropy-gradient clustering," *Information Sciences,* vol. 262, pp. 117-136, 2014/03/20/ 2014.

[112] "Magnetic Resonance Imaging of the Brain and Spine, 4th ed., Vol. 1 and 2," *American Journal of Neuroradiology,* vol. 30, no. 5, p. e76, 2009.

[113] B. De Coene *et al.*, "MR of the brain using fluid-attenuated inversion recovery (FLAIR) pulse sequences," *American Journal of Neuroradiology,* vol. 13, no. 6, p. 1555, 1992.

[114] C. Granziera and T. Sprenger, "Brain Inflammation, Degeneration, and Plasticity in Multiple Sclerosis," in *Brain Mapping*, A. W. Toga, Ed. Waltham: Academic Press, 2015, pp. 917-927.

[115] A. L. Alexander *et al.*, "Characterization of Cerebral White Matter Properties Using Quantitative Magnetic Resonance Imaging Stains," *Brain Connectivity,* vol. 1, no. 6, pp. 423-446, 2011/12/01 2011.

[116] M. D. Does, "Inferring brain tissue composition and microstructure via MR relaxometry," *NeuroImage,* vol. 182, pp. 136-148, 2018/11/15/ 2018.

[117] B. Alfano, A. Brunetti, M. Arpaia, A. Ciarmiello, E. M. Covelli, and M. Salvatore, "Multiparametric display of spin-echo data from MR studies of brain," *Journal of Magnetic Resonance Imaging,* https://doi.org/10.1002/jmri.1880050218 vol. 5, no. 2, pp. 217-225, 1995/03/01 1995.

[118] J. B. M. Warntjes, M. Engström, A. Tisell, and P. Lundberg, "Brain Characterization Using Normalized Quantitative Magnetic Resonance Imaging," *PLOS ONE,* vol. 8, no. 8, p. e70864, 2013.

[119] B. Alfano *et al.*, "Unsupervised, automated segmentation of the normal brain using a multispectral relaxometric magnetic resonance approach," *Magnetic Resonance in Medicine,* https://doi.org/10.1002/mrm.1910370113 vol. 37, no. 1, pp. 84-93, 1997/01/01 1997.

[120] B. Alfano *et al.*, "Automated segmentation and measurement of global white matter lesion volume in patients with multiple sclerosis," *Journal of Magnetic Resonance Imaging,* https://doi.org/10.1002/1522-2586(200012)12:6<799::AID-JMRI2>3.0.CO;2-# vol. 12, no. 6, pp. 799-807, 2000/12/01 2000.

[121] O. Dietrich, "Conventional Spin-Echo and Gradient-Echo Pulse Sequences," in *Parallel Imaging in Clinical MR Applications*, S. O. Schoenberg, O. Dietrich, and M. F. Reiser, Eds. Berlin, Heidelberg: Springer Berlin Heidelberg, 2007, pp. 113-118.

[122] G. M. Rojas, U. Raff, J. C. Quintana, I. Huete, and M. Hutchinson, "Image fusion in neuroradiology: Three clinical examples including MRI of Parkinson disease," *Computerized Medical Imaging and Graphics,* vol. 31, no. 1, pp. 17-27, 2007/01/01/ 2007.

[123] R. Stokking, I. G. Zubal, and M. A. Viergever, "Display of fused images: Methods, interpretation, and diagnostic improvements," *Seminars in Nuclear Medicine,* vol. 33, no. 3, pp. 219-227, 2003/07/01/ 2003.

[124] A. Hagiwara *et al.*, "SyMRI of the Brain: Rapid Quantification of Relaxation Rates and Proton Density, With Synthetic MRI, Automatic Brain Segmentation, and Myelin Measurement," (in eng), *Investigative radiology,* vol. 52, no. 10, pp. 647-657, 2017/10// 2017.

[125] D. Ma *et al.*, "Magnetic resonance fingerprinting," (in eng), *Nature,* vol. 495, no. 7440, pp. 187-192, 2013.

[126] A. Traboulsee *et al.*, "Revised Recommendations of the Consortium of MS Centers Task Force for a Standardized MRI Protocol and Clinical Guidelines for the Diagnosis and Follow-Up of Multiple Sclerosis," *American Journal of Neuroradiology,* vol. 37, no. 3, p. 394, 2016.

[127] M. Quarantelli *et al.*, "Brain tissue volume changes in relapsing-remitting multiple sclerosis: correlation with lesion load," (in eng), *NeuroImage,* vol. 18, no. 2, pp. 360-366, 2003/02// 2003.

[128] P. Ehses *et al.*, "IR TrueFISP with a golden-ratio-based radial readout: Fast quantification of T1, T2, and proton density," *Magnetic Resonance in Medicine,* https://doi.org/10.1002/mrm.24225 vol. 69, no. 1, pp. 71-81, 2013/01/01 2013.

[129] G. Palma *et al.*, "A Novel Multiparametric Approach to 3D Quantitative MRI of the Brain," *PLOS ONE,* vol. 10, no. 8, p. e0134963, 2015.

[130] W. Chau and A. R. McIntosh, "The Talairach coordinate of a point in the MNI space: how to interpret it," *NeuroImage,* vol. 25, no. 2, pp. 408-416, 2005/04/01/ 2005.

[131] J. D. Schmahmann *et al.*, "Three-Dimensional MRI Atlas of the Human Cerebellum in Proportional Stereotaxic Space," *NeuroImage,* vol. 10, no. 3, pp. 233-260, 1999/09/01/ 1999.

[132] J. Ashburner and G. Ridgway, "Symmetric Diffeomorphic Modeling of Longitudinal Structural MRI," *Frontiers in Neuroscience,* 10.3389/fnins.2012.00197 vol. 6, p. 197, 2013.

[133] C. Blaiotta, P. Freund, M. J. Cardoso, and J. Ashburner, "Generative diffeomorphic modelling of large MRI data sets for probabilistic template construction," *NeuroImage,* vol. 166, pp. 117-134, 2018/02/01/ 2018.

[134] P. Kalavathi and V. B. S. Prasath, "Methods on Skull Stripping of MRI Head Scan Images-a Review," (in eng), *Journal of digital imaging,* vol. 29, no. 3, pp. 365-379, 2016.

[135] S. M. Smith, "Fast robust automated brain extraction," *Human Brain Mapping,* https://doi.org/10.1002/hbm.10062 vol. 17, no. 3, pp. 143-155, 2002/11/01 2002.

[136] N. V. Chawla, "Data Mining for Imbalanced Datasets: An Overview," in *Data Mining and Knowledge Discovery Handbook*, O. Maimon and L. Rokach, Eds. Boston, MA: Springer US, 2005, pp. 853-867.

[137] P. Branco, L. Torgo, and R. P. Ribeiro, "A Survey of Predictive Modeling on Imbalanced Domains," vol. 49, no. 2 %J ACM Comput. Surv., p. Article 31, 2016.

[138] B. Krawczyk, "Learning from imbalanced data: open challenges and future directions," *Progress in Artificial Intelligence,* vol. 5, no. 4, pp. 221-232, 2016/11/01 2016.

[139] N. R. Draper and H. Smith, *Applied regression analysis*. John Wiley & Sons, 1998.

[140] J. O. Rawlings, S. G. Pantula, and D. A. Dickey, *Applied regression analysis: a research tool*. Springer Science & Business Media, 2001.

[141] J. D'Errico. (2020, January 13). *polyfitn (https://www.mathworks.com/matlabcentral/fileexchange/34765-polyfitn), MATLAB Central File Exchange. Retrieved January 13, 2020.*

[142] H. Amiri, I. Brouwer, J. P. A. Kuijer, J. C. de Munck, F. Barkhof, and H. Vrenken, "Novel imaging phantom for accurate and robust measurement of brain atrophy rates using clinical MRI," *NeuroImage: Clinical,* vol. 21, p. 101667, 2019/01/01/ 2019.

[143] S. J.-S. Chen *et al.*, "An anthropomorphic polyvinyl alcohol brain phantom based on Colin27 for use in multimodal imaging," *Medical Physics,*

https://doi.org/10.1118/1.3673069 vol. 39, no. 1, pp. 554-561, 2012/01/01 2012.